FERROELECTRIC OXIDES WITH HIGH PIEZOELECTRICITY AND LOW BAND GAP FOR SOLAR ENERGY HARVESTING APPLICATIONS

CHAN MAN KIT

MPhil

The Hong Kong Polytechnic University

2020

The Hong Kong Polytechnic University

Department of Applied Physics

Ferroelectric Oxides with High Piezoelectricity and Low Band Gap for Solar Energy Harvesting Applications

Chan Man Kit

A thesis submitted in partial fulfillment of the requirements for the degree of Master of Philosophy

August 2019

CERTIFICATE OF ORIGINALITY

I hereby declare that this thesis is my own work and that, to the best of my knowledge and belief, it reproduces no material previously published or written, nor material that has been accepted for the award of any other degree or diploma, except where due acknowledgement has been made in the text.

_____(Sign)

Chan Man Kit (Name of student)

Abstract

Ferroelectric materials have attracted considerable interest for photovoltaic applications due to its spontaneous electric polarization that can promote the separation of photo-excited charge carriers and lead to an above-band gap voltage. However, due to the wide optical band gap (2.7-4 eV), the ferroelectric oxides absorb only 8-20 percent of the solar spectrum and exhibit a poor solar energy conversion efficiency which limits their use in photovoltaic applications. In general, the common ferroelectric oxides with a perovskite structure ABO_3 exhibit a wide optical band gap due to the large difference of electronegativity between the oxygen ions and the B-site transition-metal ions. However, the B-site ion also plays a crucial role in the ferroelectric properties of perovskite materials. Any attempt of replacing the B-site ion with the aim of reducing the optical band gap may result in the degradation of the ferroelectric and dielectric properties. In this study, we aim at developing perovskite ferroelectric oxides with large polarization and low optical band gap for solar energy harvesting applications.

Barium titanate-based ferroelectric ceramic $Ba_{0.9}Ca_{0.1}Ti_{0.9}Sn_{0.1}O_3$ (abbreviated as BCTSn-0.1-0.1) has been chosen as the base material due to its large piezoelectric coefficient d_{33} (520 pC/N). After replacing Sn^{4+} with Fe^{3+}, the optical band gap of the ceramic, i.e., $Ba_{0.9}Ca_{0.1}Ti_{1-x}Fe_xO_{3-\delta}$ or BCTFe-0.1-x, decreases with increasing the doping level of Fe^{3+}. The BCTFe-0.1-0.025 ceramic which exhibits the optimized properties for photovoltaic responses, i.e., a low optical band gap (2.78 eV) and good piezoelectric properties (190 pC/N), has been chosen to demonstrate the ferroelectric photovoltaic effect.

The ferroelectric photovoltaic effect of BCTSn-0.1-0.1 and BCTFe-0.1-0.025 has been investigated using interdigitated electrode (IDE) pattern and vertical ITO electrode configuration. For the samples with IDE pattern, the photocurrent of BCTFe-0.1-0.025 is lightly larger than that of BCTSn-0.1-0.1 (0.22 nA vs 0.07 nA). On the other hand, the steady photocurrent of the BCTFe-0.1-0.025 ceramic with vertical electrode configuration is 5.5 nA or 11 nA/cm^2, which is 3 times larger than that of the BCTSn-0.1-0.1 ceramic (1.5 nA or 3 nA/cm^2).

With the aim of studying the effect of the reduction in optical band gap, the photovoltaic response of the non-ferroelectric BCTFe-0.1-0.1 ceramic deposited with asymmetric electrodes of ITO-Cr/Au has been investigated. It is expected that the resulting asymmetric Schottky barriers formed at the top and bottom interfaces will induce the photovoltaic response. The short-circuit current and open-circuit voltage of the BCTFe-0.1-0.1 ceramic measured under 1 sun illumination are 10.9 nA/cm^2 and 0.16 V, respectively. Because of the reduced optical band gap (i.e., 2.24 eV), the photovoltaic response is observed under the illumination of green lights (e.g. 580 nm). Therefore, the enhancement of the photovoltaic current observed in the BCTFe-0.1-0.025 ceramic should be partly attributed to its lower optical band gap. It demonstrates that it is possible to improve the ferroelectric photovoltaic response by reducing the optical band gap and retaining the piezoelectricity at the same time.

On the other hand, the photovoltaic response has also been observed in the BCTFe-0.1-0.1 ceramic deposited with symmetric ITO electrode configuration. This should be attributed to the accumulation of oxygen vacancies in one side of the samples. The distribution of oxygen vacancies can be modulated by an external field and thus the

photocurrent is switchable. The switchable photocurrent is observed on both ferroelectric and non-ferroelectric ceramics.

Acknowledgements

I would like to express my sincere appreciation to my chief supervisor, Prof. K. W. Kwok for his patience, advice, support and constant encouragement throughout my whole study. With his broad knowledge, academic insight, enthusiastic and painstaking guidance, I can finish my MPhil study quickly, smoothly and successfully.

I also need to thank Prof. J. Y. Dai for the photovoltaic measurement, thank Dr. W. Xiao and Dr. J. W. Chen for the D.C. conductivity and pyroelectric measurements. Moreover, I gratefully acknowledge the technical support provided by the Materials Research Centre and Clean Room of the Hong Kong Polytechnic University. Without their help, I cannot finish my experimental work readily.

I would also like to thank all members in Prof. Kwok's group, especially Dr. Ming Zheng, Dr. Yu Sun, Dr. Hailing Sun, Mr H.F. Ting and Miss Y. L. Chan for their friendship, help and valuable discussions on my experiments. In addition, I would like to give my sincere thanks to my colleagues in our department, Mr. Chi Man Wong, Mr. Man Chung Wong and Dr. Vincent Chan, for their great help and assistance.

Last but not the least, I am deeply indebted to my parents and friends for their understanding, constant support and encouragement.

Table of Contents

List of Figures

List of Tables

Chapter 1 Introduction

Since the discovery of ferroelectricity in Rochelle salt in 1921 and then extension to the realm of polycrystalline ceramics (Barium titanate, $BaTiO_3$) during 1940s, various types of ferroelectric materials have been developed and used in industrial and commercial applications, e.g. high-dielectric-constant capacitors, ultrasonic transducers and ferroelectric memories [1]. In recent years, researchers have been interested in ferroelectric materials for applications in piezoelectric energy generation, ferroelectric photovoltaic devices and pyroelectric harvesting [2]. Due to the unique switchable spontaneous polarization, ferroelectric materials play an irreplaceable role in energy-related applications [3]. For example, ferroelectric material exhibits switchable photo-current and photo-voltages larger than its band gap, and thus may be developed as a new type of photovoltaic devices for replacing conventional p-n junction devices [4].

This chapter will start from an introduction of ferroelectric, piezoelectric and pyroelectric materials. Next, the photovoltaic effect in semiconductor p-n junctions and ferroelectric materials will be introduced and compared for better understanding the ferroelectric photovoltaic effect in this study. After that, the latest researches on optical band gap modulation in ferroelectric materials will be reviewed. Finally, the motivation of this study and a brief introduction of each chapter will be given.

1.1. Ferroelectric materials

When discussing the ferroelectricity, it is always linked with pyroelectricity and piezoelectricity because of the specific interrelationship between them in terms of crystal structure. According to crystallography, the crystals can be divided into 32 point groups, 21 of them are non-centrosymmetric which is the necessary condition for the

piezoelectricity. Indeed, only 20 groups have the piezoelectric properties. Among the 20 piezoelectric crystals, 10 of them show spontaneous polarization [1]. Within a specific temperature range, the spontaneous polarization can be varied due to a temperature change. This phenomenon is called the pyroelectric effect. In addition, if the spontaneous polarization can be reversed by an external electric field, the material is defined as ferroelectric. Therefore, if a material is ferroelectric, it must exhibit piezoelectric and pyroelectric responses [2]. Figure 1-1 summarizes the relationship between the piezoelectric, pyroelectric and ferroelectric materials, as well as the general dielectrics.

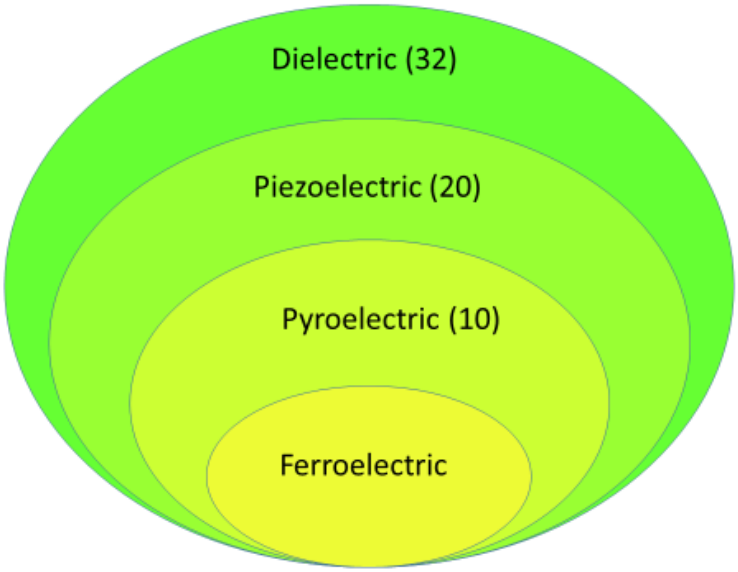

Figure 1-1 Relationship between dielectric, piezoelectric, pyroelectric and ferroelectric materials.

As mentioned above, ferroelectric materials are characterized by two conditions, which are the existence of a spontaneous polarization and its reversibility under an external electric field [2]. Generally, insulating materials can be polarized by an external electric field and the induced polarization (P) is linear with the magnitude of applied electric filed, which is named as dielectric polarization. At high temperatures, i.e., above

the Curie Temperature Tc, a ferroelectric material is at the paraelectric state and presents a nonlinear relationship with the external electric field. A paraelectric-to-ferroelectric phase transition occurs when the temperature decreases and passes through Tc [5]. Although it may undergo several ferroelectric phase transitions at lower temperatures, only the transition temperature at which ferroelectric properties are first observed is called the Curie point [6]. At the ferroelectric phase, there is a spontaneous polarization present in the materials. The spontaneous polarization can be reoriented by an external electric filed and the direction of the polarization is dependent on the electrical history. Therefore, a ferroelectric material always exhibits a polarization-electric field hysteresis loop (PE loop) [7]. Figure 1-2 shows the relationship of dielectric permittivity and dielectric polarization at both the paraelectric and ferroelectric phases of materials. The peak observed in Figure 1-2(a) is known as the Curie Temperature Tc., The material is ferroelectric below the Curie temperature and becomes non-ferroelectric at temperatures above Tc. As illustrated in Figure 1-2(b), when the material is ferroelectric, the polarization increases with increasing the electric field and then becomes saturated. The observed polarization is resulted from the alignment of the spontaneous polarization along the external electric field. When the electric field is removed, the polarization decreases due to the re-orientation, and the remained polarization (i.e., the y-intercept of the PE loop) is defined as the remnant polarization P_r. If the electric field is continually decreased to negative, the magnitude of the field for achieving a zero spontaneous polarization (i.e., the x-intercept) is called the coercive field E_c.

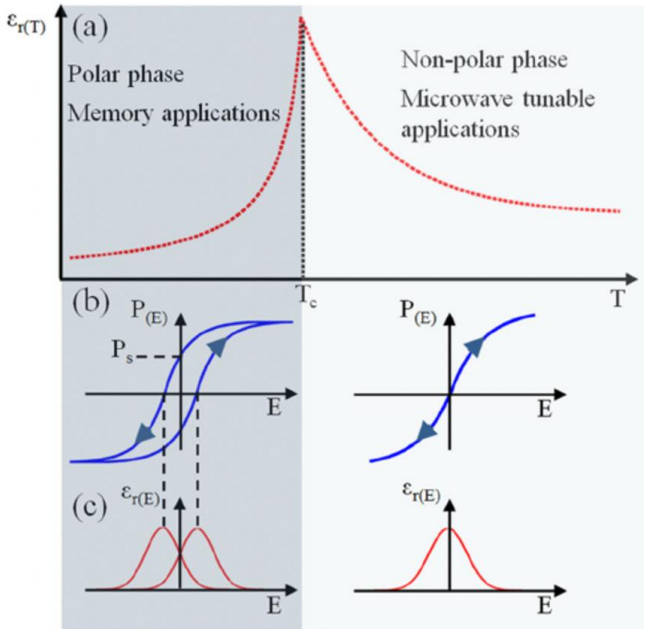

Figure 1-2 (a) Temperature dependence of the dielectric constant of a ferroelectric material. (b) and (c) The corresponding polarization and dielectric constant as a function of applied field below and above Tc [5].

Ferroelectric materials can be divided into four groups according to their crystals structure: tungsten-bronze group [8], pyrochlore group [9], bismuth layer-structure group [10] and perovskite group. In general, the perovskite group is the most common one which has been widely studied. The perovskite structure can be expressed as a chemical formula ABO_3, where the valence of A cations can be varied between +1 and +3 and that of B cation is between +3 and +6 [11]. Barium titanate $BaTiO_3$ will be used as an example in the following discussion. As shown in Figure 1-3, $BaTiO_3$ is a perovskite crystal in which Ba^{2+} occupies the A-site and Ti^{4+} occupies the B-site. Figure 1-3 also shows the different structures of $BaTiO_3$, i.e., the cubic structure in paraelectric phase (> 130°C) and the tetragonal structure in ferroelectric phase (< 130°C) In the paraelectric phase, the structure is highly symmetric as compared with those in the ferroelectric phase. In the ferroelectric phase, the reversibility of the spontaneous polarization is contributed by the

displacement of the cation Ti^{4+} located at the centre of the unit cell. The displacement can be considered as a shift of O^{2-} and Ti^{4+} ion with respect to Ba^{2+} [12]. For an as-prepared ferroelectric (polycrystalline) ceramic, the spontaneous polarization in each grain is randomly oriented and thus the net polarization of the ceramic is zero. To trigger the piezoelectric response, the as-prepared ferroelectric ceramics must be polarized by using a sufficiently high electric field, e.g. 1-3 kV/mm for $BaTiO_3$ [6]. The details of the poling process will be discussed in the following section.

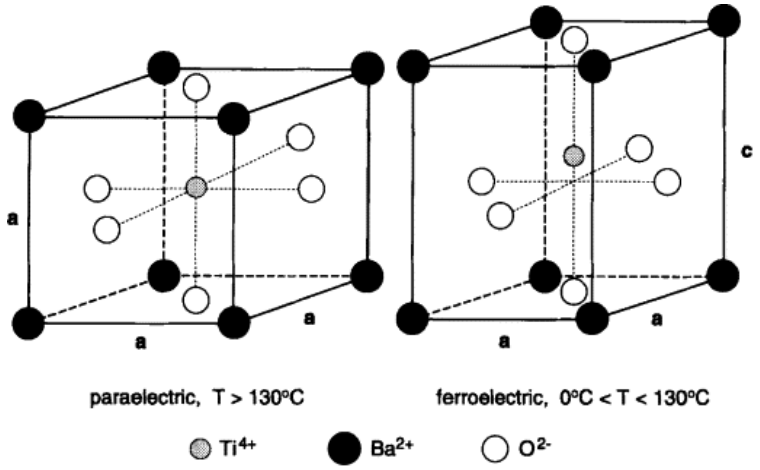

Figure 1-3 The perovskite BaTiO3 which is cubic in the paraelectric phase and tetragonal in the ferroelectric phase [12].

1.1.1. Piezoelectric effect

For observing the piezoelectric response of ferroelectric ceramics, the spontaneous polarization in each grain should be aligned along the same direction to avoid the cancellation effect. The process of the alignment of the spontaneous polarizations using a high external electric field is called poling. After poling, the ferroelectric ceramics exhibit the piezoelectric effect. Piezoelectric effects have two aspects: (1) direct effect and (2) converse effect [13]. The direct piezoelectric effect refers to the generation of electrical charges on sample surfaces by applying an external mechanical stress. The

generated charges are resulted from the change of the aligned polarization, i.e., the shifting of the positive and negative charges in the unit cells due to the external stress. For the converse piezoelectric effect, a strain is induced by the application of an external electric field.

Figure 1-4 illustrates the inter-relationships between the strain and charges for the direct and converse piezoelectric effects. The piezoelectric coupling factor (e.g. k_p and k_{33}), piezoelectric charge coefficients (e.g. d_{33} and d_{31}) and piezoelectric voltage coefficients (e.g. g_{33}) are generally used for characterizing the properties of piezoelectric materials.

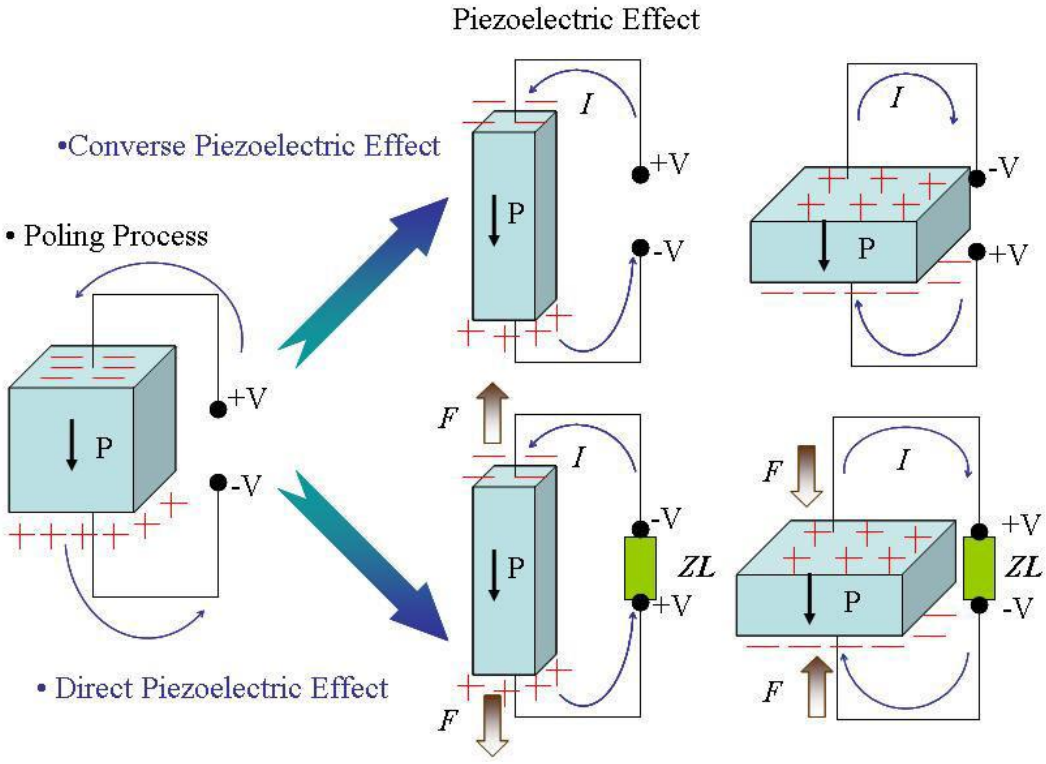

Figure 1-4 The difference between direct piezoelectric effect and converse piezoelectric effect [13].

1.1.2. Pyroelectric effect

Similar to the piezoelectric effect, the pyroelectric properties of ferroelectric materials only appear after poling. The pyroelectric effect is a phenomenon that the variation of the (aligned) spontaneous polarization is induced by a change in temperature [7]. In poled ferroelectric materials, due to the aligned spontaneous polarization, the polarization charges are localized beneath the surfaces. Free charges of opposite polarity and the same quantity are bounded by the localized charges on the surfaces, and thus there is no net charge (observed) in the ferroelectric materials. However, as the temperature increases (decreases), the polarization and then the localized charges decrease (increases), and thus leading to net charges appeared on the surfaces. If the surfaces are connected to an ammeter, the net charges will form an electric current called pyroelectric current. The direction of the pyroelectric current is dependent on the polarization direction as well as the temperature change, i.e., heating or cooling. A schematic diagram of the pyroelectric effect for poled ferroelectric materials undergoing a heating process is shown in Figure 1-5.

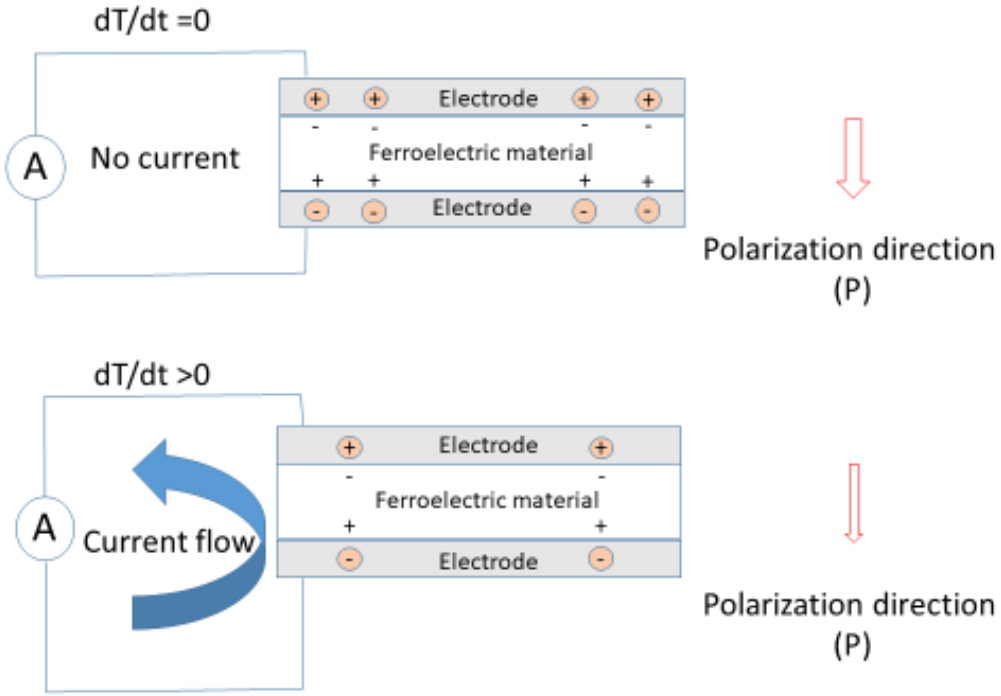

Figure 1-5 Pyroelectric effect for poled ferroelectric materials undergoing an increasing temperature process.

The pyroelectric properties can be characterized by a pyroelectric coefficient p, given as:

$$p = \frac{\Delta P}{\Delta T} \qquad (1.1)$$

where ΔP is the change in polarization and ΔT is the (small) change in temperature. The pyroelectric coefficient has a unit of C m^{-2} K^{-1} [14].

1.1.3. Lead-free perovskite piezoelectric materials

After the discovery of piezoelectricity in $BaTiO_3$(BTO) ceramics around 1940s, ($Pb(Zr_{1-x}Ti_x)O_3$ or PZT) ceramics were soon discovered and then widely used for various dielectric and piezoelectric applications [3]. As compared with BTO ceramics, PZT ceramics have better properties, i.e., larger piezoelectric coefficients, higher Curie

temperature and larger electromechanical coupling factors [1, 15]. However, due to more and more lead-based piezoelectric ceramics were used, the problem of environmental pollution has attracted a great deal of attention. In order to reduce the impact of hazardous materials to the environment, European Union restricted the use of heavy metals such as lead and mercury in electric and electronic devices since 2003[16]. For these reasons, there has been urgent demand of the development of lead-free piezoelectric ceramics for substituting lead-based materials.

Overall, there are three families of lead-free perovskite structure ceramics: (1) $K_{0.5}Na_{0.5}NbO_3$ (KNN) [17, 18], (2) $Na_{0.5}Bi_{0.5}TiO_3$ (BNT) [19, 20], and (3) $BaTiO_3$ (BTO) [21, 22]. Indeed, each system has its unique advantages and weakness.

The KNN system exhibits a high Curie temperature (Tc ~ 420°C), good ferroelectric properties (P_r ~ 33 μC/cm^2), and large electromechanical coupling factors. However, owing to the high volatility of alkali metal, KNN-based ceramics with dense structure are difficult to obtain [23].

The BNT system is another promising candidate for lead-free piezoelectric ceramics due to its large remnant polarization (P_r ~ 33 μC/cm^2) and high Curie temperature (Tc ~ 320°C). But, its large leakage and high coercive field (Ec ~ 7 kV/mm) make the poling hard to be proceed [6].

The BT system is the first discovered piezoelectric polycrystal, which has also attracted a great deal of attention because of the high piezoelectric coefficient (d_{33} ~ 190 pC/N). Yet, its low Curie temperature (Tc ~ 120°C) limits its working temperature for practical applications [24].

1.1.4. Barium titanate-based ceramic (BT-based system)

Serval lead-free piezoelectric systems have been briefly mentioned above, as for highlighting the research topic of this work, only BT-based systems with excellent piezoelectric properties are discussed in detail. In 2009, Ren et al. accomplished a pioneering development work of lead-free piezoelectric ceramics, in which a surprisingly large d_{33} of 620 pC/N was first achieved by constructing a "morphotropic phase boundary (MPB)" from a tri-critical triple point of $Ba(Ti_{0.8}Zr_{0.2})O_3$-$x(Ba_{0.7}Ca_{0.3})TiO_3$ (BZT-xBCT) system [24]. Figure 1-6 shows the phase diagram of BZT-xBCT ceramics. The large piezoelectric coefficient is contributed by the co-existence of the cubic, rhombohedral and tetragonal phases. Such an excellent piezoelectric performance is comparable to the commonly used engineering piezoceramics e.g. PZT-5A and PZT-5H [25].

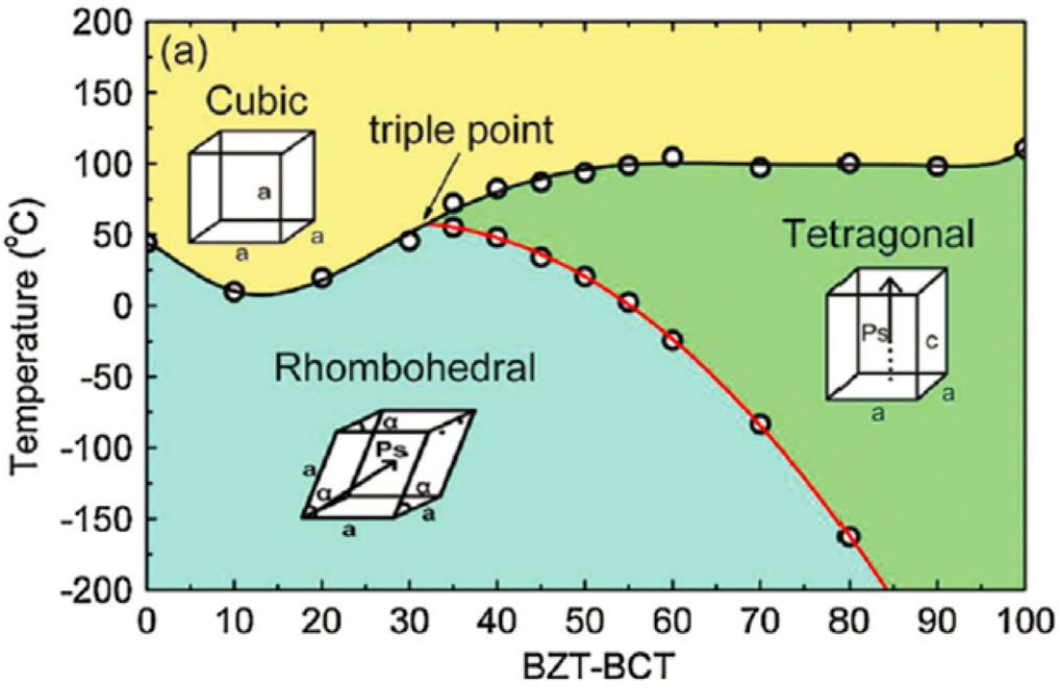

Figure 1-6 Phase diagram of $Ba(Zr_{0.2}Ti_{0.8})O_3$-$x(Ba_{0.3}Ca_{0.7})TiO_3$ ceramics [24]

Unlike the BNT-based or KNN-based systems, the BT system contains no volatile elements, and thus a predesigned stoichiometric ratio can be well maintained even after

the high-temperature fabrication processes [16]. Indeed, there is other BT-based system $(Ba,Ca)(Ti,Sn)O_3$ which also exhibits excellent piezoelectric performance comparable to the BZT-xBCT system. Similar to BZT-xBCT, the good piezoelectric properties of the $(Ba,Ca)(Ti,Sn)O_3$ system are achieved by optimizing the substitution contents of Sn [26]. As shown in Figure 1-7(a), a maximum d_{33} of 521 pC/N is achieved in the composition of $Ba_{0.9}Ca_{0.1}Ti_{0.9}Sn_{0.1}O_3$. The large piezoelectric coefficient is attributed to the increase in possible polarization states, which is the result of the coexistence of the orthorhombic and tetragonal phases at room temperature [27]. Indeed, the substitution of Sn^{4+} induces a change of the phase transition temperature. Figure 1-8 shows the temperature dependence of the dielectric properties for the $Ba_{0.9}Ca_{0.1}Ti_{(1-x)}Sn_xO_3$ ceramics. It can be seen that the Curie Temperature Tc of the ceramic decreases linearly from 138°C to below room temperature with increasing the Sn content. When the content of Sn reaches 0.10 mol, the orthorhombic and tetragonal phases coexist in the ceramic at room temperature. In addition, the dielectric properties can be modulated by the B-site cation doping. The optimal composition is $Ba_{0.9}Ca_{0.1}Ti_{0.88}Sn_{0.12}O_3$. These results suggest that $(Ba,Ca)(Ti,Sn)O_3$ is a promising candidate for exhibiting excellence piezoelectric and ferroelectric properties. In the following section, the photovoltaic effect in p-n junction will be introduced and then the relationship between the ferroelectric properties and photovoltaic effect will be discussed.

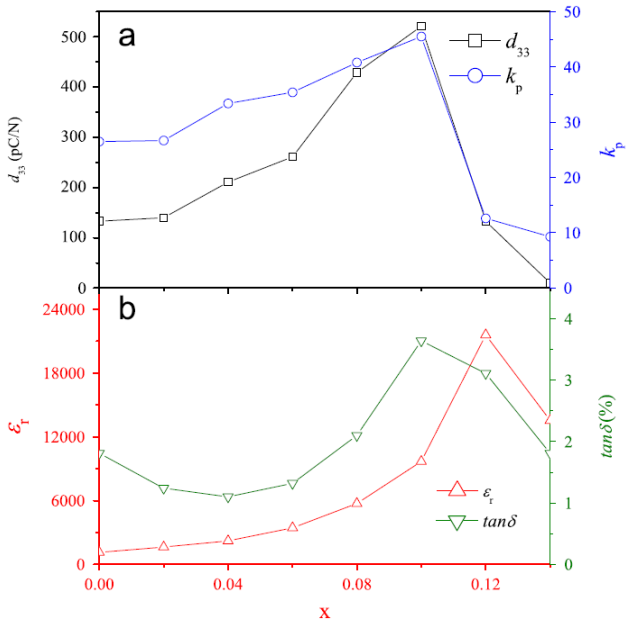

Figure 1-7 Sn content dependences of (a)piezoelectric and (b)dielectric properties of the $Ba_{0.9}Ca_{0.1}Ti_{0.9}Sn_xO_3$ ceramics [27].

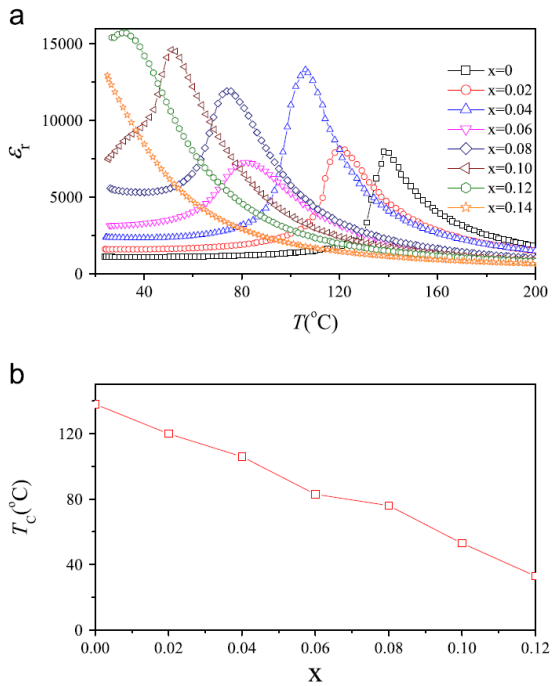

Figure 1-8 (a)Temperature dependences of dielectric permittivity at 10kHz for the $Ba_{0.9}Ca_{0.1}Ti_{0.9}Sn_xO_3$ ceramics; (b) variation of Tc with x for $Ba_{0.9}Ca_{0.1}Ti_{0.9}Sn_xO_3$ ceramics [27].

1.2. Photovoltaic effect

The photovoltaic (PV) effect refers to a phenomenon that voltage and electric current are generated in a material when it is illuminated by a light with energy higher that the optical band gap of the material. The PV effect involves the conversion of light to electricity, which has been considered as one of the promising green energy sources [28].

The development of photovoltaic effect is mainly dominated by semiconducting materials in the past decades [29]. The structure of semiconductor-based devices is generally known as a p-n junction. When the light with above-band gap energy illuminates the semiconductor devices, the excited electrons will be driven by a built-in electric field formed at the p-n junction. Because of the nature of the p-n junction, the built-in electric field is limited by the band gap of the semiconductors, and thus the voltage output of the p-n junction devices will not be larger than the band gap. As the power conversion efficiency (PCE) of semiconductor-based photovoltaic devices is dependent on the product of the short-circuit current density, open-circuit voltage and the fill factor, the maximum efficiency of p-n junction devices is limited by the band gap of materials. This limitation is known as Shockley–Quisser limit [30].

On the other hand, the photovoltaic effect in ferroelectric materials which was first observed in the early 1950s does not need a p-n junction [31]. The photo-excited carriers in ferroelectric materials are separated by the spontaneous polarization, and thus the voltage output can be larger than the band gap [4]. Theoretically, the efficiency of ferroelectric photovoltaic effect may be larger than that of p-n junction devices.

In the following, the mechanism of photovoltaic effect in conventional p-n junction devices will first be introduced in detail. The possible mechanism of ferroelectric

photovoltaic effect will be proposed and then recent researches on ferroelectric photovoltaic effect will be reviewed.

1.2.1. Photovoltaic effect in semiconductor

Before discussing the photovoltaic effect in semiconductor p-n junctions, it needs to introduce the concept of semiconductors first and then p-n junctions.

1.2.1.1. Band gap model of semiconductor

Figure 1-9 shows the band diagram of metal, semiconductor and insulator. In conductors, the valence band and the conduction band overlap and thus the electrons always move freely within the conductor, resulting in good thermal and electrical conductivity. In semiconductors and insulators, there is an electron forbidden area between the conduction band and valence bands which is known as the band gap [32]. In general, semiconductors have a smaller band gap than the insulators. Typically, the band gap of semiconductors is lesser than 3 eV, which is equivalent to the cutoff energy of the visible spectrum [33]. In insulators, owing to the larger band gap, more energy is needed for exciting electrons from the valence band to the conduction band. Thus, the electrical conductivity of insulators is always low and that of semiconductors lies between those of conductors and insulators.

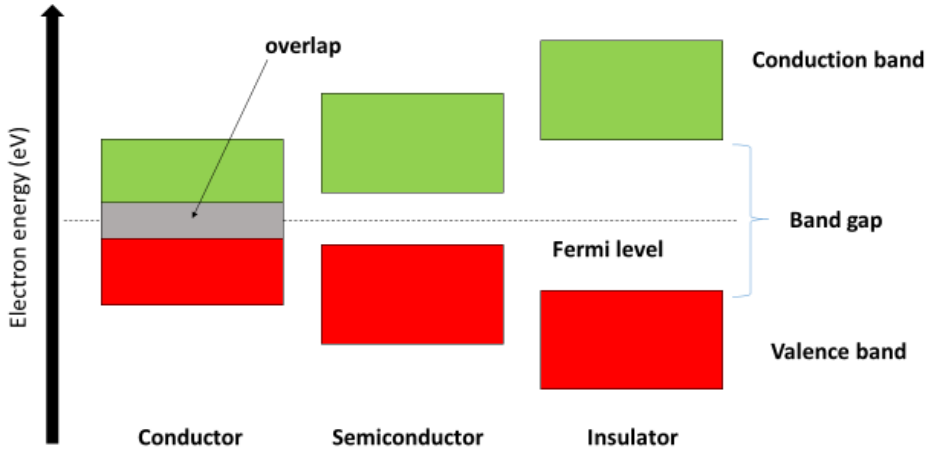

Figure 1-9 A band diagram of conductors, semiconductors, and insulators.

1.2.1.2.p-n junction

For practical applications, semiconductors should be doped with impurities of different valences. The doping with donors (e.g. phosphorus) will make the semiconductor to be an n-type semiconductor, while the semiconductor doped with acceptors (e.g. boron) is called a p-type semiconductor. From the band gap point of view, n-type and p-type semiconductors shows additional energy levels within the band gap. In n-type materials, the electron energy level is near the top of the band gap, and thus the electron can be easily excited to the conduction band. In p-type materials, the hole energy level is near the valence band and thus the holes can be easily excited to the valence band to form mobile holes in the valence band [34].

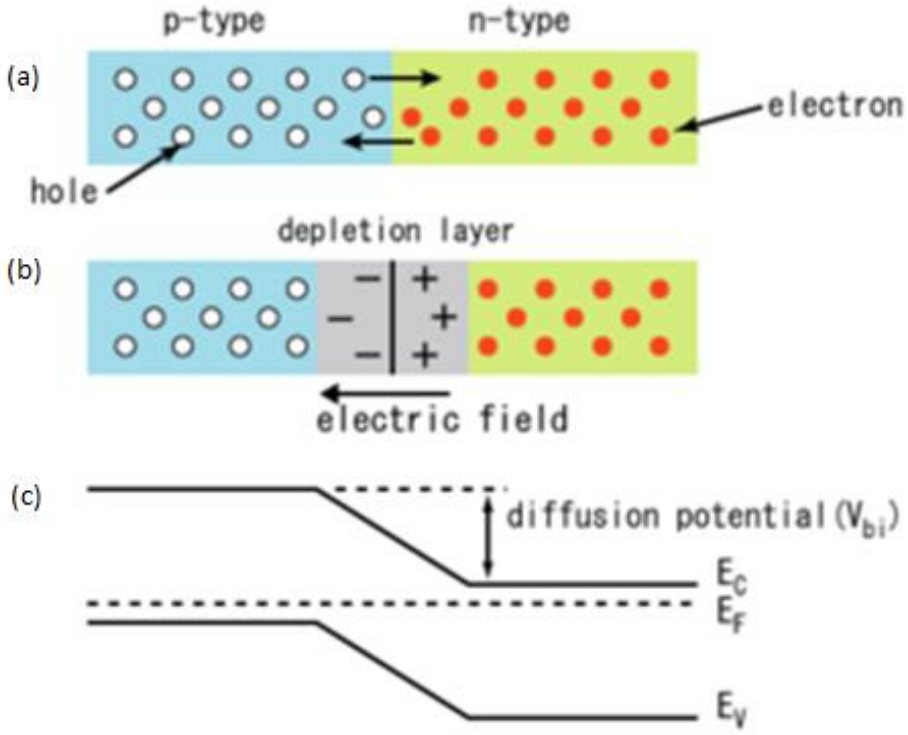

Figure 1-10 the schematic diagram of (a) p-n junction contact;(b) depletion layer in equilibrium;(c) diffusion potential with deletion region[35].

When a p-type and n-type semiconductor are joined together, as shown at Figure 1-10(a), the electrons from the n-type and holes from p-type will diffuse across the junction and combine with each other to form a depletion region. The equilibrium state of the p-n junction is shown in Figure 1-10(b). Due to thermal equilibrium, the Fermi level is uniform throughout the junction and a band bending is resulted. As illustrated in Figure 1-10(c), a build-in field within the junction is formed and its magnitude is dependent on the energy level difference between the p-type and n-type semiconductors. [33]

1.2.1.3.Conventional photovoltaic effect

Now, it is time to see how the photovoltaic effect works in the p-n junction. When a light with enough energy (i.e., above the optical band gap) of the semiconductor) shines on the p-n junction devices, electrons are excited from the valence band to the conduction band and holes are left in the valence band. The generated electrons and holes only remain in a short period of time before recombination [32]. However, owing to the build-in field, the excited electrons are attracted towards the positively charged region, i.e., the n-type side and the holes are attracted to the p-type side. The current which flows across the junction due to the efficient charge separation is defined as the photovoltaic current. The efficiency (η) of the p-n junction-based photovoltaic devices can be express by the following equation [33]:

$$\eta = \frac{J_{sc}V_{oc}FF}{P_{in}} \tag{1.2}$$

where V_{oc} is the open-circuit voltage, J_{sc} is the short-circuit current, P_{in} is the power of the photons incident on the photovoltaic devices and FF is the fill factor.

1.2.2. Photovoltaic effect in ferroelectric

As mentioned above, the photovoltage of semiconductor devices is limited by the built-in field of the depletion region. However, this limitation will not happen in ferroelectric photovoltaic devices. The ferroelectric photovoltaic devices can exhibit the above-band gap open-circuit voltage which is distinguished from the p-n junction devices [36]. The other characteristics of ferroelectric photovoltaic devices is the switchable photocurrent which is resulted from the re-orientation of the spontaneous polarization under an external electric field [37]. These unique ferroelectric photovoltaic features provide another pathway for the light-to-electric energy applications.

There are several models proposed for explaining the ferroelectric photovoltaic effect, including the depolarization field model [38, 39], domain wall model [36], Schottky-junction effect [40, 41] and shift current model [42]. At present, the shift current model is well explained the ferroelectric photovoltaic effect rather than other mechanisms [42]. To avoid any confusion, only the modified bulk photovoltaic effect based on the shift current model will be discussed in detail for well understanding the origin of the ultra-high photovoltage. Besides, the experimental evidences including recent studies for the ferroelectric photovoltaic effect will be reviewed.

1.2.2.1. Bulk photovoltaic effect

The bulk photovoltaic effect is most frequently used for explaining the abnormally large photovoltage of ferroelectric photovoltaic effect. According to the shift current model, a steady current is formed under illumination due to the non-centrosymmetric nature of the ferroelectric materials [42]. It proposes that the excited electrons jump from a k momentum state to a k' momentum state and the possibility for the reverse process is not equal. Thus, a net flow of photo-generated charge carriers occurs. The short-circuit current J_{sc} is generated by an above-band gap illumination. The short-circuit current can be described by the Glass model [43, 44]:

$$J_{sc} = k(\omega)\alpha(\omega)I_o \tag{1.3}$$

where ω represents the frequency, α is the absorption coefficient of the material, I_o is the intensity of the radiation and k is the glass coefficient with unit cm/V which first proposed by Glass et al. It is in fact a third-rank photovoltaic tensor [127].

The first proposed Glass model is unable to explain the angular dependence of the photovoltaic current in Fe-doped $LiNbO_3$ under illumination of light with rotating polarization [45]. With the help of the shift current model which involves the wave vector

k, the angular dependence of photovoltaic current can be well described. Additionally, the total current density J_{total} emerging in the ferroelectric materials can be described as:

$$J_{total} = J_{pv} + (\sigma_{dark} + \sigma_{ph})E \quad (1.4)$$

where J_{pv} is the photovoltaic current, σ_{dark} and σ_{ph} are the dark conductivity and photoconductivity, respectively, and E is the internal electric field which depends on the applied voltage (V) and the electrode distance (d). The ferroelectric photovoltaic devices can act as a current source due to the very low conductivity of most ferroelectric materials. For the open circuit case, V_{oc} can be expressed as:

$$V_{oc} = Ed = \frac{J_{pv}}{\sigma_{dark}+\sigma_{ph}} d \quad (1.5)$$

Form this equation, it is immediately found that V_{oc} can be increased by suppressing both σ_{dark} and σ_{ph}. It may figure out that the ferroelectric photovoltaic device, which exhibits a high photovoltage, always shows poor conductivity. On the contrary, ferroelectric photovoltaic devices with better conductivity are crucial to obtain the large photovoltaic current. However, if the ferroelectric photovoltaic devices exhibit good conductivity (i.e., a high leakage current), its ferroelectric properties may degenerate. Typically, the photocurrent density obtained from ferroelectric materials is in the order of $nAcm^{-2}$.

1.2.2.2. Characteristics of ferroelectric photovoltaic effect

The photocurrent in ferroelectric materials was first observed in single crystals of $BaTiO_3$ in 1956. Without an electric field, the crystal exhibits a pyroelectric current as well as a steady photovoltaic current just above Curie temperature [31]. Afterwards, the effects of light on other ferroelectric materials have also been reported, including $LiNbO_3$ [46, 47, 48], $KNbO_3$ [49], and $Pb(ZrTi)O_3$ [50, 51, 52].

A typical ferroelectric photovoltaic current observed in $LiNbO_3$ is shown in Figure 1-11. The current flow direction is opposite to the spontaneous polarization orientation. The observed current can be separated into two part: the peaks (pyroelectric current) at the moment of On/Off and the flow (photovoltaic current) in the steady state. As discussed in Section 1.1, a ferroelectric material must be pyroelectric. When the light is turned on, the temperature of materials increases and then a pyroelectric current is induced. Later on, when the temperature becomes equilibrium, the pyroelectric current disappears because of the lack of the temperature change. The observed current is then mainly the photovoltaic current.

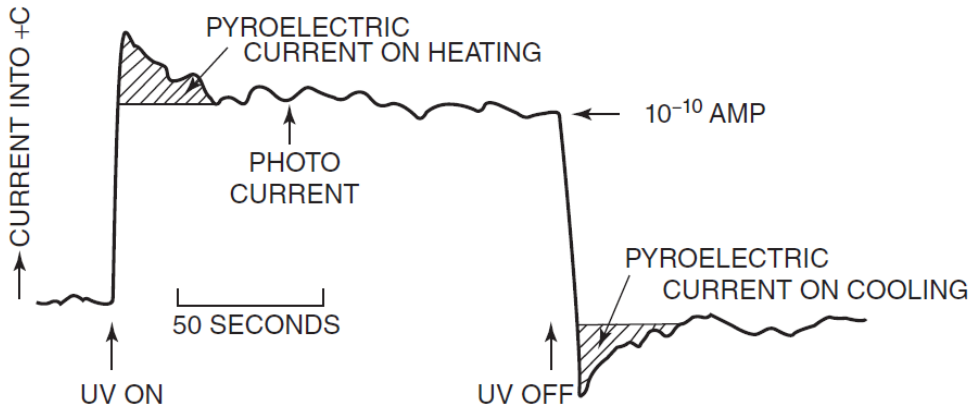

Figure 1-11 Current-versus-time along the c crystallographic direction of the $LiNbO_3$ crystal when the a face of the crystal was illuminated with a UV light from the mercury discharge lamp. [53]

Besides, it is also worth to mention the J-V characteristic of the ferroelectric photovoltaic devices. As shown in Figure 1-12, the current density shows the ohmic characteristic, i.e., the current increases linear with the voltage. From the power conversion point of view, the fill factor FF, which is defined as the ratio of the maximum

power obtained from the current-voltage curve to the product of the short-circuit current and the open-circuit voltage, is quite low e.g., 10%-30% due to the linear characteristic of the current-voltage curve. However, the FF reaches up to 80% in the classical semiconductors [54].

On the other hand, Figure 1-12 shows the inversion characteristic of the J-V curve by the re-orientation of spontaneous polarization. It can be found that the above-band gap voltage is nearly symmetric in both poling directions suggesting that the ferroelectric polarization plays a dominant role in the photovoltaic effect [55]. Both the above-band gap voltage and reversible current have not been observed in conventional p-n junction devices.

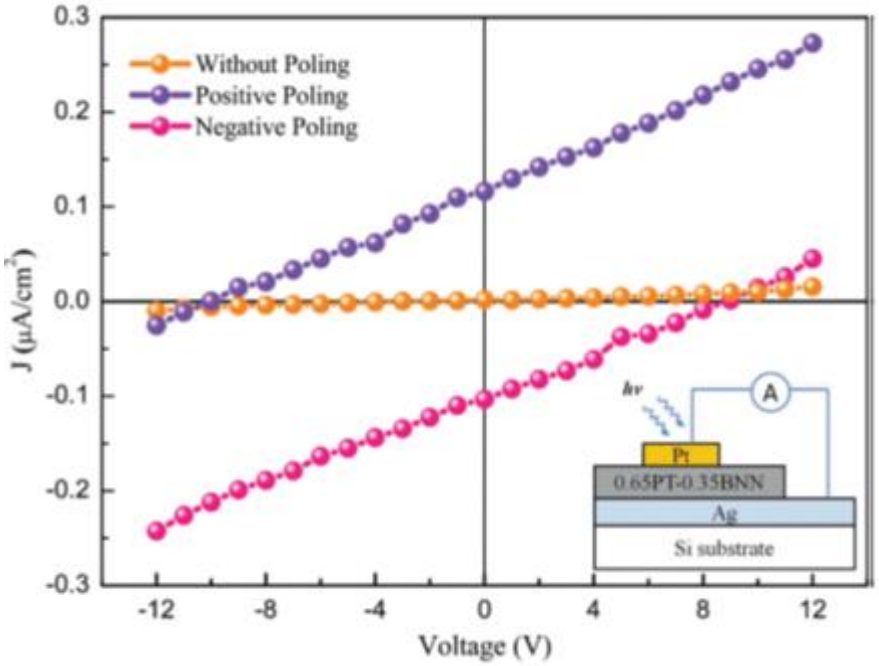

Figure 1-12 J-V characteristics of 50-μm-thick 0.65PT–0.35BNN (x = 0) sample measured with white light of 200 mW cm $^{-2}$ [55].

1.2.2.3. Recent studies

Over half a century, the photovoltaic effect in ferroelectrics has remained scientific curiosity rather than practical applications because of its poor energy conversion

efficiency e.g. <0.1% [54]. Recently, Nechache et al. have reported that the optical band gap of double perovskite oxides Bi_2FeCrO_6(BFCO) could be tuned by modulating the B-site cation ordering. Due to a wider absorption spectrum, the power conversion efficiency of the devices reached 8-1% [56]. It showed a possible pathway to bring the ferroelectric photovoltaic effect from laboratory to the real life. Later on, with the purpose of modulating the ferroelectric photovoltaic effect, several approaches have been proposed, including the electrode design, polarization modulation and optical band gap reduction [57, 58].

For the electrode selection aspect, Cao et al. demonstrated that via the insertion of a n-type cuprous oxide (Cu_2O) layer between the $Pb(Zr,Ti)O_3$ film and Pt electrode in a ITO/PZT/Pt cell, the short-circuit photocurrent could be increased 120-fold to 4.8 mA/cm^2 and the power conversion efficiency was increased 72-fold to 0.57% under 100 mW/cm^2 illumination [59]. The role of Cu_2O was to modify the energy level at the junction of PZT/Pt for achieving an efficient charge collection in the cathode. Nevertheless, Zhang's group used a La-doped PZT pellet in a size of 10 x 10 x 0.3 mm^3 to examine the ferroelectric photovoltaic effect of metal electrodes which includes Mg, Ag and Pt. It was found that the photovoltaic effect could be enhanced by using low work function metals as the electrodes e.g. Mg. Under a 1 sun (100 mW/cm^2) illumination, the Mg/PLZT/ITO structure exhibited the best ferroelectric photovoltaic performance, i.e., the short-circuit current and open-circuit voltage were 150 and 2 times larger than those of Pt/PLZT/ITO, respectively [60].

On the other hand, according to the shift current model, the separation of the electron-holes pairs is driven by the non-centrosymmetric nature of ferroelectric materials [61]. Hence, increasing the non-centrosymmetric of a crystal by varying the chemical

composition should be another pathway for improving the ferroelectric photocurrent. For example, by replacing Bi with La, the crystal symmetry of $BiFeO_3$ is changed from rhombohedral to orthorhombic and resulting in a strong rotation instability of the polarization. Such instability affects the charge transfer at the band edges and thus enhance the photovoltaic current [62].

Finally, the optical band gap engineering is also a hot topic for ferroelectric photovoltaic effect development. As the main objective of this study, the background of optical band gap modulation will be reviewed in detail in the following section.

1.3. Optical band gap modulation

Ferroelectric oxides are stable in a wide range of mechanical, chemical and thermal conditions and can be fabricated using low-cost methods such as solid-state reaction. However, due to the wide optical band gap (2.7-4 eV), the ferroelectric oxides absorb only 8-20 percent of solar spectrum and exhibit a poor solar energy conversion efficiency which limits their application in photovoltaic applications [63]. The optical band gap of well-known ferroelectric oxides exhibiting photovoltaic effect is summarized in Table 1-1.

Table 1-1 The summary of optical band gap of perovskite ferroelectric oxides

Materials	Optical band gap(eV)
$BaTiO_3$ [47, 64 , 65]	3.3
PLZT(3/52/48) [66]	3.4
$BiFeO_3$ [67,68]	2.7
$LiNbO_3$ [69]	3.78
$KNbO_3$ [70, 71]	3.3

The wide optical band gap of ABO_3 ferroelectric oxides is due to the fundamental characteristics of metal-oxygen A-O and B-O bonds. The excitation across optical band gap refers to a charge transfer from oxygen 2p states at the top of the valance band to d states of the transition-metal ion B at the bottom of the conduction band [72]. Due to the large electronegativity difference between oxygen and transition metal ions, the optical band gap of ferroelectric oxides is large [58]. It is suggested that a partial B-site substitution of typical ferroelectrics such as $BaTiO_3$(BTO), $BiFeO_3$(BFO) and $KNbO_3$(KNO) with transition metal ions with high electronegativity, which led to a smaller electronegativity difference, could be an effective tool for reducing the optical band gap of ferroelectric oxides [70 ,73, 74].

The lowest optical band gap for a typical ferroelectric oxide is known to be 2.7eV, which is the value for $BiFeO_3$[67, 68]. Recently, it has been shown that a large optical band gap tunability (Eg=1.1-3.8eV) could be achieved by varying the B-site doping of Ni^{2+} in (1-x) ($KNbO_3$)-x$Ba(Ni_{1/2}Nb_{1/2})O_{3-\delta}$) [70]. In the system, Nb^{5+} is used to maintain the ferroelectricity of oxides and accommodate the oxygen vacancy. K^+ is replaced by Ba^{2+} for the charge compensation of oxygen vacancies. The Ni^{2+} in the B-site plays a crucial role for the optical band gap reduction. It has been shown, based on the first-principles density functional theory (DFT) calculation, the bottom of the conduction band comprised Nb 4d states, while the maximum of the valence band is hybridized the Ni 3d and O 2p state rather than only the O 2p state. Therefore, Ni^{2+} is considered as the key element for the optical band gap reduction in the $KNbO_3$ system. Although the ferroelectric properties became weaker after the doping and impurity was observed, the work showed a possibility of tuning the optical band gap by doping transition metals into ferroelectric materials.

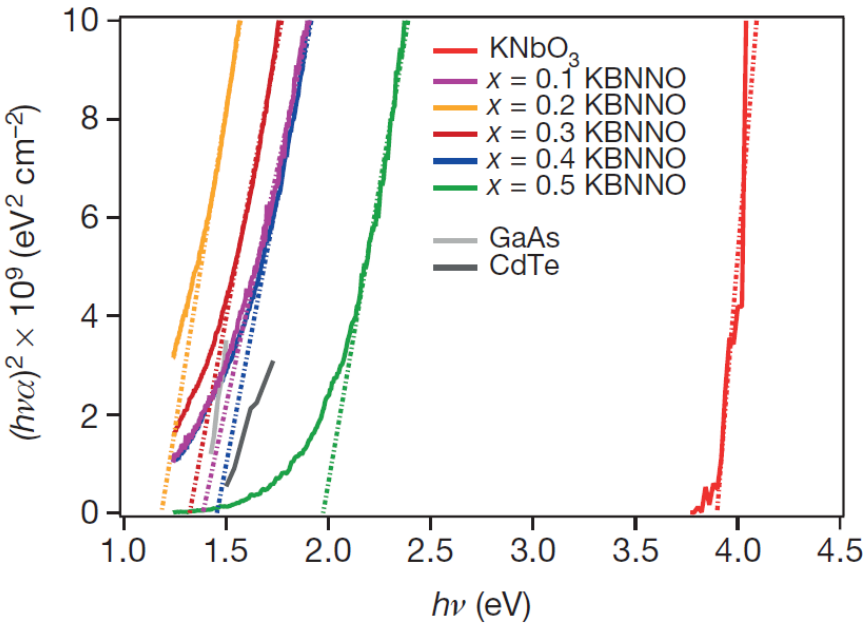

Figure 1-13 KBNNO oxides showing bandgaps from 1.18 eV to 3.8 eV [70].

Very recently, Das's group had showed that the optical band gap of the typical ferroelectric oxide $BaTiO_3$ (BTO) could be tuned from 3.2eV to 1.8eV by doping transition metals [73]. Two transition-metals were used for substituting the B-cation Ti^{4+}. Transition metal Mn^{3+} was used for reducing the optical band gap and Nb^{5+} was used for balancing the net charge of Mn^{3+} dopant and maintaining the ferroelectricity. The reduction of optical band gap was originated from the states of Mn 3d which predominated the top of the valence band and the bottom of the conduction band and thus lowered the optical band gap of oxides. The optimal composition $BaTi_{1-x}(TM_{1/2}Nb_{1/2})_xO_3$ (x=0.075) has been showed having good ferroelectricity (Ps =15.4 μC/cm^2) and a low optical band gap (1.66eV) at room temperature. Although the authors have not demonstrated the enhanced ferroelectric photovoltaic performance of these materials, it provided experimental evidence of optical band gap modulation via chemical doping.

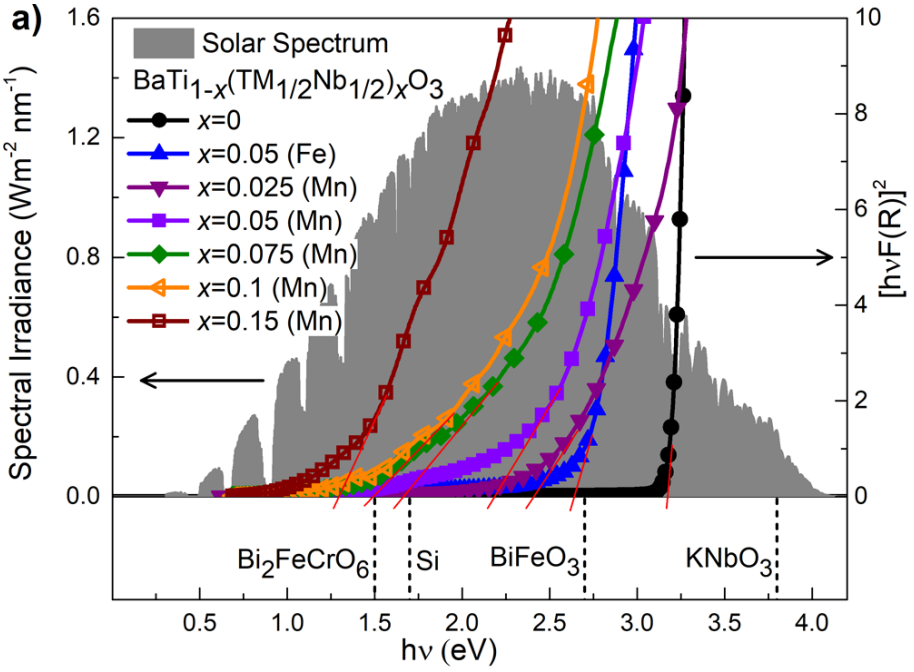

Figure 1-14 BTMNO and BTFNO oxides showing bandgaps from 1.8 eV to 3.1 eV[73].

1.4. Motivation of research

In general, the common ferroelectric oxides with the perovskite structure ABO_3 exhibit a wide optical band gap due to the large difference of electronegativity between the oxygen ions and the B-site transition-metal ions. However, the B-site ion also plays a crucial role for the ferroelectric properties of perovskite materials [75]. Any attempt of replacing the B-site ion with the aim of reducing the optical band gap may result in the degradation of the ferroelectric and dielectric properties [73, 76]. Although there are few substituted systems exhibiting a low optical band gap by chemical doping, they always fail to show either the sizable polarization or enhanced ferroelectric photovoltaic performance.

In this study, it aims to develop perovskite ferroelectric oxides with large polarization and low optical band gap in a result of high piezoelectricity and enhanced photovoltaic performance for solar energy harvesting applications.

Barium titanate-based ferroelectrics ceramics $Ba_{0.9}Ca_{0.1}Ti_{0.9}Sn_{0.1}O_3$ (abbreviated as BCTSn-0.1-0.1) have been chosen as the base material due to its large piezoelectric coefficient d_{33} (520pC/N) [27]. The work focuses on reducing the optical band gap of BCTSn-0.1-0.1 through substituting Sn^{4+} with transition-metal ion Fe^{3+} with high electronegativity (1.9) [77]. Since Fe^{3+} has similar radius of Sn^{4+}, the tolerance factor may not change significantly [78, 79]. As a result, new perovskite-structured ferroelectric oxides can be formed and then the piezoelectric and ferroelectric properties of ceramics can be retained.

Additionally, defects such as oxygen vacancies may be formed after the doping of trivalent ion Fe^{3+}. It has been reported that oxygen vacancies of ferroelectric ceramics may create extra energy levels between the optical band gap [80]. As a result, the optical

band gap will also be reduced with the help of oxygen vacancies. Therefore, the effect of oxygen vacancies on the optical properties of Fe^{3+}-doped $Ba_{0.9}Ca_{0.1}TiO_3$ (BCT) ceramic will be taken into account for understanding the optical band gap mechanism.

In addition, the substitution of different transition-metal ions may also affect the crystallite structure as well as the ferroelectric properties of the oxides. Therefore, the effect of the B-site dopant on the crystal structure, dielectric, piezoelectric and ferroelectric properties will be studies in detail as well. Their inter-relationships with the optical band gap will be revealed for optimizing the chemical composition. As a result, the optimal composition of ferroelectric oxides with low optical band gap and high piezoelectricity can be developed. The newly developed ceramic may also exhibit better ferroelectric photovoltaic performance comparing with the $Ba_{0.9}Ca_{0.1}Ti_{0.9}Sn_{0.1}O_3$ ceramic.

On the other hand, several researches have reported that the migration of oxygen vacancies is as essential as the polarization switching in producing the switchable photovoltaic effect [81, 82, 83]. It has been reported that the flow direction of the photocurrent is independent of the polarization orientation but opposite to the voltage direction in the last treatment [84]. However, most of the works have discussed the effects of oxygen vacancies in ferroelectric materials. It is then hard to distinguish the contributions of the spontaneous polarization and oxygen vacancies in the switchable photovoltaic response. For evaluating the role of oxygen vacancies in the photovoltaic effect, non-ferroelectric ceramics will be developed, e.g., by heavily doped Fe^{3+} into BCT. It is expected that, without the influence of spontaneous polarization, the contribution of oxygen vacancies to the photovoltaic effect can be studied in detail in non-ferroelectric ceramics.

1.5. Scope of work

The main objectives of this work are to demonstrate the ferroelectric photovoltaic effect and study the relationship between the optical band gap and photovoltaic performance of BTO-based perovskite oxides. The thesis consists six chapters:

Chapter 1 briefly introduces the background of ferroelectricity and corresponding materials. It also reviews the photovoltaic mechanisms in semiconductors and ferroelectric materials. Together with the possible pathways for enhancing ferroelectric photovoltaic response, the motivation and objectives of the present work are given.

Chapter 2 provides experimental details on sample preparation and equipment setup. It includes the characterization instruments and techniques for the dielectric, piezoelectric, ferroelectric properties as well as the optical properties.

Chapter 3 presents the dielectric, piezoelectric and ferroelectric properties of Fe/Sn-doped BCT ferroelectric ceramics. The studies of the relationship between the optical band gap and Fe doping level of BCT perovskite oxides are also presented.

Chapter 4 demonstrates the ferroelectric photovoltaic effect on Fe/Sn-doped BCT ferroelectric oxides. Two types of electrode configuration (i.e., in-plane and vertical) will be used together to examine the wavelength-dependent current of samples. In addition, different poling fields will be applied to the samples and then demonstrates the switchable photocurrent of ceramic.

Chapter 5 examines the photovoltaic performances of non-ferroelectric Fe-doped BCT perovskite oxides. The studies of the oxygen vacancies effect on the photovoltaic response of Fe-doped BCT ceramics are also presented.

Chapter 6 gives the conclusion.

Chapter 2 Sample Fabrication and Characterization

2.1. Preparation of the samples

2.1.1. Fabrication procedure of the ceramics

The $Ba_{0.9}Ca_{0.1}Ti_{0.9}Sn_{0.1}O_3$ and $Ba_{0.9}Ca_{0.1}Ti_{1-x}Fe_xO_{3-\delta}$ ceramics were synthesized by a conventional solid state reaction method using high purity metal oxide or carbonate powders: $BaCO_3$ (99.5%), $CaCO_3$ (99%), TiO_2 (99.9%), SnO_2 (99.9%) and Fe_2O_3 (99.5%). A flow chart of the fabrication process is shown in Figure 2-1. The raw materials in the stoichiometric ratio were mixed using ethanol as medium and ball-milled for 10 hours using zirconia ball, and then dried at 120 ˚C and calcined at 1000 ˚C for 4 hours. The calcined powers were ball-milled again for 10 h, dried and mixed with a polyvinyl alcohol (PVA) binder solution (5wt%). The mixture was sieved through an 80-mesh screen and then pressed into disk samples of diameter 12 mm and thickness 0.5 mm by a hydraulic press. After burning out the binder at 650˚C, the samples were finally sintered at 1430 ˚C-1490 ˚C for 2 hours. The sintering temperature was varied depending on the composition.

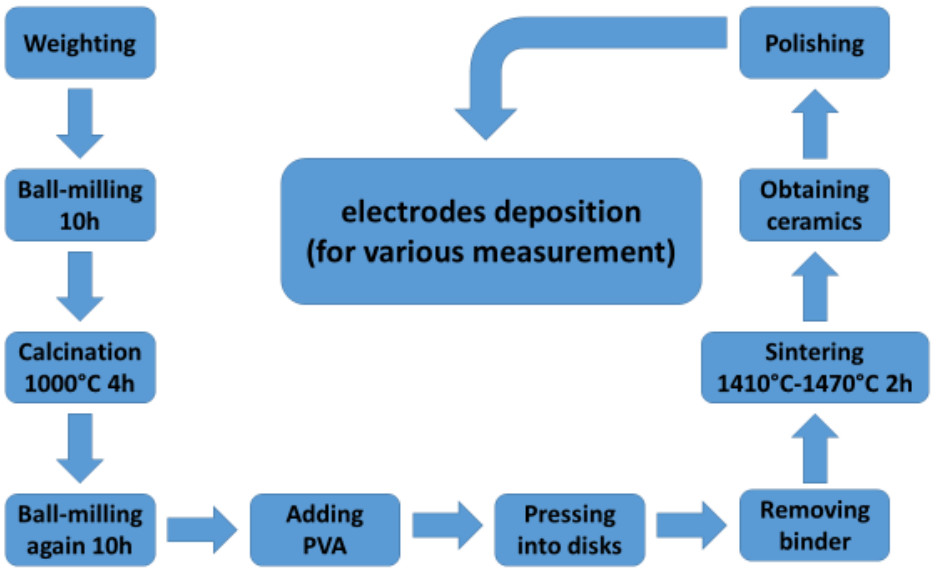

Figure 2-1 Flow chart of sample fabrication.

2.1.2. Preparation of In-plane electrode

An interdigitated electrode (IDE) was deposited on the polished sample surface using the left-off photolithography technique and dc-magnetron sputtering. First, a layer of positive photoresist (AZ5214E) was deposited on the sample surface by spin-coating. After baking at 100 ˚C for 2 min, the sample with photoresist layer was exposed to UV light under a mask with the designed pattern. The exposed photoresist was removed using a developer (AZ300MIF), leaving the desired pattern on the sample surface. A layer of Cr/Au was deposited on the sample surface by dc magnetron sputtering. After removing the remaining photoresist using acetone, a Cr/Au IDE pattern was obtained. The workflow of the electrode fabrication is shown in Figure 2-2.

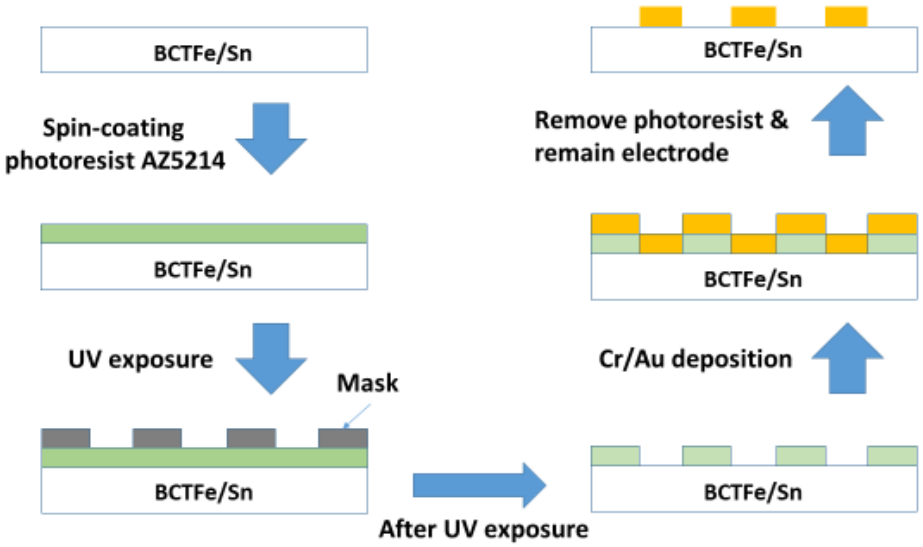

Figure 2-2 The working flow of the fabrication of Cr/Au IDE patterns.

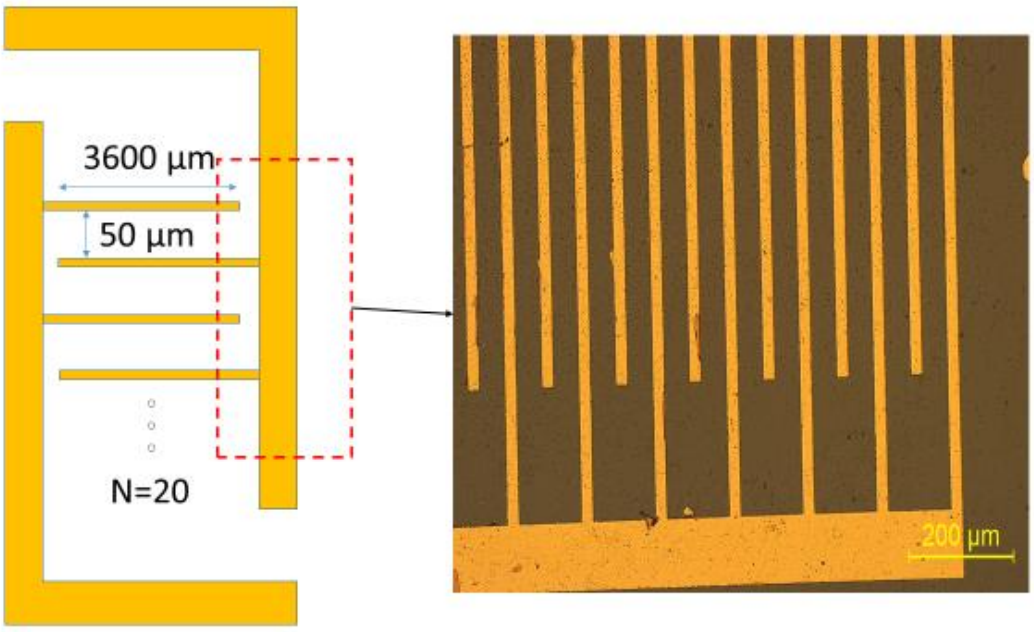

Figure 2-3 Microscopic photograph of the Cr/Au IDE pattern deposited on the surface of a BCTSn-0.1-0.1 bulk sample

The obtained Cr/Au IDE pattern is shown in Figure 2-3. The overlapped electrode length is 3600 μm and the electrode gap is 50 μm. The total number of the gap is 20 and then the effective area of the sample is calculated as the width of the electrode gap multiple by the overlapped electrode length. The resulted effective area is 3.6×10^{-6} m^2. When an electric field is applied, the width of the electrode gap is considered as the thickness of samples.

The IDE pattern allows a direct irradiation of light on the surface of ferroelectric materials to achieve direct interaction without any weakening of the light intensity by the top electrode. Also, under the direct illumination, the generated electron-hole pairs can be uniformly distributed between the two electrodes, resulting in an efficient charge carrier transportation. On the other hand, due to the symmetric electrode configuration, the photovoltaic effect arising from asymmetric Schottky barriers can be ruled out [57].

2.1.3. Preparation of vertical electrode (ITO/Au)

In order to conduct the photovoltaic measurement with larger active area under illumination, an indium tin oxide (ITO) transparent electrode, was deposited on the surface of the ceramic samples. The thick ceramic samples were first adhered on a glass plate as a substrate and then polished to a thickness of 0.1 mm using sandpapers and diamond films. The polished ceramic sample was deposited with an ITO electrode using RF magnetron sputtering as a bottom electrode. The sample has adhered at the surface of the glass which already deposited Au using silver paste. Then, the top surface was deposited with another ITO electrode with a shadow mask. The diameter of the top electrode is 8 mm. The deposition parameters for preparing Cr/Au and ITO electrodes are summarized in Table 2-1. Figure 2-4 shows the transmittance of the ITO electrode

deposited on a quartz glass plate which does not absorb the visible light. The electrodes were then connected with wires for the photovoltaic measurement.

Table 2-1 the summary of deposition parameter for Cr/Au and ITO electrode

	Cr/Au electrode	**ITO electrode**
Type of sputtering	DC magnetron sputtering	RF magnetron sputtering
Deposition temperature	25 ˚C	200˚C
Power	70W	70W
Gas mixture	Pure Ar	O_2:Ar(1:60)
Pressure	$6x10^{-3}$ Torr	$5x10^{-3}$ Torr
Deposition time	Cr(36s)+Au(4min)	40min
Annealing	N/A	1 hour at 200˚C

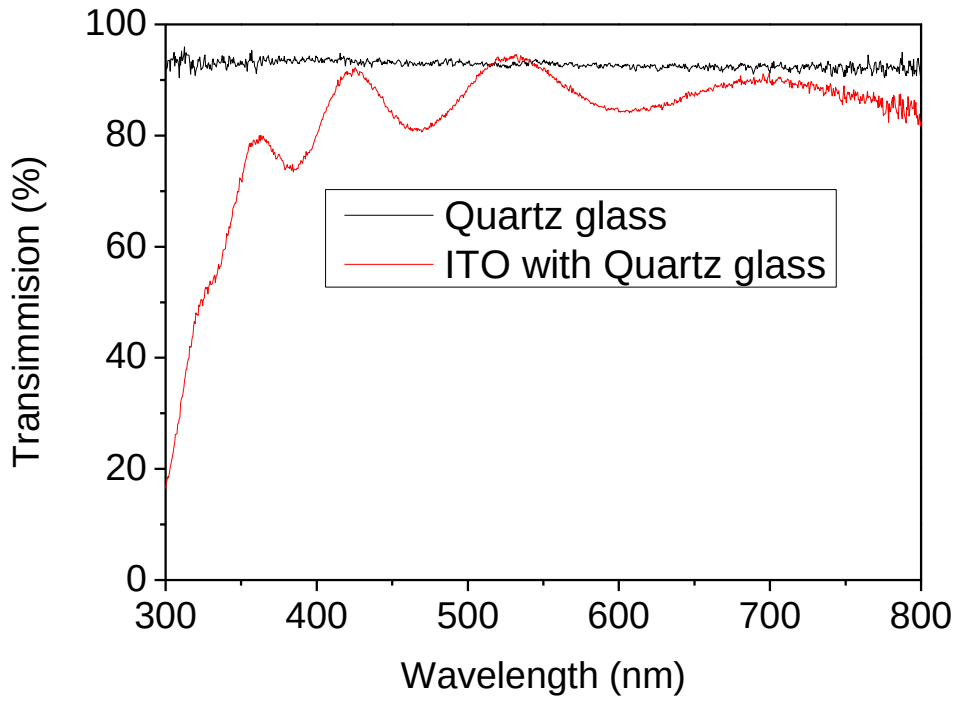

Figure 2-4 The transmittance of ITO electrode

2.2. Characterization procedure

2.2.1. Crystalline structure

X-ray diffraction (XRD) is a technique to study the crystalline structure, materials. During the measurement, a beam of X-ray is incident on the sample surface with an angle of θ. The crystal lattices interact with and scattered the X-Ray beam. The scattered X-ray beams from difference crystalline planes interfere with each other and thus the intensity of the resultant X-Ray beam varies with the incident angle due to the constructive or destructive interferences. The profile of the intensity of the X-ray beam versus the incident angle is called XRD pattern. By analyzing the XRD pattern, the crystalline structure can be determined. According to the Bragg law, the diffraction peaks appear when the incident angle of X-ray satisfies the following condition:

$$2d_{hkl}sin\theta_{hkl} = n\lambda \qquad (2.1)$$

where h,k,l are the Miller indices, d_{hkl} is the interplanar spacing of {hkl} set of lattice planes, θ_{hkl} is the incident angle, n is the order of diffraction, and λ is the wavelength of the X-ray.

In this study, the powder form samples were used for the XPD analysis. The as-prepared ceramics were first grinded and sieved through an 80-mesh screen. An X-Ray diffractometer (SmartLab, Rigaku Co., Japan) with Cu Kα (λ = 1·5418 Å) radiation was used for the measurement.

2.2.2. Dielectric properties

The ceramic samples were polished using sandpapers to obtain flat and smooth surfaces. The polished ceramic was then coated fired-on silver electrode on both surfaces at 750°C for 30 min for the measurements of dielectric, piezoelectric and ferroelectric properties.

2.2.2.1. Dielectric constant and dielectric loss at room temperature

The dielectric constant (ε_r) and dielectric loss (tan δ) of samples were measured at 1 kHz using an impedance analyzer (HP 4294A, Agilent Technologies Inc., Palo Alto, CA) at room temperature. The dielectric constant is also known as relative permittivity, which is calculated from:

$$C = \frac{\varepsilon_o \varepsilon_r A}{d} \tag{2.2}$$

where C is the capacitance, ε_o is the permittivity of vacuum (~8.85×10^{-12} F/m), A and d are the electrode area and thickness of the sample. ε_r can be expressed as $\varepsilon_r = \varepsilon' + i\varepsilon''$, where ε' and ε'' are the real and imaginary parts of the relative permittivity, respectively. tan δ is then given as:

$$\tan\delta = \frac{\varepsilon''}{\varepsilon'} \tag{2.3}$$

Especially for tan δ, the dielectric property can indicate the quality of ceramics for practical uses.

2.2.2.2. Temperature dependence of dielectric properties

The ceramic samples were placed on a temperature-controlled probe stage (HFS600E-PB4, Linkam Scientific Instrument, UK) and connected to the impedance analyzer for the measurement of the temperature dependence of dielectric properties. A LabVIEW program was used to control the measurement stage and record the data. The temperature varies from -100˚C to 200 ˚C at a heating rate of 1 ˚C/min. The schematic diagram of the experimental setup is showed in Figure 2-5

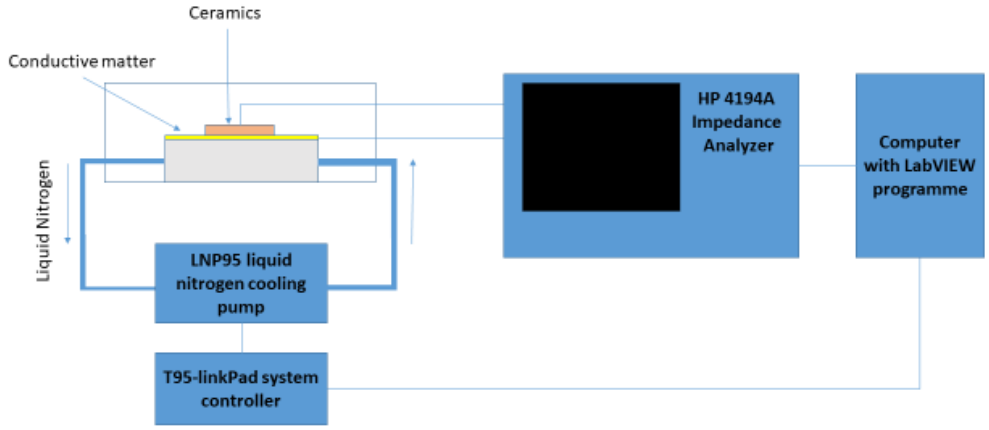

Figure 2-5 The schematic diagram of equipment setup for the temperature dependence dielectric measurement.

2.2.3. Ferroelectric properties (P-E loop)

As mentioned in Chapter 1, polarization-electric field (P-E) hysteresis loops are used to examine the ferroelectric properties of ceramics, including the spontaneous polarization (P_s), remnant polarization (P_r) and coercive field (E_c). In this study, the PE loop of ceramics were measured by a modified Sawyer-Tower circuit at 100 Hz. As shown in Figure 2-6, a function generator is used to produce a AC voltage signal which is then amplified for 2000 times by an amplifier (Trek 609D-6) and applied to the sample. A reference capacitor, which has a capacitance 1000 times smaller than that of the ceramic samples, is used to collect the charges generated from ceramic sample. A digital oscilloscope (HP 54645A, Agilent Technologies Inc., USA) is used to measure the voltages across the sample and the reference capacitor. For preventing electrical breakdown, the ceramic is immersed in silicone oil during the experiment. The polarization (P) of ceramics can be calculated from the voltage (V_o) across the reference capacitor as:

$$P = \frac{C_R V_o}{A} \tag{2.4}$$

where A is the area of electrode and C_R is the capacitance of reference capacitor.

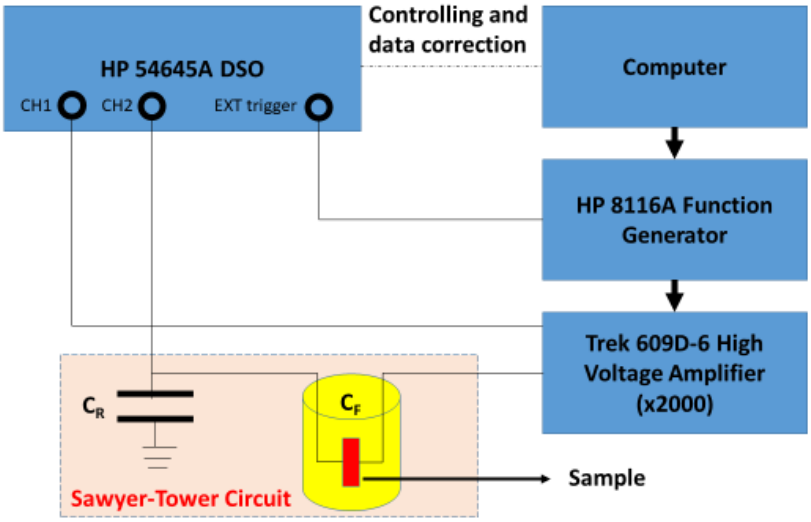

Figure 2-6 The schematic diagram of PE loop measurement setup.

2.2.4. Piezoelectric properties

Before measuring the longitudinal piezoelectric properties (d_{33}), the samples coated with silver electrodes were poled under a DC E field of 3 kV/mm in a silicone oil bath at room temperature for 30 min. The schematic diagram of the poling setup is shown in Figure 2-7. After poling, the d_{33} of samples was measured using a piezo d_{33} meter (ZJ-3B, Institute of Acoustics Academia Sinica).

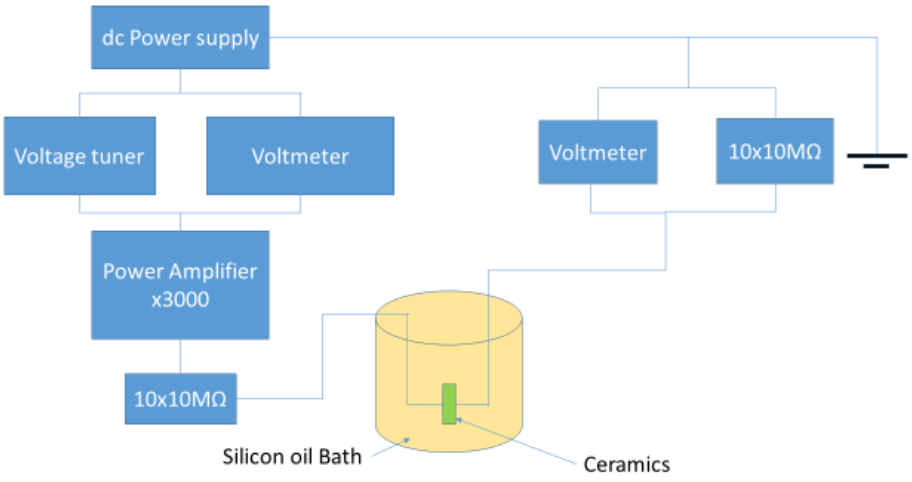

Figure 2-7 The schematic diagram of poling

2.2.5. Optical band gap estimation

Due to the advantage of insensitivity to surface defects, diffuse reflectance spectroscopy was chosen for the optical band gap estimation [85]. The top view of the diffuse reflectance measurement set up is shown in Figure 2-8.

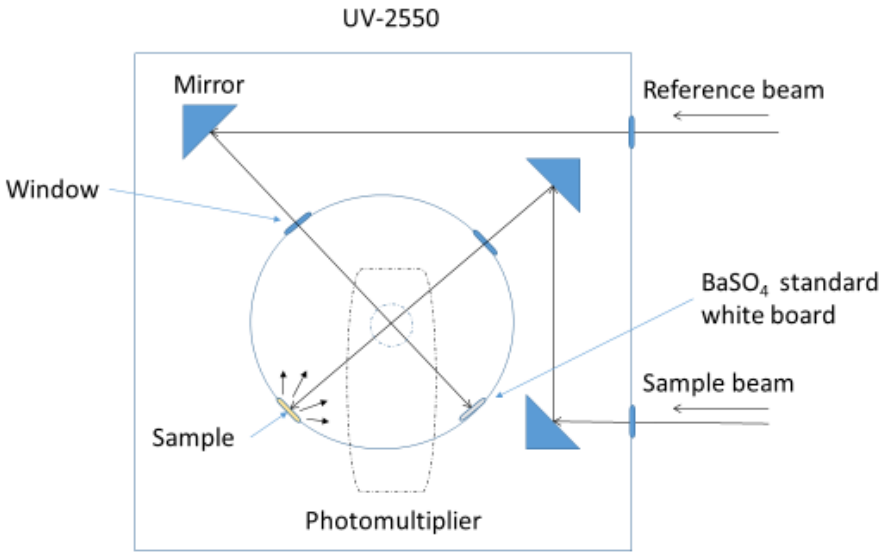

Figure 2-8 The top view of diffuse reflectance measurement set up.

The diffuse reflectance of the powder samples was measured in the range of 300-800 nm using an UV-Vis spectrophotometer (UV—2550, Shiadzu Co.). BaSO4 powder was used as a non-absorbing standard. The absorption coefficient of samples was calculated using the Kubelka-Munk (K-M) function based on the reflectance data [86]:

$$F(R) = \frac{(1-R)^2}{2R} = \frac{K}{S} \qquad (2.5)$$

where R is the observed reflectance, K and S are the absorption and scattering coefficients, respectively. Assuming that the scattering coefficient S is wavelength independent, F(R) is proportional to K. After that, Tauc's plot was used to estimate the optical band gap. The Tauc equation is expressed as follow [85]:

$$(h\nu\alpha)^{1/n} = A(h\nu - Eg) = [h\nu F(R)]^{1/n} \qquad (2.6)$$

where h is the Planck constant, v is the frequency of vibration, α is the absorption coefficient, Eg is the band gap, and A is a proportional constant. The value of the exponent n depends on the type of the transition. For the direct allowed transition, n= 0.5, while n = 2 for the indirect allowed transition. Together with Equation 2.5, the optical band gap value was determined as the x-intercept of the extrapolation of the Tauc's plot. A typical tauc' plot is shown in Figure 1-13 in chapter 1.

2.2.6. Photovoltaic response

Both the in-plane and parallel-plate electrodes are used to examine the photovoltaic performance of the ceramics.

A solar simulator (Newport 91160,300W) was used as a light source of AM1.5 (100 mW/cm^2). The AM1.5 standard spectrums, which corresponds to the sunlight received at an angle of 48.19° from zenith, is a common illumination for solar cell characterization. The output current and voltage of the samples were measured using a source meter

(Keithley 2410) and recorded by a computer together with a LabVIEW program. The light intensity was calibrated by a standard silicon solar cell.

The wavelength dependence of the photovoltaic response of the samples was measured using a standard system which includes a Xenon Lamp (Oriel 66902,300W) and a monochromator (Newport 66902). The intensity of the monochromatic light, which came from a narrow aperture, was recorded by a dual channel power meter (Newport 2931_C) together with a Si detector (Oriel 76175_71580). During the measurement, the sample was fixed on the holder and placed at the position the same as photodetector. It ensures that the intensity of light received by the sample is the same as that in the calibration. A schematic diagram of the wavelength dependence photovoltaic measurement is shown in Figure 2-9.

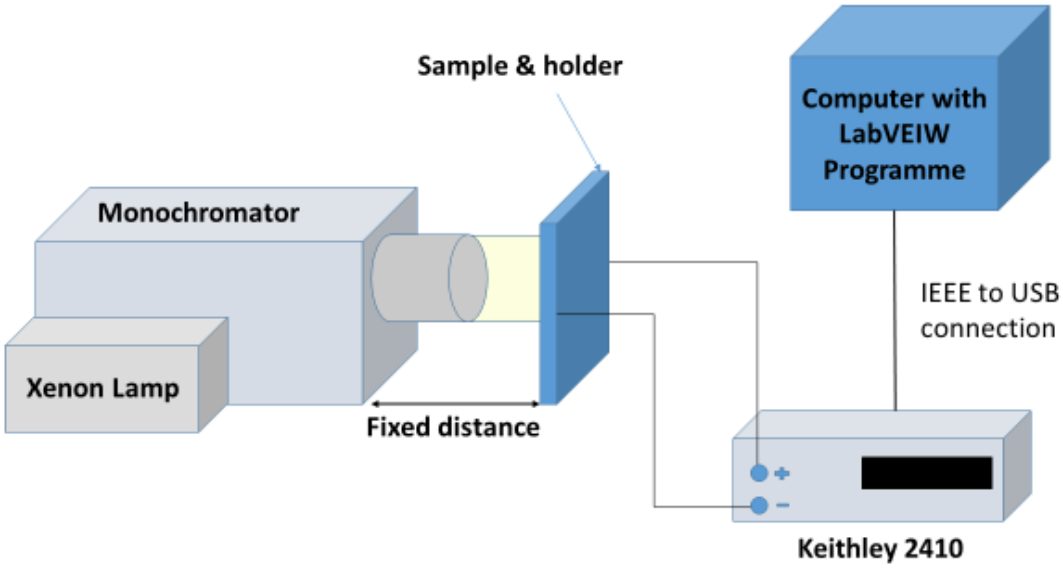

Figure 2-9 Schematic diagram of wavelength dependence photovoltaic measurement.

Chapter 3 BCTSn-0.1-0.1/BCTFe-0.1-x Ceramics

3.1. Introduction

As discussed in Chapter 1, the optical band gap reduction of ferroelectric oxides via chemical doping is an attractive research topic for enhancing the performance of the ferroelectric photovoltaic effect [3, 54, 57]. Previous studies have reported that a reduction of the optical band gap can be achieved by doping transition metals with high electronegativity into the B-site of perovskite ferroelectric oxides, although the new systems also shows a severe degradation of ferroelectric properties [70, 73, 87]. In most of the optical band gap modulation works, the new compositions always end up with a lower optical band gap but inferior ferroelectric properties.

In this chapter, $Ba_{0.9}Ca_{0.1}Ti_{0.9}Sn_{0.1}O_3$ (BCTSn-0.1-0.1) ceramics are used as the starting ferroelectric oxide for the optical band gap modulation because of its good ferroelectric and piezoelectric properties (d_{33} ~520 pC/N) [27]. It is believed that the (total) replacement of Sn^{4+} with the high electronegativity transition metal Fe^{3+} will not affect the ferroelectric properties significantly due to the similar ionic radii of Sn^{4+} and Fe^{3+}. The new ceramics $Ba_{0.9}Ca_{0.1}Ti_{1-x}Fe_xO_{3-\delta}$ (abbreviated as BCTFe-0.1-x) with x=0.1, 0.5 and 0.025 have been prepared by a solid-state reaction (SSR) method. The optimum sintering temperature has been determined as 1450 ˚C. The crystalline structure of the BCTFe-0.1-x ceramics have been investigated for confirming the perovskite structure and ferroelectric phase of the ceramics. Besides, the effects of the doping level of Fe^{3+} on dielectric, piezoelectric and ferroelectric properties together with the optical band gap value have been examined. On the basis of the results, the optimal composition has been determined for the studies of ferroelectric photovoltaic responses.

3.2. Crystalline structure

The XRD patterns of the BCTSn-0.1-0.1 and BCTFe-0.1-x ceramics measured in the range of 20° to 80° are shown in Figure 3-1(a) for revealing the formation of the polycrystalline perovskite structure of the ceramics. No additional peaks related to secondary phases are observed within the detection limit of XRD, suggesting that both Sn^{4+} and Fe^{3+} have diffused into the Ba0.9Ca0.1TiO3 (BCT) lattices, respectively, to form a new homogenous solid solution. Figure 3-1(b) shows an expansion of the (200) peak for further analysis. A dotted line is added for showing the shifting of the (200) peak. Similar to previous results, the broad peak of the BCTSn-0.1-0.1 ceramic at 45-46° is resulted from the coexistence of the orthorhombic and tetragonal phases [27].

Besides, after replacing Sn^{4+} with Fe^{3+} in the BCT system, the (200) peak of the BCTFe-0.1-0.1 ceramic is shifted towards a larger angle. Considering the ionic radius and charge difference between Sn^{4+}(r=0.69 Å) and Fe^{3+}(r=0.645 Å), the shifting should be resulted from the shrinkage of the lattices arisen from the smaller ion radii of Fe^{3+} and formation of oxygen vacancies [26, 88, 89]. In addition, when the content of Fe^{3+} is reduced from 0.1 mol to 0.025 mol, the (200) peak shift towards larger angles continually. This should be due to the increase of the Ti^{4+} content. Ti^{4+} is smaller (0.605 Å) than Fe^{3+}, and thus the lattice shrinkage increases with increasing the content of Ti^{4+} or decreasing the content of Fe^{3+}.On the other hand, the BCTFe-0.1-0.1 and BCTFe-0.1-0.05 ceramics exhibit a relatively sharp and symmetric peak at 45-46°. Even after enlarging the pattern, no splitting of the (110) and (111) peaks are observed, implying a cubic-like or pseudo-cubic symmetry of the ceramics. It has been known that the doping of Fe^{3+} in $BaTiO_3$ may induce distortion of the tetragonal structure [88,90]. Similarly, the BCTFe-0.1-0.1

and BCTFe-0.1-0.05 ceramics may transform from a ferroelectric tetragonal phase to a paraelectric cubic phase at room temperature due to the high doping levels of Fe^{3+}. Additional evidence of the paraelectric cubic phase for the two ceramics will be provided from the experimental results of the temperature dependences of the dielectric constant and dielectric loss, which will be discussed in the following section. By reducing the doping level of Fe^{3+} to 0.025 mol, the (200) peak becomes split, comprising the (002) and (200) peaks attributed to the tetragonal structure. It has been known that BCT possessed a tetragonal symmetry suggesting that doping 0.025 mol of Fe^{3+} into BCT has not affected the crystal structure significantly [27]. The tetragonal symmetry nature is also obtained on another Fe-doped BCT system [91].

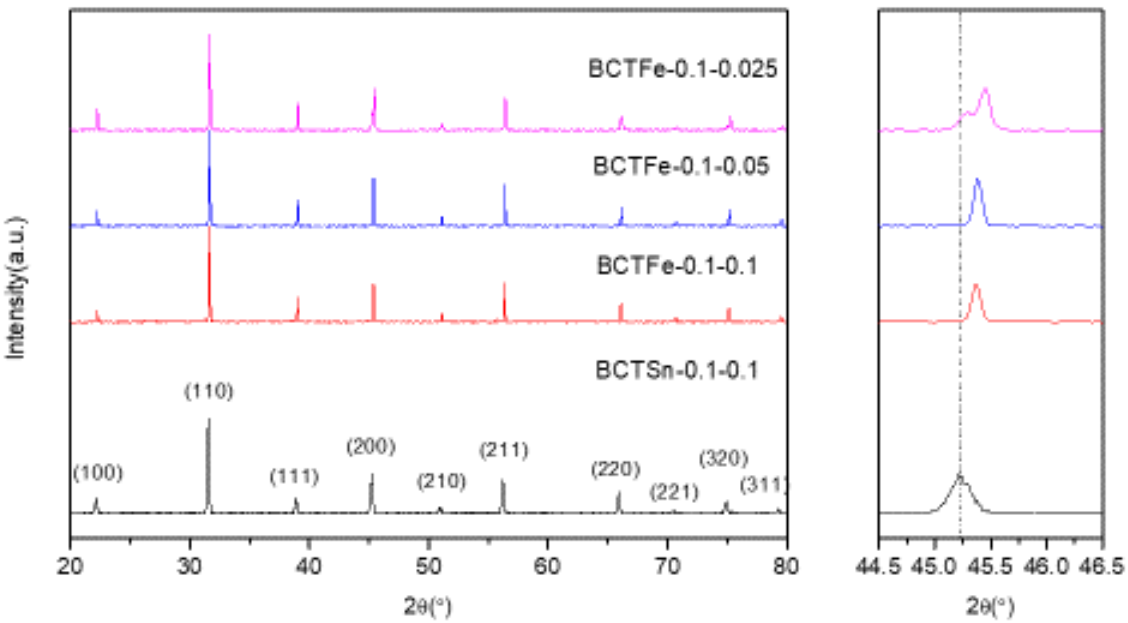

Figure 3-1 The XRD patterns of the BCTSn-0.1-0.1 and BCTFe-0.1-x ceramics in the range of (a) 20°-80° and (b) 44.5°-46.5°.

3.3. Dielectric properties

3.3.1. Dielectric constant and dielectric loss

The dielectric constant (ε_r) and dielectric loss (tan δ) of the BCTSn-0.1-0.1 and BCTFe-0.1-x ceramics are measured at room temperature and 1 kHz are summarized in Table 3-1. The observed ε_r (8400) and tan δ (1.9%) of the BCTSn-0.1-0.1ceramic are comparable to those reported in previous studies [27], suggesting that the ceramic is well sintered and of good quality. By replacing Sn^{4+} with Fe^{3+}, the observed ε_r of the BCTFe-0.1-0.1 ceramic decreases greatly to 700. When the doping level of Fe^{3+} is reduced to 0.05 mol, the observed ε_r increases significantly to 3500. However, when the doping level is further reduced to 0.025, the observed ε_r increases only slightly to 3800. Such a "non-regular variation" of ε_r can be understood in terms of the phase transition of the ceramics, which will be discussed in the following section. Nevertheless, all the ceramics exhibited a low dielectric loss (<3 %), indicating that they are dense and suitable for practical applications [1].

Table 3-1 The dielectric constant (ε_r) and dielectric loss (tan δ) of the BCTSn-0.1-0.1 and BCTFe-0.1-x ceramics at room temperature and 1 kHz.

Sample	ε_r	tan δ (%)
BCTSn-0.1-0.1	8400	1.9
BCTFe-0.1-0.1	700	2.3
BCTFe-0.1-0.05	3500	0.6
BCTFe-0.1-0.025	3800	1.2

3.3.2. Temperature dependence of dielectric properties

The temperature dependences of ε_r and tan δ for the BCTSn-0.1-0.1 and BCTFe-0.1-x ceramics measured at 1 kHz, 10 kHz and 100 kHz in a temperature range of 25°C to 150°C are shown in Figure 3-2. A phase transition peak is observed at 57°C for the BCTSn-0.1-0.1 ceramic, which is consistent with the previous report [27]. No transition peaks are observed for both the BCTFe-0.1-0.1 and BCTFe-0.1-0.05 ceramics in the temperature range studied. The temperature has been extended to 300°C for searching the phase transition (data not shown); but the ceramics became very leaky (i.e., tanδ >100%) . It has been shown that high doping level of Fe^{3+} can lower the transition temperature of BTO-based systems significantly [92]. Therefore, it is suggested that the Curie temperature of the BCTFe-0.1-0.1 and BCTFe-0.1-0.05 ceramics should be below room temperature. This is consistent with the XRD results that the ceramics should be in the cubic phase at room temperature. On the other hand, when the doping level of Fe^{3+} is reduced 0.025 mol, the observed ε_r achieve a maximum at 53 °C. Combining with the XRD analysis, it should be associated with a transition from ferroelectric tetragonal phase to paraelectric cubic phase.

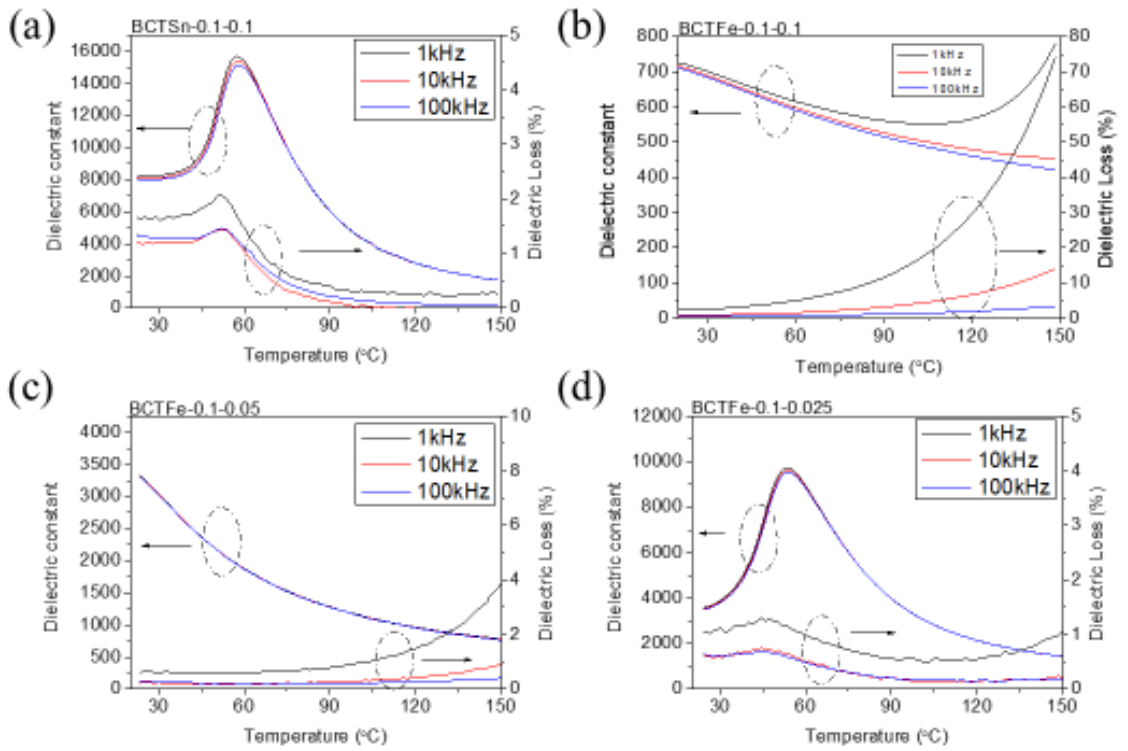

Figure 3-2 Temperature dependence of dielectric properties of (a) BCTSn-0.1-0.1, (b) BCTFe-0.1-0.1, (c)BCTFe-0.1-0.05, (d)BCTFe-0.1-0.025 ceramics.

For confirming the phase transition of the BCTFe-0.1-x ceramics, the temperature range for the dielectric measurement has been extended to -100°C, giving the results shown in Figure 3-3. For the BCTFe-0.1-0.025 ceramic, in addition to the Curie transition peak at 55°C, a weak ε_r peak is observed at -50°C. With reference to the phase transitions of BTO [93], it should be associated with a transition from tetragonal phase to orthorhombic phase. As shown in Figure 3-3, the Curie transition temperature of the ceramics shifts to lower temperatures with increasing the doping level of Fe^{3+}. The transition temperature of the BCTFe-0.1-0.05 ceramic is around -25°C, whereas that of the BCTFe-0.1-0.1 ceramic is most likely below -100°C. Consequently, both the BCTFe-0.1-0.1 and BCTFe-0.1-0.05 ceramics are non-ferroelectric at room temperature, while the BCTFe-0.1-0.025 ceramic remains ferroelectric. The shifting of the transition

temperature should also be the cause for the "non-regular variation" of ε_r shown in Table 3-1.

Figure 3-3 also illustrates that the Curie transition peak of the BCTFe-0.1-0.05 ceramic is broader than that of the BCTFe-0.1-0.025 ceramic. In the BCTFe-0.1-x ceramics, part of Ti^{4+} is replaced with Fe^{3+}, and thus oxygen vacancies should be formed due to the charge imbalance. Under the same fabrication conditions, a larger amount of oxygen vacancies should be formed in the BCTFe-0.1-0.05 ceramic as compared with the BCTFe-0.1-0.025 ceramic due to the higher doping content of Fe^{3+}. Such oxygen vacancies should play a role as disorder dipole inside the materials, and thus a broadened transition temperature peak is observed in the BCTFe-0.1-0.05 ceramic [73]. Similar results have been reported for Fe-doped BCT ceramics [91].

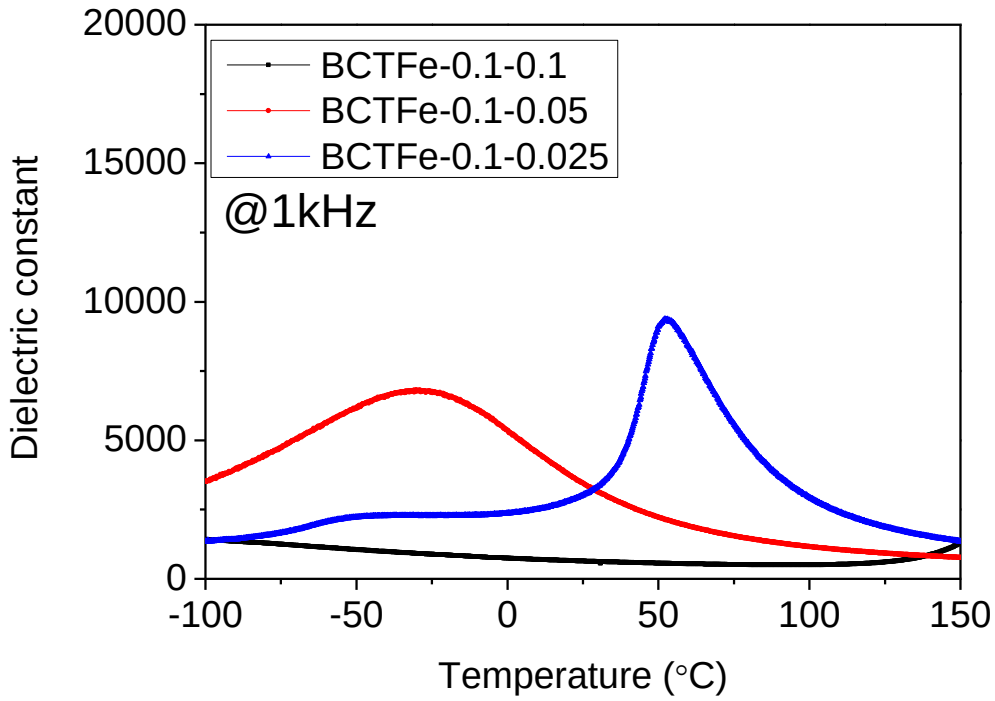

Figure 3-3 Temperature dependence of dielectric constant of BCTFe-0.1-x ceramics at 1 kHz.

3.4. Ferroelectric properties

The P-E loops of the BCTSn-0.1-0.1 and BCTFe-0.1-x ceramics measured under an E field of 3 kV/mm at 100 Hz are shown in Figure 3-4. The observed saturated polarization (P_s), remnant polarization (P_r) and coercive field (E_c) are listed in Table 3-2. The P-E loop of the BCTSn-0.1-0.1 ceramic is similar to that reported in the previous study, although the observed P_r is slightly lower (6.0 μC/cm^2 vs 6.2 μC/cm^2) [27]. As shown in Figure 3-4, the observed P_r of the BCTFe-0.1-0.0.5 and BCTFe-0.1-0.1 ceramics are almost zero, confirming their cubic structures at room temperature. On the other hand, because of the ferroelectric tetragonal structure, the BCTFe-0.1-0.025 ceramic exhibits a large P_r (4.5 μC/cm^2) and P_s (18.5 μC/cm^2), which are helpful for separating the photo-generated electron-hole pairs in the ferroelectric photovoltaic effect.

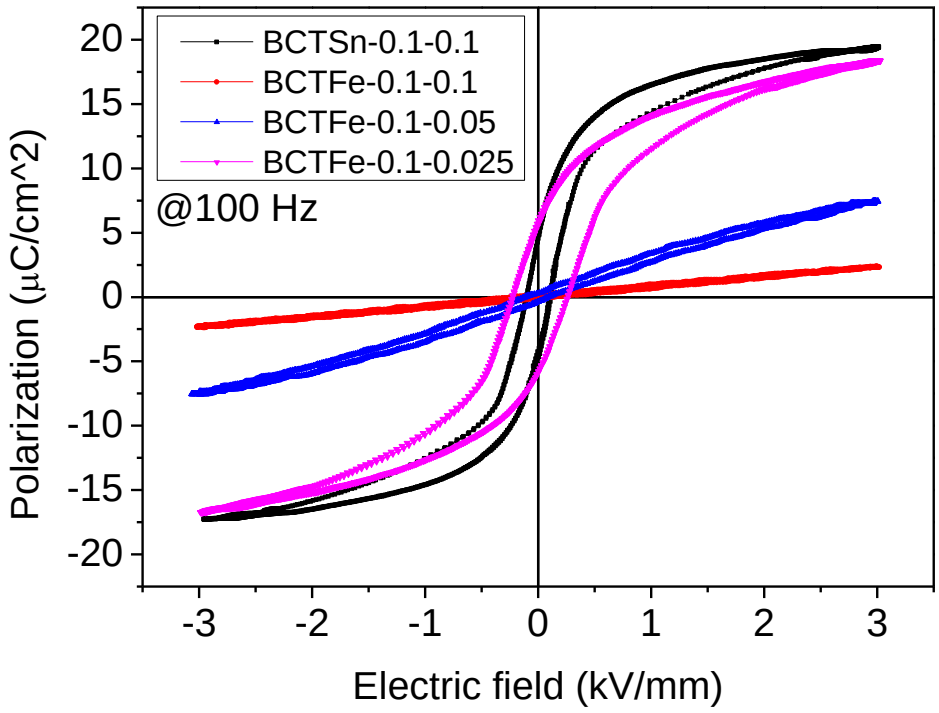

Figure 3-4 PE loop of the BCTSn-0.1-0.1 and BCTFe-0.1-x ceramics

On the other hand, the BCTFe-0.1-0.025 ceramic exhibits a higher E_c as compared to BCTSn-0.1-0.1. This should be attributed to the oxygen vacancies which will form defect dipoles hindering the switching of the polarizations and thus making the ceramic to become hardened [94, 95].

Table 3-2 ferroelectric properties of the BCTSn/Fe ceramics

Sample	P_r (μC/cm^2)	P_s (μC/cm^2)	E_c (kV/mm)
BCTSn-0.1-0.1	6.0	19.4	0.11
BCTFe-0.1-0.1	0.1	2.2	0.22
BCTFe-0.1-0.05	0.3	7.4	0.11
BCTFe-0.1-0.025	4.5	18.5	0.25

3.5. Piezoelectric properties

The piezoelectric coefficients (d_{33}) of the BCTSn-0.1-0.1 and BCTFe-0.1-x ceramics are summarized in Table 3-3. As evidenced by the results of XRD, temperature dependence of dielectric constant and P-E loop measurements, the BCTFe-0.1-0.1 ceramic is non-ferroelectric at room temperature and thus exhibit a zero d_{33} at room temperature. As the doping level of Fe^{3+} decreases to 0.05 mol, the transition temperature shifts to near the room temperature. Although it should be non-ferroelectric as shown by the results of XRD and P-E loop measurements, a small d_{33} of 5 pC/N is obtained. Indeed, the phase transition of the BCTFe-0.1-0.05 ceramic is relatively board, suggesting a coexistence of the tetragonal and cubic phases at room temperature [96]. As a result, a

weak piezoelectricity remained in the ceramic. Both the BCTSn-0.1-0.1 and BCTFe-0.1-0.025 ceramics are ferroelectric and thus exhibit a large d_{33} of 300 pC/N and 190 pC/N, respectively. Among the samples, the BCTFe-0.1-0.025 and BCTSn-0.1-0.1 ceramics show promising piezoelectric properties for practical applications.

Table 3-3 The piezoelectric coefficient (d33) of BCTSn-0.1-0.1 and Fe-0.1-x ceramics

	BCTSn-0.1-0.1	**BCTFe-0.1-0.1**	**BCTFe-0.1-0.05**	**BCTFe-0.1-0.025**
d_{33}(pC/N)	300	0	5	190

3.6. Optical band gap estimation

3.6.1. Reflectance of BCTSn/Fe-0.1-x ceramic powder

The diffuse reflectance spectra of the BCTSn-0.1-0.1 and BCTFe-0.1-0.025 ceramics, in powder form, are shown in Figure 3-5, in which the spectrum of a $0.94Bi_{0.5}Na_{0.5}TiO_3$-$0.06BaTiO_3$ (BNT-6BT) ceramic is plotted for comparison. The reflectance of the BCTSn-0.1-0.1 ceramic increases rapidly from ~360 nm and reaches above 90% at wavelengths > 450 nm, suggesting that it only absorbs the violet region of the visible spectrum, which is normal for typical ferroelectric oxides [47, 64]. On the other hand, for all the BCTFe-0.1-x ceramics the reflectance is low in the whole range of the visible spectrum. At each wavelength, the reflectance decreases with increasing the doping level of Fe^{3+}.

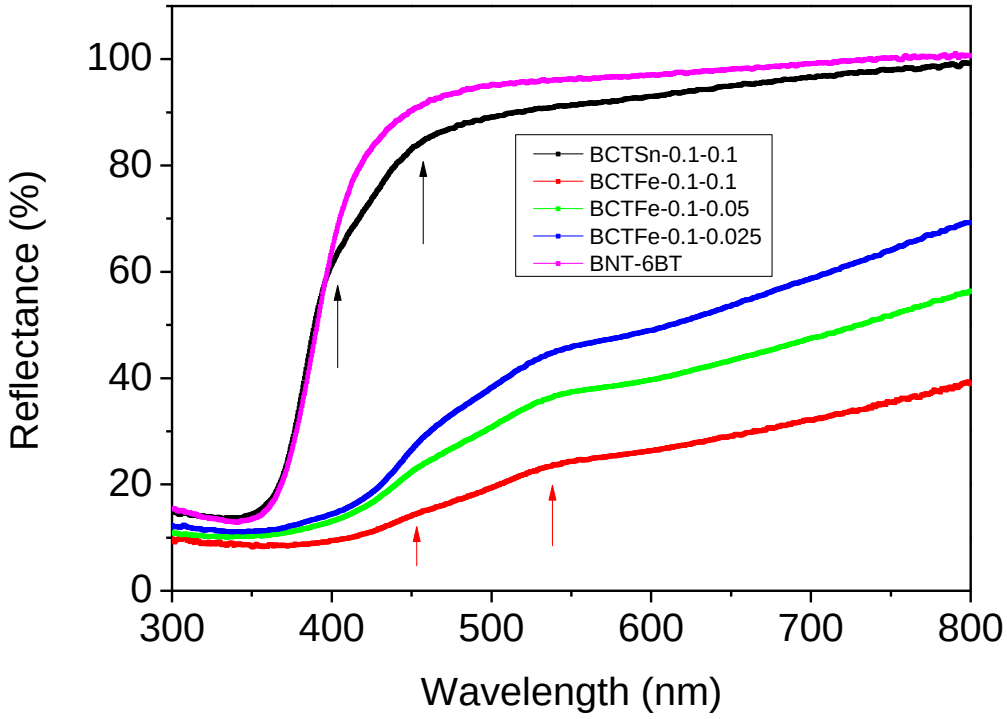

Figure 3-5 Diffuse reflectance spectral of BCTSn-0.1-0.1 and BCTFe-0.1-x ceramics.

As discussed in Section 3.3.2, because of the valence difference and charge neutralization, oxygen vacancies are formed in the BCTFe-0.1-x ceramics. Because of the oxygen vacancies, band tail states are formed on top of the valence band [97, 98]. Therefore, the low reflectance of the ceramics should be attributed to the presence of oxygen vacancies. The more the vacancies, the lower the reflectance. Similar effects of oxygen vacancies on the reflectance have been reported for Ni/Nb-codoped BTO ceramics [76].

Two shoulders are observed for all the ceramics, which are indicated by black and red arrows for the BCTSn-0.1-0.1 and BCTFe-0.1-x ceramics, respectively, in Figure 3-5. Unlike the ceramics, the reflectance of the BNT-6BT ceramic exhibits a sharp and smooth reduction of reflectance in the wavelength range from 350 nm to 450 nm. The BNT-6BT ceramic contains a single type of transition metal, i.e., Ti^{4+} in the B-sites, while

the BCTSn-0.1-0.1 ceramic contains two types, i.e., Ti^{4+} and Sn^{4+}. Therefore, it is suggested that the shoulders are contributed to the absorptions from the O 2p state at the top of the valence band to the Ti 3d and Sn 3d hybridized state at the bottom of the conduction band. Similar results have been reported for $(Ba,Ca)TiO_3$-$Ba(Sn,Ti)O_3$ ceramics [99].

For the BCTFe-0.1-x ceramics, the increase of the reflectance is not as sharp as that in the BCTSn-0.1-0.1 ceramic, which should be due to the presence of oxygen vacancies. Moreover, the shoulders shift to longer wavelengths, i.e., from the violet region to the green region. It has been shown by the fist-principles calculation that the Fe 3d state will associate with the defect band and appears between the Ti 3d state and O 2p state when Fe is doped into BTO [100, 101, 102]. The calculations have also predicted a redshift of the absorption spectra for Fe-doped BTO ceramics. Therefore, the shoulders for the BCTFe-0.1-x ceramics should be attributed to the charge transfer from the Fe 3d state to O 2p state.

3.6.2. Tauc's plot of BCTSn-0.1-0.1 and BCTFe-0.1-0.025

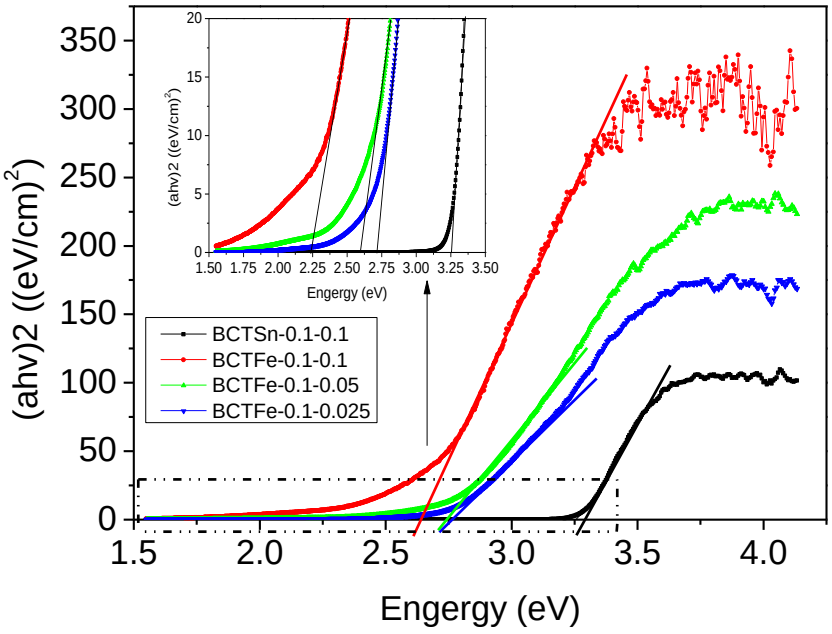

Figure 3-6 Tauc's plot of BCTSn-0.1-0.1 and BCTFe-0.1-x ceramics

The optical band gap of the BCTSn-0.1-0.1 and BCTFe-0.1-x ceramics is estimated from the diffuse reflectance spectra. The Kubelka-Munk (K-M) function has been used to calculate the absorption coefficient from the reflectance and then the Tauc's plots as shown in Figure 3-6. According to Tauc's model, the direct optical band gap is determined as the x-intercept of the extrapolation of the Tauc's plot [103]. For the BCTSn-0.1-0.1 ceramic, owing to the strong absorption in the violet region, a linear fitting is easily achieved, and the estimated optical band gap is 3.30 eV. However, for the BCTFe-0.1-x ceramics, the initial linear region of the curve is ambiguous due to the presence of oxygen vacancies and the relatively weak absorption in the region between 450 nm and 550 nm. As shown in the inset of Figure 3-6, the x-intercept is shifted towards lower photon energies $(h\nu)$ after enlarging the scale of $(h\nu\alpha)^2$. As a result, the estimated

optical band gap of the BCTFe-0.1-x ceramics varies a lot with the scale of $(h\nu\alpha)^2$, while the variation for the BCTSn-0.1-0.1 ceramic is not significant (≤0.05 eV). The variations of the estimated optical band gap are summarized in Table 3-4. The estimated direct optical band gap of the BCTFe-0.1-x ceramics are 2.64 eV, 2.74 eV and 2.78 eV for x = 0.1, 0.05 and 0.025, respectively. Unfortunately, most of the previous works have not discussed the dependence of the optical band gap on the scale of $(h\nu\alpha)^2$[70,73,74]. Therefore, the optical band gap of the BCTFe-0.1-x ceramics will be further confirmed based on their photovoltaic responses.

Table 3-4 Estimated optical band gap of BCTSn-0.1-0.1 and BCTFe-0.1-x samples

	BCTSn-0.1-0.1	**BCTFe-0.1-0.1**	**BCTFe-0.1-0.05**	**BCTFe-0.1-0.025**
E_g (eV)	3.30	2.64	2.74	2.78
ΔE_g(eV)	0.05	0.4	0.12	0.05

3.7. Conclusions

BCTSn-0.1-0.1 and BCTFe-0.1-x ceramics have been successfully fabricated by a solid-state reaction method. Within the detection limit of XRD, no additional peaks are observed, indicating that the ceramics have crystallized in a pure perovskite structure. Together with the results of the dielectric, piezoelectric and ferroelectric properties, the ferroelectric tetragonal to non-ferroelectric cubic phase transition of the BCTFe-0.1-x ceramics has been investigated. The observed Curie temperature is 53°C for the BCTFe-0.1-0.025 ceramic and decreases with increasing the doping level of Fe^{3+}. Because of the ferroelectric tetragonal structure at room temperature, the BCTFe-0.1-0.025 ceramic

exhibit a large d_{33} (190 pC/N) and P_r (4.5 μC/cm^2), which are comparable to those of the BCTSn-0.1-0.1 ceramic (300 pC/N and 6 μC/cm^2). On the other hand, the absorption edge of the ceramics shows a redshift from 450 nm to 550 nm after replacing Sn^{4+} with Fe^{3+}. The optical band gap of the BCTFe-0.1-x ceramics decreases with increasing the doping level of Fe^{3+}. The BCTFe-0.1-0.025 ceramic thus exhibits the optimized properties for photovoltaic responses, i.e., a low optical band gap (2.78 eV) and good piezoelectric properties (190 pC/N).

Chapter 4 Ferroelectric Photovoltaic effect on BCTSn-0.1-0.1/BCTFe-0.1-0.025 ceramics

4.1. Introduction

In Chapter 3, the influence of the dopant Fe^{3+} on the electric properties and optical properties of BCT system has been discussed, and the optimal composition showing a low optical band gap (2.78 eV) and a sufficiently large remnant polarization ($P_r \sim 4.5$ $\mu C/cm^2$) has been obtained, i.e., of BCTFe-0.1-0.025.

In this chapter, the study of the ferroelectric photovoltaic response of the BCTSn-0.1-0.1 and BCTFe-0.1-0.025 ceramics deposited with in-plane electrodes (i.e., IDE pattern of Au with 50 μm electrode gap) will be presented. The usage of the in-plane electrode is to rule out the interface effect (i.e. Schottky barriers) arisen form the asymmetry electrode configuration. It also allows the ceramics to be illuminated directly without any reduction arisen from the electrodes. The short-circuit current of the samples will be first examined under 1 sun illumination for demonstrating the ferroelectric photovoltaic response. The temperature effect (i.e, pyroelectric current) on the observed short-circuit current of the samples will be considered. Besides, the wavelength-dependent photovoltaic response will be examined using un-poled samples for confirming the optical band gap measurement. The usage of un-poled samples aims to exclude the pyroelectric current. Before the examination, the photocurrent of the un-poled samples under different electric fields will be measured for determining the bias electric field that is just large enough for producing an observable photocurrent for confirming the cut-off photon energy and then the optical band gap of ceramics.

BCTFe-0.1-0.025 and BCTSn-0.1-0.1ceramics with vertical electrodes of large area (i.e., 8 mm in diameter) will be also used for demonstrating the ferroelectric photovoltaic response. The samples have been thinned down to 100 μm and deposited with ITO electrodes on both surfaces before the measurement. Similarly, as the ITO electrode has been used on both surfaces, the interface effect arisen from Schottky barriers can be ruled out. The thin thickness (i.e., 100 μm) is beneficial for reaching thermal equilibrium. At last, the poling field-dependent ferroelectric photovoltaic current and the wavelength-dependent photovoltaic current of the BCTFe-0.1-0.025 and BCTSn-0.1-0.1 ceramics will be presented, based on which the switchable photocurrent is demonstrated.

4.2. Interdigitated electrode (IDE)

4.2.1. Ferroelectric photovoltaic response under 1 sun illumination for 30 s

Before the ferroelectric photovoltaic measurements, the samples are poled with an electric field of 3 kV/mm at room temperature. The poling field is defined as the poling voltage divided by the electrode gap (i.e., 50 μm) of the IDE pattern. The short-circuit current of the poled samples (without a bias electric field) is then measured under 1 sun illumination.

A schematic diagram showing the poling direction and the photocurrent direction is shown in Figure 4-1. The interdigital electrode (IDE) is simplified as a pair of parallel stripes. After poling, the observed positive photocurrent is in opposite direction of the poling field, which agrees with the literature report [104].

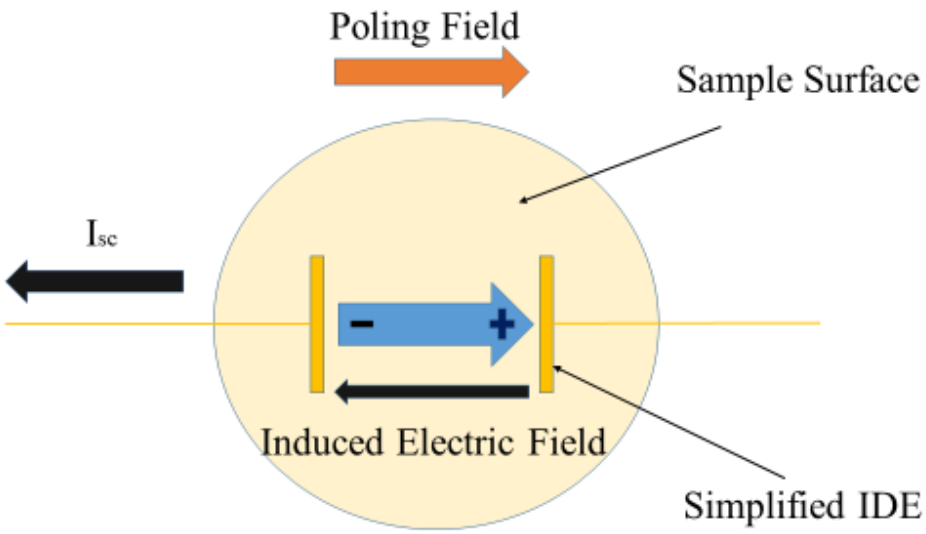

Figure 4-1 The simplified electrode structure of samples

Figure 4-2(a) shows the short-circuit current as a function of time for the BCTSn-0.1-0.1 and BCTFe-0.1-0.025 ceramics when the 1 sun illumination is repeatedly turned off (i.e., Off state) and on (i.e., ON states). Before poling, both the ceramics (as in the as-fabricated state) exhibit no photocurrent under the illumination, indicating that the Schottky barriers formed at the interfaces do not have contribution to the photo-response. After poling, the observed short-circuit current reaches a steady value of 0.07 nA and 0.22 nA for the BCTSn-0.1-0.1 and BCTFe-0.1-0.025 ceramics, respectively. As shown in Figure 4-2(a), both the BCSn-0.1-0.1 and BCTFe-0.1-0.025 ceramics exhibits a current peak at the beginning of the ON and OFF states. It has been known that poled ferroelectric oxides will exhibit the pyroelectric effect upon the change in temperature. When the temperature becomes steady, no pyroelectric current will be observed. As also mentioned in Section 1.1.2., the induced pyroelectric current is in opposite direction of the

polarization direction upon heating and vice versa. Therefore, the observed current peak for the poled ceramics should be contributed by the pyroelectric effect [105], and the photocurrent observed after the peak should be mainly originated from the ferroelectric photovoltaic effect [53]. This agrees with the temperature measurements on the sample surfaces under similar illumination conditions as shown in Figure 4-2 (b). It can be seen that the sample temperature does not saturate in the 30-s illumination period. Therefore, the observed short-circuit current for both the BCTFe-0.1-0.0.25 and BCTSn-0.1-0.1 ceramics should contain the pyroelectric current. In fact, there can be other factors contributing to the observed current peak. Because of the complicated distributions of the electric field and polarization orientation, the pyroelectric current is hard to estimate on the ceramic with the in-plane electrode. The contribution of the pyroelectric effect on the peak current will be further discussed in detail in section 4.3.1.

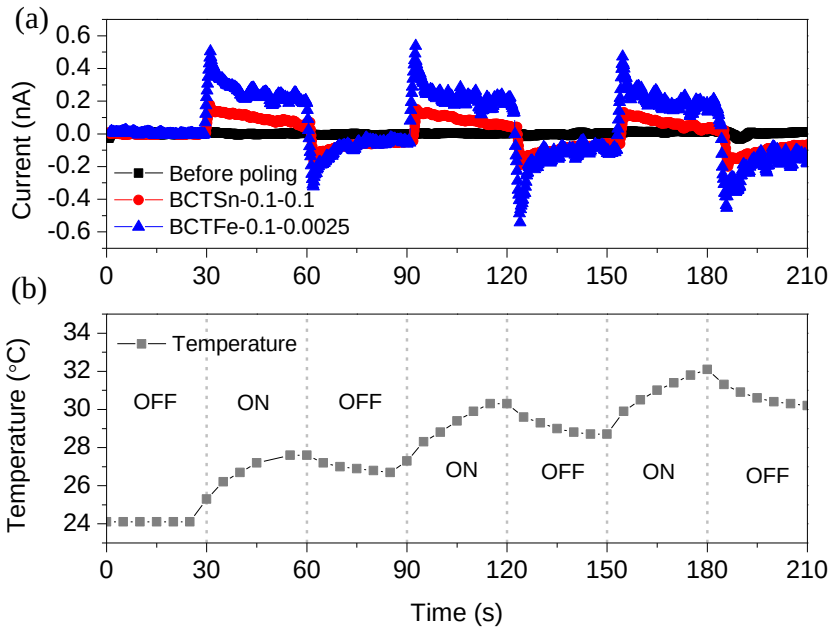

Figure 4-2 (a) The short circuit current of BCSn-0.1-0.1 and BCTFe-0.1-0.0025 poled at 3 kV/mm and the un-poled sample; (b) The temperature record of sample surface under 1 sun between On and Off.

4.2.2. Ferroelectric photovoltaic response under 1 sun illumination for 600 s

The illumination time has been prolonged to the 600 s with the expectation of allowing the ceramic surface temperature to become saturated and then eliminating the pyroelectric effect. The observed photocurrent for the BCTSn-0.1-0.1 and BCTFe-0.1-0.025 ceramics are shown in Figure 4-3(a) and (b), respectively, while the surface temperature is shown in Figure 4-3(c). Unfortunately, probably because of the high light intensity, the ceramic surface temperature does not saturate within the 600-s illumination period. Moreover, the observed photocurrent of the BCTSn-0.1-0.1 and BCTFe-0.1-0.025 ceramics become very noisy after 100 s of ON state, and that of the BCTSn-0.1-0.1 ceramic even becomes indistinguishable from the noise signal. As discussed in Section 3.3.2, a dispersive phase transition has been observed in both the BCTSn-0.1-0.1 and BCTFe-0.1-0.025 ceramics, indicating that they undergo a gradual change from the ferroelectric phase to the paraelectric phase near their Curie temperature, i.e., 57°C and 53°C, respectively. When the temperature increases to near the Curie temperature, the portion of the non-ferroelectric phase of the ceramic increases and thus the remnant polarization is weakened, which regarded as a depolarization process [62]. As a result, the observed peak current is weakening in the second illumination period due to the irreversible depolarization process. On the other hand, the change of the surface temperature is being stable under illumination and then resulted in weakening pyroelectric current. The observed current is disappearing during illumination because of the relatively weak photovoltaic response. These should be the reasons for the weakening and eventually “disappearing” of the observed photocurrent for the BCTSn-0.1-0.1 ceramic.

For the BCTFe-0.1-0.025 ceramic, because of the stronger photovoltaic response, i.e., showing a larger photocurrent as compared to the BCTSn-0.1-0.1 ceramic (0.22 nA vs 0.07 nA), the observed photocurrent can still be distinguished from the large noise signal in the prolonged illumination. An abnormal current peak (around 150 s after the illumination is turned on) is observed which is different from the typical photovoltaic current observed in other ferroelectric oxide systems [106, 107]. This may be attributed to the interrelationship of the pyroelectric effect and the ferroelectric photovoltaic effect. When the illumination is turned on, the BCTFe-0.1-0.025 ceramic is heated up, and then resulting in a pyroelectric current peak. After a while (e.g. the 50s), the heating rate becomes lower and thus observed current is weakened and decreases gradually before 100 s. Meanwhile, the ferroelectric photovoltaic response should exist at any time under illumination. The conductivity of the BCTFe-0.1-0.025 ceramic is increase upon illumination and then heating [108, 109]. According to Equation 1.4 discussed in Chapter 1, the short-circuit current increases when the conductivity increases. Therefore, the small (abnormal) current peak observed around 150 s is resulted from the increased conductivity. However, when the BCTFe-0.1-0.025 ceramic is heated up to near the Curie temperature (i.e., 53°C), it may be partially depolarized (i.e., weakened P_r), and thus resulting in a gradually decreasing photocurrent [37, 110]. This depolarization process is irreversible and then the observed current peaks in the consecutive cycle (e.g. at the 1200s and 1350s) is declined [111].

The illumination intensity has been reduced from 100 mW/cm^2 to 50 mW/cm^2 (data not shown) for lowering the sample temperature and then eliminating the pyroelectric effect. However, owing to the reduced light intensity, the observed photocurrent for both the ceramics decreases and becomes close to the detection limit of the Keithley 2410

source meter (i.e., 10 pA). Therefore, the approaches of elongating the illumination time or reducing the light intensity may not be appropriate for eliminating the pyroelectric effect so as to compare their ferroelectric photovoltaic effect. As the ceramics deposited with vertical electrodes exhibit larger photocurrents, they have been used for the investigation of the ferroelectric photovoltaic response which will be discussed later. Before that, the wavelength-dependent photovoltaic current of the poled and un-poled samples are presented.

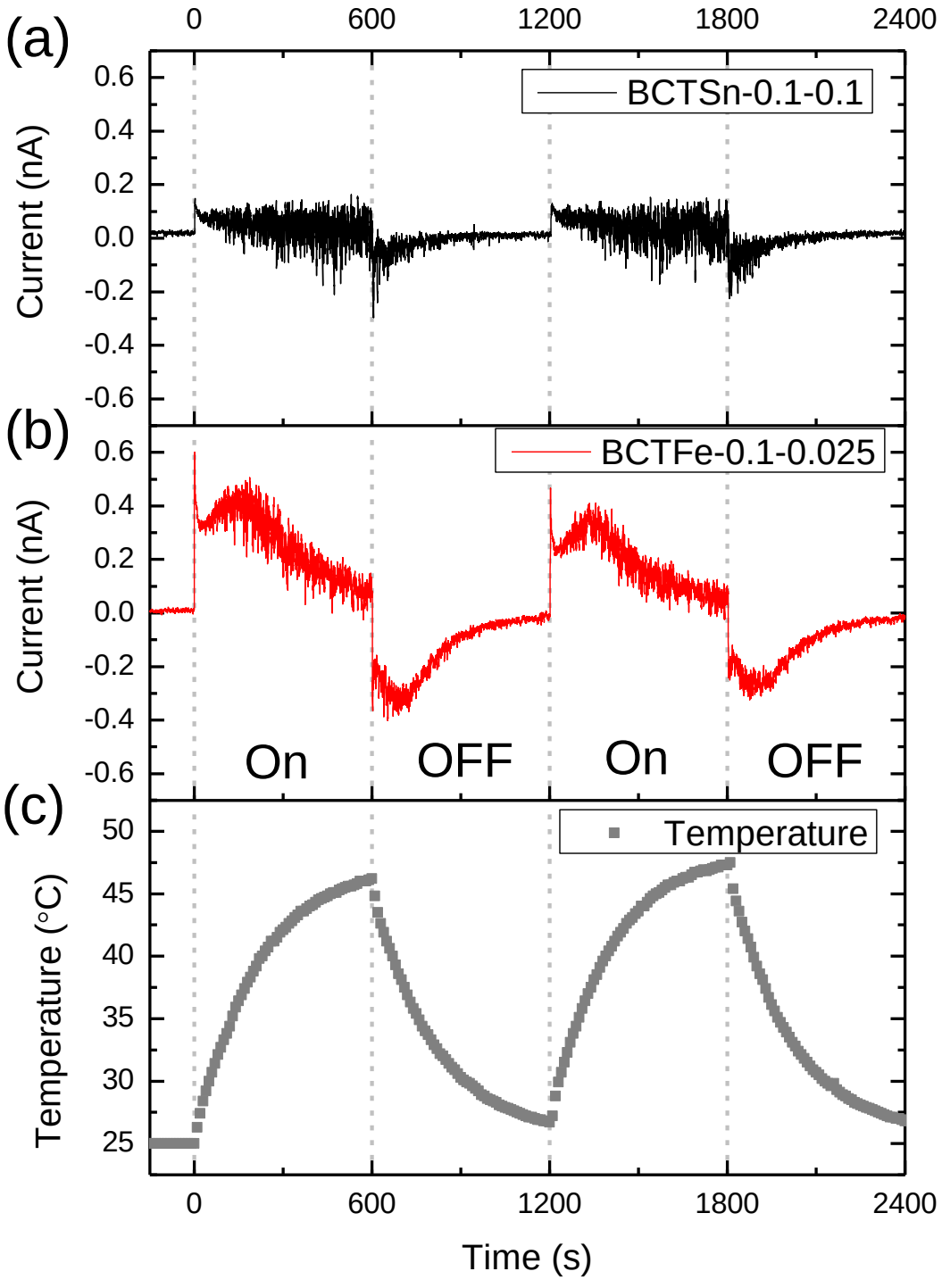

Figure 4-3 The short circuit current of (a)BCTSn-0.1-0.1 and (b) BCTFe-0.1-0.025 and (c) the temperature profile under A.M. 1.5 illumination.

4.2.3. Wavelength-dependent photovoltaic current of poled ceramics

The vibration of the wavelength-dependent photovoltaic current is commonly used as an alternative method for determining the optical band gap of materials [108, 112, 113]. Figure 4-4 shows the photocurrent of the BCTFe-0.1-0.025 poled ceramic under 1 sun illumination. Different band-pass filters with a bandwidth of 30 nm are inserted before the ceramic sample to limit the wavelength components of the illumination. Owing to the low light intensity, the observed photocurrent of the BCTFe-0.1-0.025 ceramic is weak and decreases quickly to zero after reaching a peak (arisen from the pyroelectric effect). Such a transient and weak photocurrent is observed for the wavelength ranging from 650 nm to 365 nm. Similar results (with weaker photocurrent) have also been observed for the BCTSn-0.1-0.1 ceramic (data not shown). It is worth to note that the optical band gap of BCTFe-0.1-0.025 has been estimated to be 2.78 eV. The energy of light with the wavelength of 650 nm is much lower than the optical band gap of BCTFe-0.1-0.025. Therefore, it is believed that the photovoltaic response could not be observed under the illumination of the light with wavelength > 650 nm. These imply that the photo-response of the ceramics are mainly resulted from the pyroelectric effect, and little from the photovoltaic effect. This may be due to the weak internal electric field which cannot separate the (small amount of) photo-generated charge carries effectively for producing a large observable current. Therefore, an external electric field (or bias field) is used to separate the charge carriers for investigating the optical band gap in the next section.

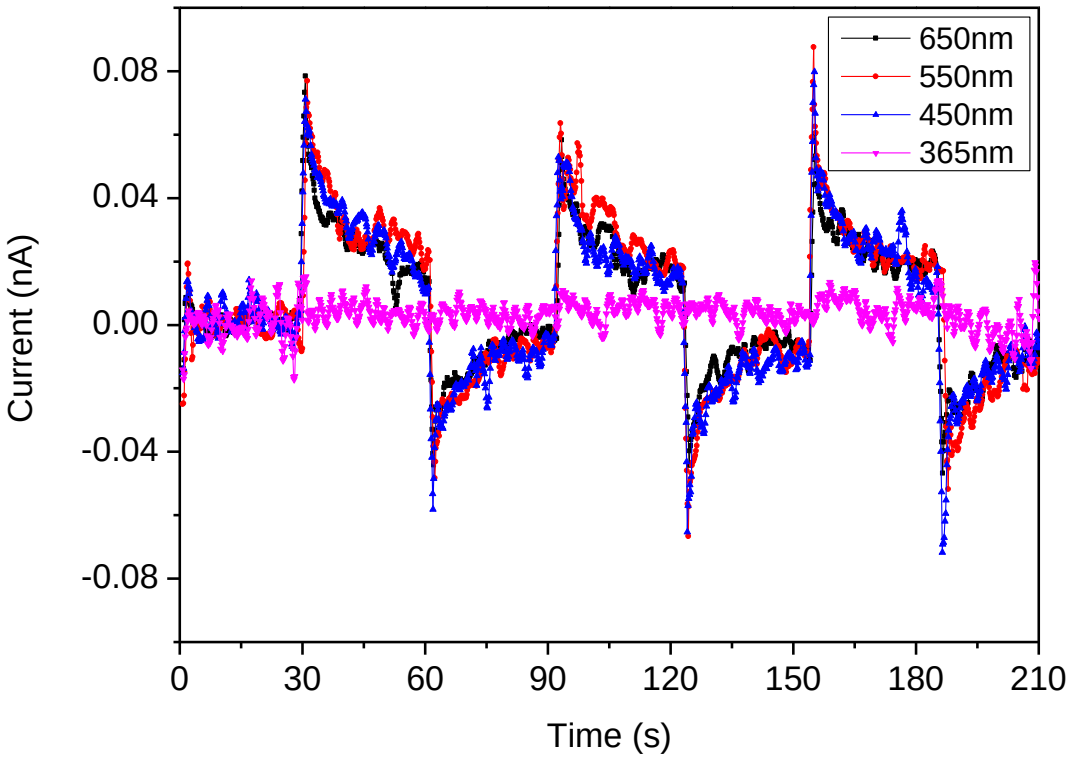

Figure 4-4 The wavelength dependent photovoltaic current of BCTFe-0.1-0.025 ceramics.

4.2.4. Wavelength-dependent photovoltaic current of un-poled ceramics

As discussed in Section 3.6.1, both the BCTSn-0.1-0.1 and BCTFe-0.1-0.025 ceramics show strong absorption in the ultra-violet (UV) region. A monochromatic light with a wavelength of 350 nm is thus chosen as a light source to determine the bias voltage for separating the photo-generated charge carries without distributing the polarization state of the ceramics. The un-poled ceramic samples are used to exclude the pyroelectric effect arisen from heating or cooling.

The current responses of the BCTSn-0.1-0.1 and BCTFe-0.1-0.025 ceramics under different bias voltages are shown at Figure 4-5. The current observed before the light is turned on is defined as the dark current. As shown in Figure 4-5, the BCTSn-0.1-0.1 and BCTFe-0.1-0.025 ceramics exhibit very similar dark currents under each bias voltage,

indicating that they have similar (dark) conductivity. To confirm this, the D.C. conductivity of the BCTSn-0.1-0.1 and BCTFe-0.1-0.025 ceramics (in the form of disk with a thickness of 0.5 mm and a diameter of 10 mm) have been measured to be 1.15×10^{-12} $\Omega^{-1}cm^{-1}$ and 1.5×10^{-12} $\Omega^{-1}cm^{-1}$, respectively, which are similar to those of other ferroelectric oxides [68].

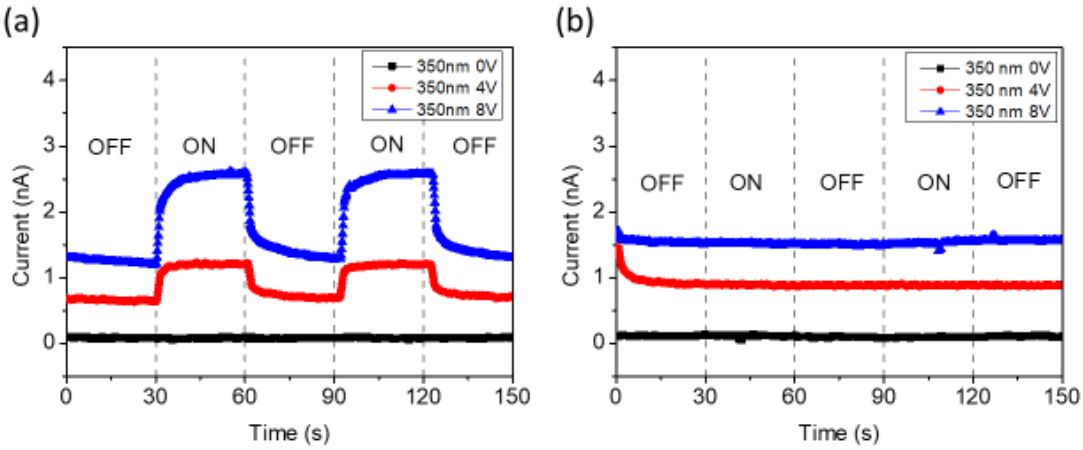

Figure 4-5 The bias voltage dependent photocurrent of (a) BCTSn-0.1-0.1 and (b) BCTFe-0.1-0.025.

When the light is turned on, the BCTSn-0.1-0.1 ceramic exhibits a large photocurrent of 1 nA under a bias voltage of 8V (or a bias field of 0.16 kV/mm). However, the BCTFe-0.1-0.0.025 ceramic shows almost no photocurrent as shown in Figure 4-5 (b). A higher bias voltage of 20 V has been applied, but the observed photocurrent of the ceramic is still very weak. It seems to suggest that the BCTFe-0.1-0.0.25 ceramic has a low photoconductivity. A low photoconductivity has also been observed in a $BiFeO_3$ (BFO) with an in-plane Au electrode having a gap of 25 μm [84]. In addition, the dark current of the BCTFe-0.1-0.025 ceramic becomes noisy when the bias voltage increases to 30 V. This equivalent to an electric field of 0.6 kV/mm, which is larger than the coercive field (0.25 kV/mm) of the ceramic and thus polarizing the ceramic (to a certain extent). The photocurrent induced by the external electric field may be canceled out by that

induced by the ferroelectric photovoltaic effect as well as the pyroelectric current. On the other hand, as discussed in Section 3.3.2, oxygen vacancies should form in the BCTFe-0.1-0.025 ceramic due to the trivalent dopant Fe. Under the bias voltage, the oxygen vacancies may migrate and accumulate at one side of the electrodes, following the field direction [114]. Thus, the migrated oxygen vacancies may play a role as extra positive carriers and form a diffusion gradient between two sides of the electrode. The carriers may diffuse from the high-density to low-density regions, which is called the diffusion current [115]. The weak photocurrent of the BCTFe-0.1-0.025 ceramic may be a combined result of the drift current induced by the bias voltage, the diffusion current and the polarization-induced photocurrent.

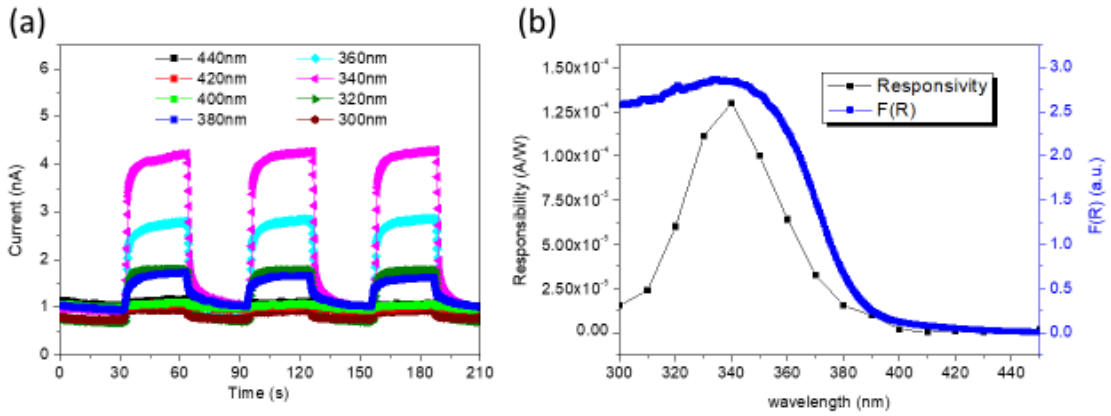

Figure 4-6 (a) The light wavelength dependent of photocurrent of BCTSn-0.1-0.1 at 8V bias voltage; (b) A responsivity spectrum of BCTSn-0.1-0.1 correlated with F(R).

For distinguishing the photovoltaic response of BCTSn-0.1-0.1 at each wavelength, the bias voltage should be large enough. Comparing with the photovoltaic response of BCTSn-0.1-0.1 under the bias voltage of 4 V and 8 V shown in Figure 4-5 (a), the bias voltage of 8 V seems more suitable used in wavelength dependence photovoltaic measurement. In fact, the bias voltage of 8V (or 0.16 kV/mm) is large enough to partially

polarize the BCTSn-0.1-0.1 ceramic due to its relatively small coercive field (0.11 kV/mm). The current induced by the partially aligned polarization of BCTSn-0.1-0.1 is negligible comparing that of induced by bias voltage (e.g. 0.04 nA vs 4 nA at the wavelength of 340 nm). Therefore, the bias voltage of 8V rather than 4 V is chosen for the wavelength-dependent photovoltaic current measurements. The photocurrent of the BCTSn-0.1-0.1 ceramic is measured from the wavelength of 450 nm to 300 nm with an interval of 10 nm. To simplify the view, Figure 4-6 (a) only shows the plots from the wavelength of 440 nm to 300 nm with an interval of 20 nm. The photocurrent is defined as the difference between the current in the ON and OFF states. The photocurrent in each cycle does not show significant variation, implying that the photocurrent is stable and repeatable. To evaluate the response of the photovoltaic response to the light intensity, the responsivity R of BCTSn-0.1-0.1 is calculated as $R = I/(PS)$, where P is the incident light intensity and S is the effect irradiated area defined in Section 2.1.2. After normalizing the photocurrent with the light intensity at each wavelength, the photo responsivity is plotted as a function of wavelength, together with the K-M Function F(R), as shown in Figure 4-6 (b). The photovoltaic response of BCTSn-0.1-0.1 is unobservable when the wavelength of incident light is larger than 400 nm. The responsivity of BCTSn-0.1-0.1, which matches well with that of F(R), is in agreement with the estimated lowest optical band gap of the BCTSn-0.1-0.1 ceramic (i.e., 3.26 eV or 381 nm). The responsivity starts to increase significantly when the wavelength becomes shorter than 380 nm and reaches a maximum at 340 nm. This may be attributed to the efficiency of electron-hole pairs generation at each wavelength. Similar observations of the maximum (i.e., 340 nm) have been reported for other ferroelectric materials as a result of the fast

band to band excitation [112, 116, 117]. After the maximum, the photo responsivity decreases owing to the rapid electron-hole pairs recombination [118].

4.3. Vertical electrode

As discussed in Section 4.2.2., the photocurrents of the BCTSn-0.1-0.1 and BCTFe-0.1-0.025 ceramics with IDE patterns are too weak for comparing their photovoltaic responses. Therefore, the vertical electrode configuration with a large electrode area has been used for examining the ferroelectric photovoltaic response. The schematic diagram of the vertical electrode configuration is shown in Figure 4-7. The transparent ITO top and bottom electrodes allow the ceramics to be illuminated by the light efficiently. The use of ITO as the top and bottom electrodes can exclude the effects arisen from Schottky barriers formed at the interfaces. As shown in Figure 4-7 (a), the so-called negative poling is achieved by the application of a negative electric field (i.e., applying a positive voltage to the top electrode of the ceramic. The (short-circuit) photocurrent resulted from the ferroelectric photovoltaic effect is opposite to the poling field, i.e., flowing out from the top electrode of the sample (Fig. 4-7b), which is defined as negative in this work.

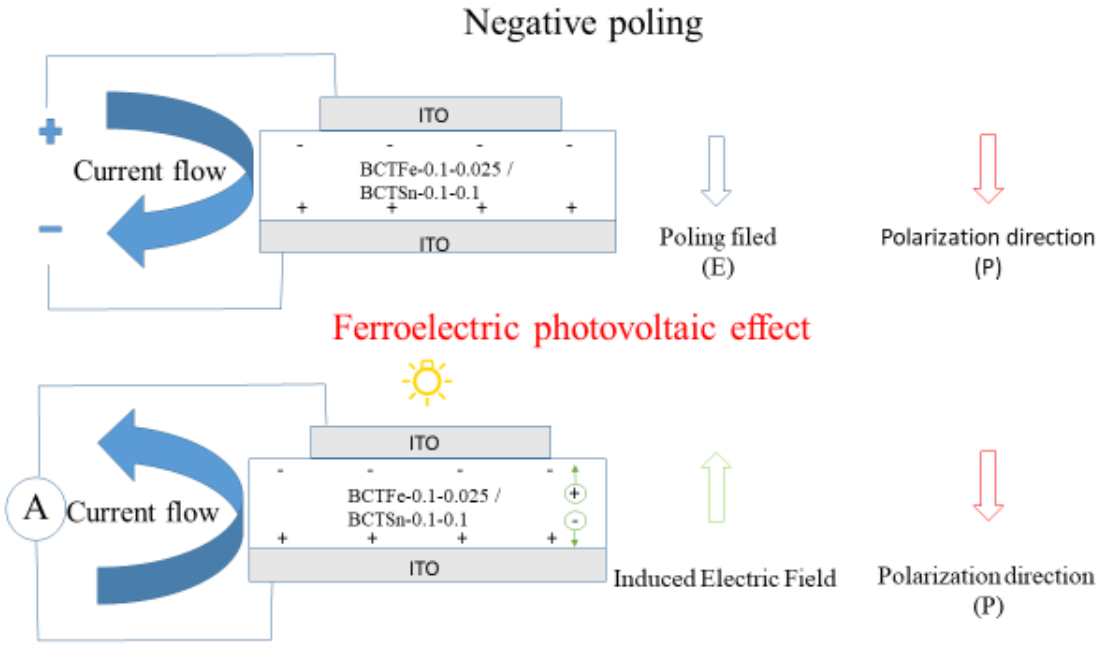

Figure 4-7 The schematic diagram of the current direction for (a) a negative poling process and (b) ferroelectric photovoltaic effect.

4.3.1. Ferroelectric Photovoltaic response under 1 sun illumination

Similar to the observations for the ceramics with IDE patterns, both the un-poled BCTSn-0.1-0.1 and BCTFe-0.1-0.025 ceramics (with vertical electrodes) exhibit insignificant photo-response under a zero bias (top panel in Figure 4-8(a) and (b)). Indeed, a small current is observed at the beginning of the ON and OFF states, which decays rapidly to a very small value (~0.1 nA) in 30 s. In addition, the current peak becomes smaller in the consecutive illumination cycles. Based on the repeated measurements (e.g., with new as-fabricated samples, annealed samples, different electrical connections), it is suggested that the current should not be arisen from the pyroelectric effect of samples.

Similar results have also been observed for un-poled ITO/$PbTiO_3$-$BiFeO_3$-$Bi(Ni_{1/2}Ti_{1/2}-)O_3$/Ag system [74]. On the other hand, our results have confirmed that the Schottky barriers formed at the interfaces do not have any significant effect on the photo-response.

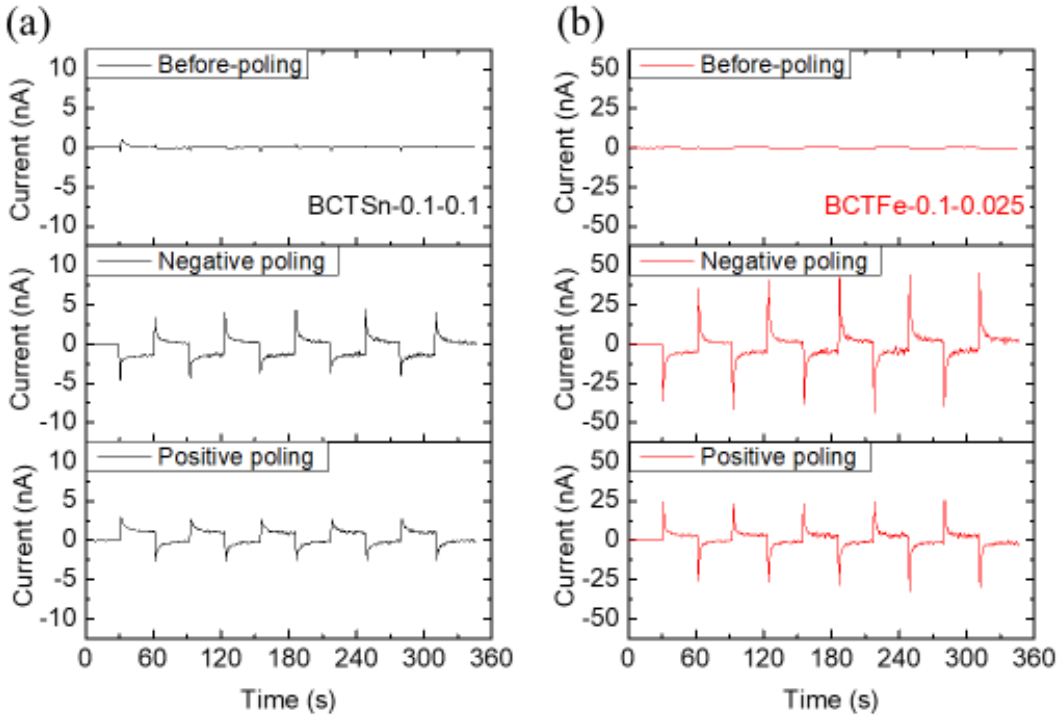

Figure 4-8 Ferroelectric photovoltaic response of (a) BCTSn-0.1-0.1 and (b)BCTFe-0.1-0.025 under 1 sun. Top: photocurrent for light on/off cycles after negatively poling; middle: un-poled state; bottom: after positive poling.

The ceramics (with a thickness of 100 μm) have then been poled under 100 V (or 1 kV/mm) for 30 min at room temperature in the negative direction and then in the positive direction. As shown in Figure 4-8, all the poled samples exhibit reproducible photo-responses, i.e., the observed photocurrent (for each poled ceramic) does not change, both the pattern and magnitude, significantly in the consecutive illumination cycles. Moreover, the photocurrent is governed by the poling direction, i.e., a negative (positive) poling

produces a negative (positive) photocurrent. This clearly confirms that the separation of the photo-generated charge carriers is realized by the aligned polarization, which is the major characteristics of the ferroelectric photovoltaic effect. For the negatively poled samples, the BCTFe-0.1-0.025 ceramic exhibits a photocurrent with larger peak (-42 nA vs -4.7 nA) and steady (-5.5 nA vs -1.5 nA) values as compared to the BCTSn-0.1-0.1 ceramic. The steady value of the current is the value evaluated from 5 s to 20 s during the ON state. After taking the electrode area into consideration, the steady current density of the BCTFe-0.1-0.025 ceramic is 11 nA/cm^2, which is comparable to those of lead-based ferroelectric oxides, e.g., $(Pb_{0.97}La_{0.03})(Zr_{0.52}Ti_{0.48})O_3$ and $PbTiO_3$-$BiFeO_3$-$Bi(Ni_{1/2}Ti_{1/2-})O_3$ [60,74]. Apart from the direction, the positively poled ceramics exhibit similar photocurrents to those poled in a negative direction, i.e., the positively poled BCTFe-0.1-0.025 ceramic exhibit a photocurrent with larger peak (38 nA) and steady (4.3 nA) values as compared to the positively poled BCTSn-0.1-0.1 ceramic (3.2 nA and 1.5nA, respectively).

As discussed in previous sections, the current peak (regardless of the direction) may be mainly contributed by the pyroelectric effect. The room-temperature pyroelectric coefficient of BCTSn-0.1-0.1 and BCTFe-0.1-0.025 have been measured to be 2.3x10^{-4} C/m^2·K and 4.8x10^{-4} C/m^2·K, respectively, which are comparable to the values found elsewhere [119, 120]. The pyroelectric current i can be calculated by [121]:

$$i = Ap\frac{dT}{dt} \qquad (4.1)$$

where A is the effective area of the samples, p is the pyroelectric coefficient, and $\frac{dT}{dt}$ is the rate of change of the temperature. In this work, the electrode area is 5.03x10^{-5} m^2 and the heating rate at the beginning of the ON state is 0.15˚C/s (Fig. 4-3c). The (maximum)

pyroelectric current of the BCTSn-0.1-0.1 and BCTFe-0.025 ceramics has then been estimated to be 1.7 nA and 3.6 nA, respectively. They are less than those peak values observed for both ceramics, suggesting that the pyroelectric effect may not play a dominant role in the observed current peak.

In ferroelectric materials, a significant change in photocurrent with time (i.e., the current peak) is frequently attributed to the pyroelectric effect arisen from the heating upon illumination as discussed in Section 4.2.1. [74,105]. However, it is difficult to estimate the pyroelectric current in the samples with IDE because of the complicated distributions of the electric field and polarization orientation. Similar current peaks have also been observed in (Pb, La)ZrO_3 ceramics with different bottom electrodes [60]. Although the authors attribute the current peak to the pyroelectric effect, it is not reasonable to obtain different current peak under same illumination condition just replacing the bottom electrode. Also, a change in the current direction has been observed for $PbTiO_3$-$BiFeO_3$-$Bi(Ni_{1/2}Ti_{1/2})O_3$ ceramics under illumination with light of different wavelengths, which should not be resulted from the pyroelectric effect [74, 106, 109]. The difference in the current peaks may be attributed to their different rates of charge recombination [57]. Therefore, it seems that the current peak observed in the samples with vertical electrode is mainly contributed by other factors (e.g. charge recombination) rather the pyroelectric effect [122]. On the other hand, the current peak has also been observed in non-ferroelectric ceramics (e.g., BCTFe-0.1-0.1) after applied electric field, which will be discussed in Chapter 5. This also suggests that the pyroelectric effect should not be the only factor producing the current peak.

4.3.2. Poling field dependent photocurrent

In order to examine the polarization-dependent photocurrent in detail, the ceramics (with vertical electrodes) have been poled progressively from -0.01 kV/mm to -1 kV/mm (i.e., Part I), and then from 0.01 kV/mm to 1 kV/mm (i.e., Part II), with an interval of 0.05 kV/mm. After each poling step, the ceramics have been stored in the dark and shorted circuit for 24 hours for removing any injected charges. The photocurrent is then measured under 1 sun illumination. Figure 4-9 shows the variations of the steady value of the photocurrent (i.e., the average value evaluated from 5 to 20 s after the illumination is switched on) with the poling field for both the BCTSn-0.1-0.1 and BCTFe-0.1-0.025 ceramics.

In Part I (i.e., poling the ceramics with a negative electric field), the magnitude of the (steady) photocurrent increases with increasing the magnitude of the electric field, and becomes saturated with the same value mentioned before (i.e., -1.5 nA and -5.5 nA for BCTSn-0.1-0.1 and BCTFe-0.1-0.025, respectively) at a poling field of -1 kV/mm. This clearly shows the significance of the (net) polarization in separating the photo-generated charge carries in producing photocurrent.

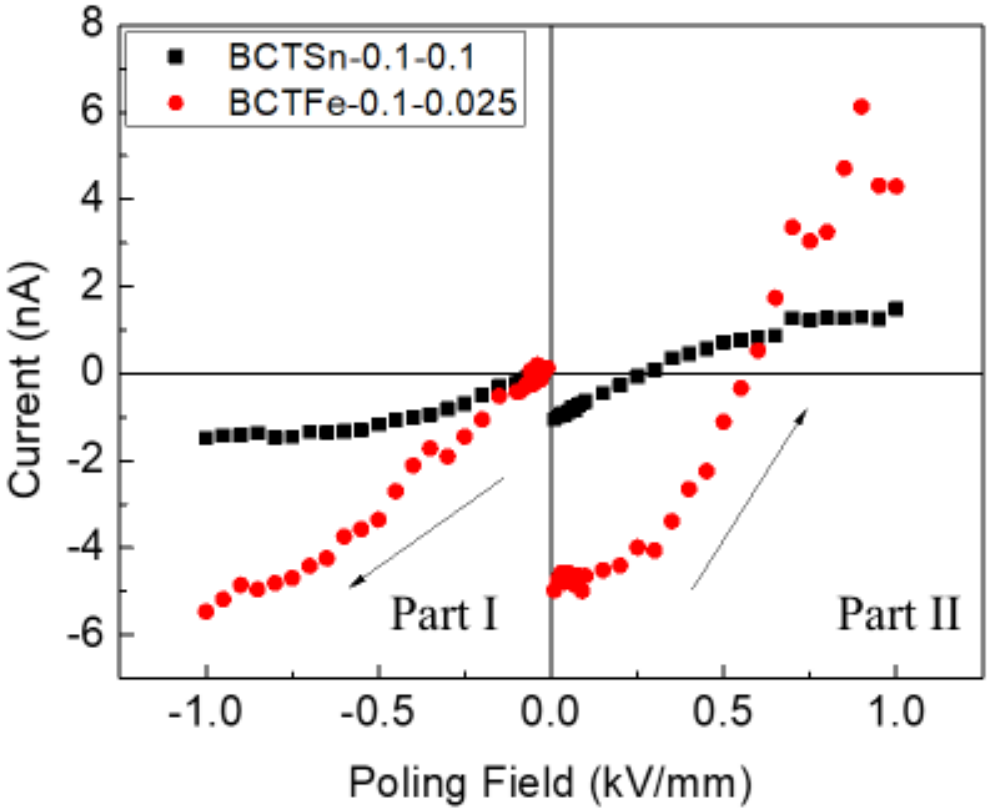

Figure 4-9 The photocurrent of BCTSn-0.1-0.1 and BCTFe-0.1-0.1 for different poling fields.

In Part II (i.e., applying a positive electric field, from 0.01 to 1 kV/mm, to the ceramic that has been just poled by an electric field of -1 kV/mm), the observed photocurrent for both ceramics decreases only slightly after the application of a small field (e.g. 0.05 kV/mm). As the electric field increases, the observed photocurrent decreases rapidly and reaches a zero value at 0.29 kV/mm and 0.59 kV/mm for the BCTSn-0.1-0.1 and BCTFe-0.1-0.025 ceramics, respectively. It is interesting to note that these values are about two times larger than the coercive field (0.11 kV/mm and 0.25 kV/mm, respectively) measured from the P-E loops of the ceramics. This may be due to the different measurement conditions. For the photocurrent measurement, the ceramics are poled by a D.C. electric field and the photocurrent (or polarization) is evaluated after

the removal of the electric field. But for the P-E loop measurement, an A.C. electric field is used and the polarization is evaluated under the electric field. As also shown in Figure 4-9, the observed photocurrent for both ceramics increases continuously as the poling field increases to 1 kV/mm. For each ceramic, the magnitude of the photocurrent after poled by -1 kV/mm and 1 kV/mm are almost the same. These clearly demonstrate that the photocurrent of the BCTSn-0.1-0.1 and BCTFe-0.1-0.025 ceramics are switchable and strongly related to the magnitude and direction of the (net) polarization, which are commonly observed for ferroelectric photovoltaic devices [60, 74, 105].

4.4. Conclusions

The ferroelectric photovoltaic responses of the BCTSn-0.1-0.1 and BCTFe-0.1-0.025 ceramics has been investigated using the IDE and vertical electrode configurations.

For the ceramics with IDE pattern, the observed photocurrent of the BCTFe-0.1-0.025 ceramic under 1 sun illumination is larger than that of the BCTSn-0.1-0.1 ceramic (0.22 nA vs 0.07 nA). The photocurrent is mainly contributed by the pyroelectric effect and the photovoltaic effect. The photocurrent observed in the beginning of the illumination is predominated by the pyroelectric effect while the steady photocurrent is mainly contributed by the photovoltaic effect. For both the (poled) ceramics, the observed photocurrent is weak and mainly contributed by the pyroelectric effect. The photocurrent of the unpoled ceramics has been measured for eliminating the pyroelectric effect. Under a bias voltage of 8 V, the photocurrent of the BCTSn-0.1-0.1 ceramic exhibit a strong dependence on the wavelength of the illumination. Based on the results, the optical band gap has been determined to be 3.26 eV, which is similar to the value determined from the

optical measurement. On the other hand, the photocurrent of the unpoled BCTFe-0.1-0.025 ceramic under the same bias voltage is very weak.

Probably because of the larger illuminated region, the photocurrent of the (poled) ceramics with vertical electrodes are larger. Both the BCTSn-0.1-0.1 and BCTFe-0.1-0.025 ceramics exhibit a photocurrent peak in the beginning of the illumination (3.6 nA and 42 nA, respectively) followed by a steady photocurrent (1.5 nA and 5.5 nA, or 3 nA/cm^2 and 11 nA/cm^2, respectively). As the estimated photocurrent arisen from the pyroelectric effect (1.7 nA and 3.6 nA, respectively) is smaller than the current peak, it is suggested that there may be other effects contributing to the photocurrent, particularly in the beginning of the illumination. Further experiments are needed to investigate the mechanism of the observed current peaks.

In conclude, the BCTFe-0.1-0.025 exhibited stronger ferroelectric photovoltaic response on both in-plane and vertical electrode configuration. By ruling out the contribution of the pyroelectric effect and conductivity of two ceramics (i.e. BCTSn-0.1-0.1 and BCTFe-0.1-0.025), it suggests that the improved photocurrent of BCTFe-0.1-0.025 is attributed to the broadening absorption of the visible spectrum (or lower optical band gap) of BCTFe-0.1-0.025.

Chapter 5 Photovoltaic effect on BCTFe-0.1-0.1 non-ferroelectric ceramics

5.1. Introduction

In Chapter 3, it has been shown that the optical band gap of the BCTFe-0.1-x ceramics decreases with increasing the doping level of Fe^{3+} (i.e., 2.78 eV). The ferroelectric photovoltaic response of the BCTFe-0.1-0.025 ceramic has been studied in Chapter 4. However, probably because of the insufficient input light intensity or low photoconductivity, the wavelength-dependent photocurrent of the ceramic is weak and then the optical band gap of the ceramic could not be confirmed based on the measurements.

In this chapter, the optical band gap of the BCTFe-0.1-0.1 ceramic is studied with the aim of providing additional evidence of the optical band gap reduction. The photocurrent of the ceramic under zero bias voltage will be investigated. Unlike BCTFe-0.1-0.025, the BCTFe-0.1-0.1 ceramic is non-ferroelectric and does not contain (significant) spontaneous polarization, and then there should not additional effect such as pyroelectric current. The current and voltage of the ceramic with asymmetric vertical electrode configuration (i.e., ITO/BCTFe-0.1-0.1/Cr/Au) under different bias voltages will be also examined, and then its conductivity will be estimated. In addition, the wavelength-dependent photocurrent of the ceramic will also be measured for confirming the reduction in the bang gap.

Besides, the influence of oxygen vacancies on the photovoltaic response of the ceramic will be investigated. Symmetric vertical electrode configuration (i.e.

ITO/BCTFe-0.1-0.1/ITO) will be used for eliminating the effect arisen from the interfaces. The switchable photovoltaic response will also be demonstrated.

5.2. Asymmetric electrode (ITO-Cr/Au)

Similar to the vertical electrode configuration used in Chapter 4 (Figure 4.3), the ITO top electrode has a diameter of 8 mm. Theoretically, the Schottky barrier of ITO/BCTFe-0.1-0.1 is determined by the difference of work function between ITO and BCTFe-0.1-0.1. It has been reported that an asymmetric band structure arisen from different Schottky barriers formed at the ceramic/electrode interfaces between the top and bottom electrodes can induce photovoltaic response [81, 123]. Assuming the work functions of ITO, BCTFe-0.1-0.1 and Cr are ~4.5 eV and~3.9 eV and ~4.6 eV, respectively [104, 107, 124]. the net built-in field, which may be defined as the difference between the built-in field of top and bottom Schottky barriers, should induce photovoltaic response in the BCTFe-0.1-0.1 ceramic [82]. Therefore, with the aim of constructing the Schottky barriers, Cr/Au bottom electrodes are used. The deposition parameters for the Cr/Au bottom electrode are same as those for the IDE pattern mentioned in Section 2.1.3. The short-circuit current of the as-fabricated BCTFe-0.1-0.1 ceramic is measured under 1 sun illumination.

5.2.1. Photovoltaic performance under 1 sun

The short-circuit current (under zero bias voltage) and open- circuit voltage (under zero current flow) of the BCTFe-0.1-0.1 ceramic under 1 sun illumination are shown in Figure 5-1 (a) and (b), respectively. For the open-circuit voltage, the voltage of the sample is measured under zero-current condition. It could be considered as the voltage that must be applied to the sample to stop the current. Therefore, the so-called open circuit voltage

is opposite to the sign of short circuit current. For confirming the contribution of the photovoltaic response, the ceramic has been connected to the Keithley 2410 source meter in both positive (i.e., connecting the ITO electrode to the positive port of the source meter) and negative directions. Except for the sign, the observed current and voltage for both connections are almost the same, giving a value of 5.5 nA (or 10.9 nA/cm^2 in current density) and 0.16 V, respectively. These suggest that they are mainly contributed by the photovoltaic response of the BCTFe-0.1-0.1 ceramic. The short-circuit current and open-circuit voltage are the average values evaluated from 5 s to 20 s during the ON state. As also shown in Figure 5-1 (a), no current peak is observed, indicating the insignificant contribution of the pyroelectric effect or other factors observed for the BCTFe-0.1-0.025 ceramic. On the other hand, the short-circuit current increases gradually in the consecutive ON states, while the open-circuit voltage decreases gradually. This should be attributed to the increase in conductivity resulted from the illumination and then heating, which will be discussed in the following section.

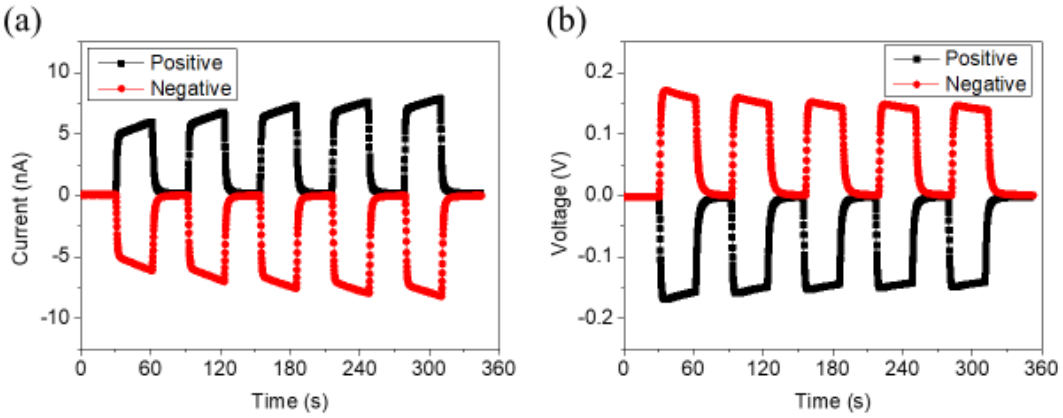

Figure 5-1 The (a) short-circuit current and (b) open circuit voltage of BCTFe-0.1-0.1 as function of time measured at forward/reverse connection.

5.2.2. I-V characteristic

The photocurrent of the BCTFe-0.1-0.1 ceramic has been measured at different bias voltages under 1 sun illumination, giving the results shown in Figure 5-2. The bias voltage, ranging from 0 to 0.24 V with an interval of 0.04 V, is applied to the bottom electrode of the ceramic. For demonstration purposes, only part of the results is shown in Figure 5-2 (a). The average current evaluated from 5 s to 20 s during each ON and OFF states are plotted as a function of bias voltage in Figure 5-2 (b). It can be seen that the observed photocurrent is negative as the bias voltage is below 0.16 V, while it becomes positive as the bias voltage is above 0.16 V (Figure 5-2b). This indicates that there is a net electric field which changes the direction as the bias voltage increases. As demonstrated in Figure 5-1 (b), the observed open-circuit voltage, which pointing towards the bottom electrode, is ~0.16 V. When the bias voltage pointing towards the top electrode is lower than 0.16 V, the sign of net electric field has not changed the direction, and thus the photocurrent flows out from the bottom electrode (which is defined as negative). As the bias voltage increases, the net electric field and then the photocurrent change the direction. As shown in Figure 5-2(b), the bias voltage for reversing the photocurrent is about 0.16 V, which is in agreement with the observed open-circuit voltage shown in Figure 5-1.

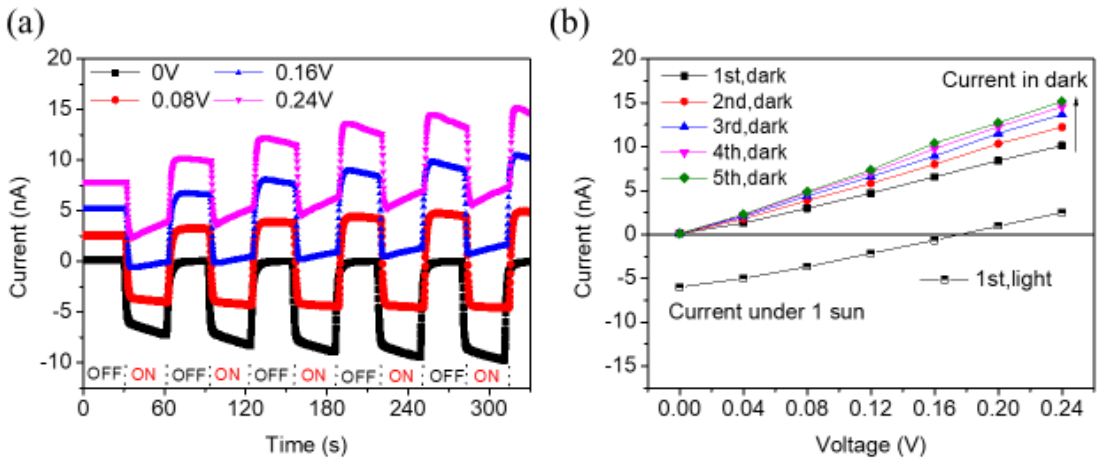

Figure 5-2 (a) Time-dependent short-circuit current of BCTFe-0.1-0.1 on reverse connection with different bias voltage; (b) The I-V curves of BCTFe-0.1-0.1 measured in dark and under illumination.

Based on the initial dark current (i.e., the current in the first OFF state) under each bias voltage (Fig. 5-2a), the resistance of the BCTFe-0.1-0.1 ceramic is calculated as 23 MΩ. It can also be seen that the observed dark current decreases gradually in the consecutive cycles, which should be resulted from a decrease of the resistance. As discussed in Section 4.2.1, the sample will be heated up by the illumination. As the temperature increases, the conductivity increases, and thus resulting in a lower resistance. This phenomenon has always been observed in oxygen vacancies-rich ferroelectric ceramics [115, 116]. Because of the increased conductivity (or decreased resistance), the observed photocurrent also increases gradually in the consecutive illumination cycles.

5.2.3. Wavelength dependence photovoltaic effect

For determining the optical band gap, the short-circuit photocurrent of the BCTFe-0.1-0.1 ceramic under illumination of different wavelengths, ranging from 800 nm to 300

nm, has been measured, giving the results shown in Figure 5-3 (a). To simplify the view, only the photocurrents under UV illumination (i.e., 450 nm to 300 nm) are shown. At each wavelength, the observed photocurrent remains almost unchanged in each ON state, implying an insignificant change in the conductivity. It is probably because of the relatively weak intensity of each monochromatic light (~4 mW/cm^2). After normalizing the photocurrent with the light intensity at each wavelength, the photo responsivity is plotted as a function of wavelength as shown in Figure 5-3(b). The K-M function F(R), which is related to the optical absorption as discussed in Section 2.2.5, is also plotted for comparison purposes. In Region 1 (i.e., 300 nm to 390 nm), the photo responsivity is large, which should be partly attributed to the strong absorption as evidenced by the large F(R). In this region, the F(R) is increasing while responsivity is decreasing. It may attribute to the difference between the generation and recombination rate of electron-hole pairs [118]. In agreement with the decreasing F(R), the photo responsivity decreases rapidly, by almost two orders of magnitude, in Region 2 (390 nm to 580 nm), and becomes almost unobservable is Region 3 (590 nm or above). The difference between the observable and unobservable photocurrent is shown in the inset of Figure 5-3 (b). Based on the agreement between the responsivity and F(R), the results confirm that the Fe^{3+} dopants can extend the optical absorption of BCT ceramics from the U-V region (i.e., below 400 nm) to the green light (i.e., 580 nm). Therefore, the optical band gap of the BCTFe-0.1-0.1 ceramic should be estimated to be 2.24 eV, which is lowest value estimated based on the reflectance results shown in Table 3-4.

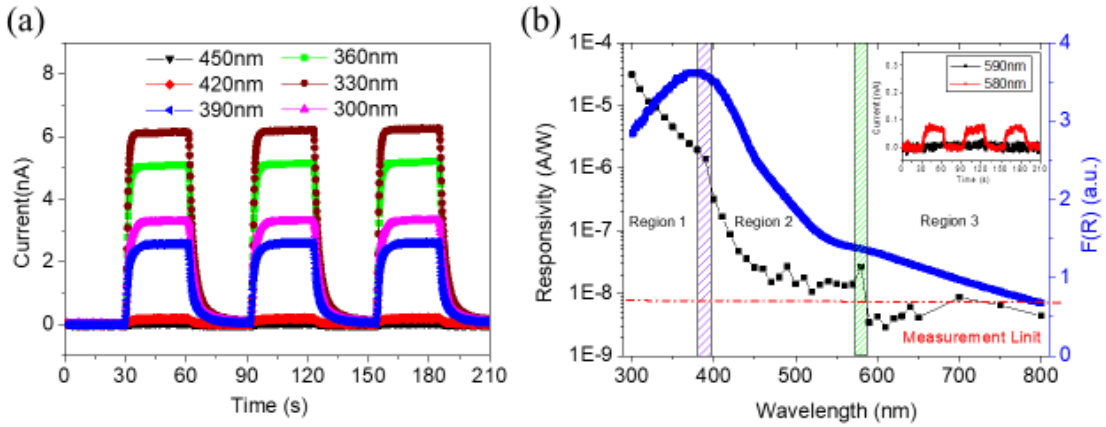

Figure 5-3 (a) The wavelength-dependent photocurrent of BCTFe-0.1-0.1 on U-V region; (b) The plot of photocurrent and F(R) of BCTFe-0.1-0.1 as function of wavelength, the inset is the time-dependent photocurrent under 590 nm and 580 nm illumination.

5.3. Symmetric electrode (ITO – ITO)

A BCTFe-0.1-0.1 ceramic with symmetric vertical electrodes (i.e., ITO-ITO) has been prepared for further investigating the photo-response of the non-ferroelectric ceramic. Figure 5-4 shows the observed photocurrent of the ceramics with symmetric electrodes and asymmetric electrodes (ITO-Au) under1 sun illumination. It is interesting to note that a significant photocurrent is observed for the ceramic with symmetric electrodes, implying that there should be factors other than Schottky barrier to generate the photocurrent in the non-ferroelectric ceramic. Similar to the ceramics with asymmetric electrodes, the observed current is changed the direction when the connection is reversed confirming that the observed current is contributed by photovoltaic response.

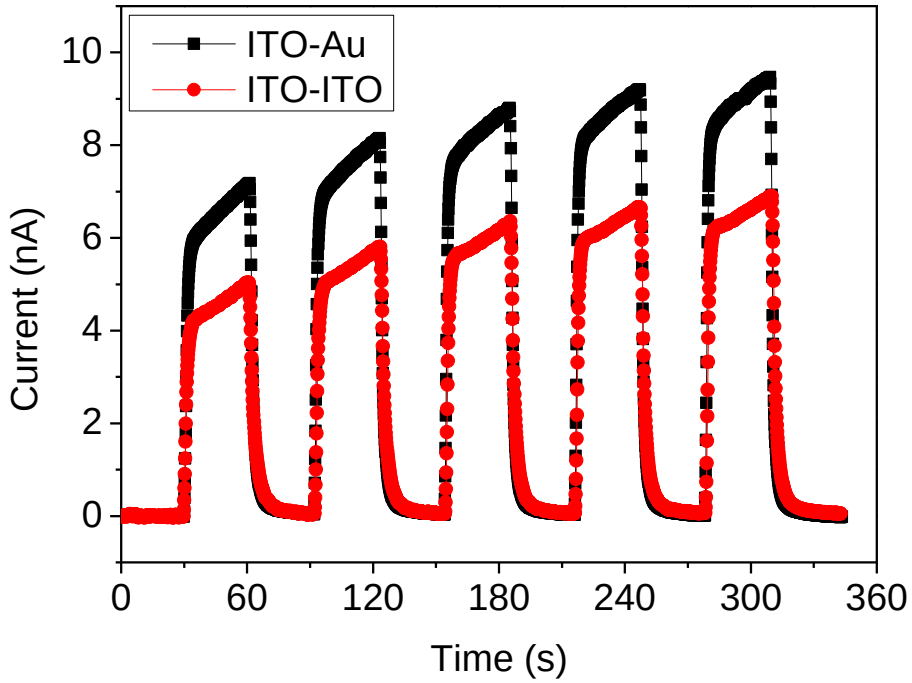

Figure 5-4 Time-dependent photocurrent of BCTFe-0.1-0.1 in ITO/ceramic/ITO and ITO/ceramic/Au configuration.

The ferroelectric photovoltaic effect should not be the originate of the photocurrent. As discussed in Chapter 3, the BCTFe-0.1-0.1 ceramic is non-ferroelectric at room temperature and thus no spontaneous polarization can be aligned for inducing the photovoltaic response. The built-in field induced by the Schottky barrier at the ITO/BCTFe-0.1-0.1 interfaces should be canceled out due to the symmetric electrode configuration. Ji *et al* have suggested that the built-in field induced in BFO is resulted from a non-uniform distribution of oxygen vacancies [68]. The accumulation of oxygen vacancies at one side induces different energy band bending behavior at the two interfaces although the top and bottom electrodes are the same. In addition, a high concentration of oxygen vacancy at the interface can reduce the barrier height [125]. Therefore, it believed that a net built-in field could be formed due to an un-uniform oxygen vacancy distribution although the extra experiments are needed to confirm the formation of net built-in field.

Under the illumination, the built-in field drives the separation of the electron-holes pairs and results in a "drift current". On the other hand, oxygen vacancies can trap the photo-induced electrons and the photo-induced holes become the extra charge carriers [81, 126]. Thus, a diffusion gradient is formed inside the sample under illumination. The extra charge carriers diffuse from high concentration to low concentration and induce a diffusion current. As discussed in Section 3.6, oxygen vacancies exist in the BCTFe-0.1-x ceramics. For easy description, the "top" electrode is defined as electrode deposited on the top of ceramic with 8 mm diameter and the "bottom" electrode is defined as deposited on the bottom of ceramic with 10 mm diameter, although the "top" and "bottom" electrode are of the same material (i.e., ITO). On the other hand, there are not experiment evidence shown that the photovoltaic response of ferroelectric ceramics will be affected by the difference between the size of top and bottom [55, 74]. Therefore, in our study, it assumed that the photovoltaic response would not be affected by the size difference between the top and bottom electrode. The observed photocurrent in the as-fabricated BCTFe-0.1-0.1 ceramic with symmetric electrodes should be attributed to the oxygen vacancies, which accumulate at the top ITO electrode and induce a current flowing from the top electrode to the bottom electrode. Although further experiments are needed for investigating the accumulation mechanism, the suggestion of the accumulation of oxygen vacancies at the top electrode is based on the experimental observed and will be evaluated by additional experimental results (discussed below). A schematic diagram showing the flow of the photocurrent in the ceramic at different states under illumination is shown in Figure 5-5. For the as-fabricated ceramic as shown in Figure 5-5 (a), the oxygen vacancies accumulated at the top electrode. Under illumination, a net (short-circuit) photocurrent combining the drift current and diffusion current is formed and flows from the top to the

bottom electrode. Here, we hypothesis that the point defect, such as oxygen vacancies, possibly exist and act as mobile ions with positive charges although the density of ions (defects) may need further estimations. They can move through the samples under electric filed to achieve a new thermodynamic equilibrium [128,129]. If a positive electric field is applied, the oxygen vacancies (mobile ions) will migrate and accumulate at the bottom electrode as shown in Figure 5-5(b). After the removal of the electric field, the net (short-circuit) photocurrent will then flow from the bottom electrode to the top electrode under illumination.

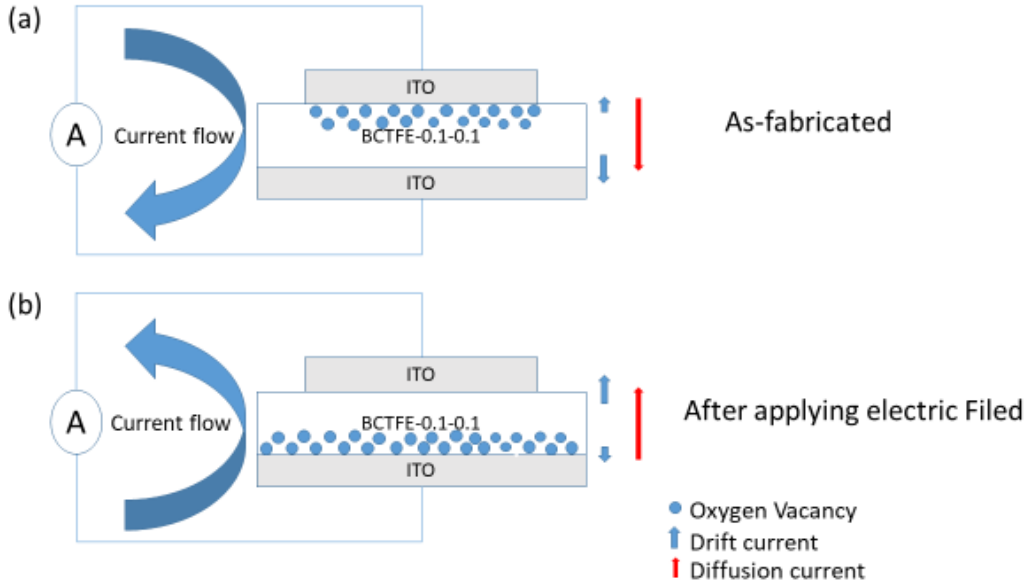

Figure 5-5 Schematic diagrams of short-circuit current flow at different state: (a) oxygen vacancies accumulated at top electrode as-fabricated BCTFe-0.1-0.1; (b) oxygen vacancies accumulated at bottom electrode after applied external E-field.

5.3.1. Switchable photovoltaic response on non-ferroelectric BCTFe-0.1-0.1 ceramic

It is worth to note that the poling condition (1 kV/mm, room temperature) for triggering the ferroelectric photovoltaic response of BCTFe-0.1-0.025 and BCTSn-0.1-0.1 had been also applied to the non-ferroelectric ceramic BCTFe-0.1-0.1. The observed photocurrent is consistent before and after applying 1 kV/mm at room temperature. It implies that oxygen vacancies (mobile ions) may not been redistributed under the poling condition (i.e., 1 kV/mm for 30 min, room temperature). Therefore, it is believed that the distribution of the oxygen vacancies (mobile ions) in the ferroelectric materials (BCTFe-0.1-0.025 and BCTSn-0.1-0.1) will not change after poling. As a result, the switchable photocurrent observed in ferroelectric devices should mainly raise from the (net) polarization rather than the re-distribution of the oxygen vacancies (mobile ions). For confirming the suggestion discussed above, an external electric field of 1 kV/mm (which is the same as the poling field for the ferroelectric BCTFe-0.1-0.025 ceramic) has been applied to the (non-ferroelectric) BCTFe-0.1-0.1 ceramic at 100°C for 30 min or 60 min, and its short circuit photocurrent of BCTFe-0.1-0.1 under 1 sun illumination has been measured, giving the results shown in Figure 5-6. Chen *et al.* have reported that the photovoltaic performance of BFO films can be improved by the application of an external electric field (smaller than the coercive field) at high temperatures (e.g. 100°C) [82]. It is suggested that the high temperature favors the migration and then the accumulation of oxygen vacancies (mobile ions). Therefore, the external electric field is applied to the

BCTFe-0.1-0.1 ceramic at 100°C for accelerating the migration of the oxygen vacancies (mobile ions).

As shown in Figure 5-6(a), the observed photocurrent of the as-fabricated ceramic increases with time because of the heating arisen from the illumination. The current is flowing out from the top electrode and is defined as positive. After the application of the electric field (pointing from the top electrode to bottom electrode) for 30 min, the photocurrent exhibits a small positive peak at the beginning of the On state, becomes negative. Similarly, the magnitude of the photocurrent increases gradually with time because of the heating. Apparently, the migration and accumulation of oxygen vacancies (mobile ions) can be enhanced by extending the application time of the electric field. As a result, the observed photocurrent (magnitude) of the ceramic after applying the field for 60 min increases considerably. Then the ceramic has been annealed at 100°C for 360 min with the aim of restoring the oxygen vacancies (mobile ions) to the "original" distribution.

As shown in Figure 5-6(d), the observed photocurrent becomes positive, i.e., returning to the original flow direction, but the magnitude cannot be entirely restored. This indicates that the re-distribution is not completed, which may be due to the low migration rate contributed mainly by thermal energy. To enhance the migration, an electric field of -1 kV/mm (i.e., pointing from the bottom electrode to the top electrode) has been applied to the ceramic at 100°C for 60 min. As shown in Figurer 5-6(e), the observed photocurrent becomes larger than that of the as-fabricated ceramic. These demonstrate that the observed photocurrent in the non-ferroelectric BCTFe-0.1-0.1 ceramic is driven by the non-uniform distribution of oxygen vacancies (mobile ions) which can be changed by an external electric field, in particular at high temperatures (e.g., 100°C).

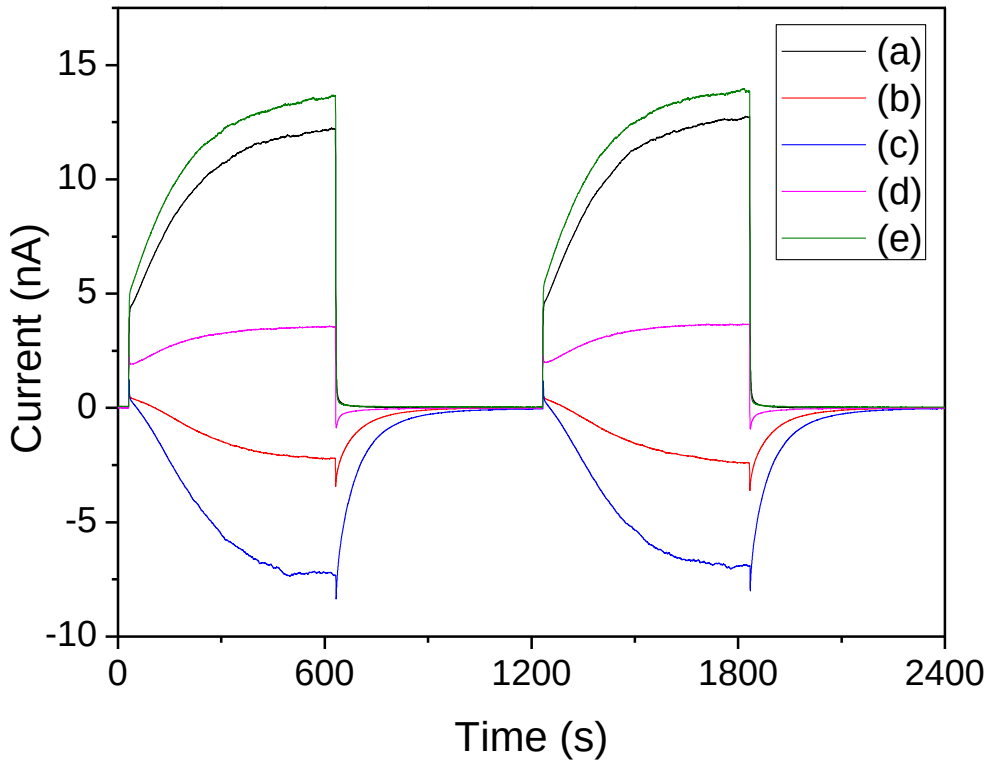

Figure 5-6 The short-circuit current of BCTFe-0.1-0.1 under 1 sun illumination for different state: (a) as-fabricated; (b) applied 100V (i.e., 1 kV/mm) for 30 min at 100°C; (c) applied 100 V (i.e., 1 kV/mm) for 60 min at 100 °C; (d) annealed for 360 min at 100°C; (e) applied -100 V (i.e., -1 kV/mm) for 60 min at 100 °C.

The results also demonstrate that the oxygen vacancies (mobile ions) accumulate originally at the top electrode of the as-fabricated ceramic. Nevertheless, as discussed above, the reasons for them to accumulate at the top electrode but not the bottom electrode of the same material is not known yet. In fact, there are also observations needed further investigation. For examples, the current peak observed at the beginning of the ON and OFF states for the ceramic after being subjected to an external field, and the different photocurrent behaviors observed in the OFF state for the ceramic at different states. They may be attributed to the change of the surface charge recombination rate and the

conversion of Schottky-Ohmic contact induced by the migration of the oxygen vacancies (mobile ions) [82,84,114].

5.4. Conclusions

The photovoltaic response of the BCTFe-0.1-0.1 ceramic has been investigated using vertical asymmetric and symmetric electrode configurations, i.e., ITO-BCTFe-0.1-0.1-Cr/Au and ITO-BCTFe-0.1-0.1-ITO, respectively.

The short-circuit photocurrent and open-circuit voltage of the ITO-BCTFe-0.1-0.1-Cr/Au ceramic under 1 sun illumination is 10.9 nA/cm^2 and 0.16 V, respectively. Upon illumination and then heating, the short-circuit photocurrent increases with time because of the increase in the conductivity, while the open-circuited voltage decreases slightly. Besides, the open-circuit voltage has been confirmed by the measurements at different bias voltages. It has been demonstrated that the photovoltaic response of BCTFe-0.1-0.1 and confirmed that the conductivity of ceramics is increased during illumination. Also, based on the measurements under illumination of different wavelengths, the optical band gap of the BCTFe-0.1-0.1 ceramic is determined to be 2.24 eV. It is the additional experimental evidence for supporting the optical band gap reduction of BCTFe-0.1-x series ceramic.

On the other hand, the photo-response of the ITO-BCTFe-0.1-0.1-ITO ceramic has been investigated. As the BCTFe-0.1-0.1 ceramic is non-ferroelectric, the observed photovoltaic response should be attributed to the accumulation of oxygen vacancies (mobile ions) inside the samples. Our results have shown that the distribution of oxygen vacancies (mobile ions) can be modulated by an external electric field at high temperatures (e.g., 1 kV/mm at 100°C), and thus the photocurrent is switchable. It

demonstrated that the switchable photocurrent can be also obtained on the non-ferroelectric ceramic. It may be the other path for designing the switchable photovoltaic devices by modulating the oxygen vacancies (mobile ions) inside the ceramic.

Chapter 6 Conclusions

This study demonstrates an improvement of the ferroelectric photovoltaic response by reducing the optical band gap of ferroelectric oxides. It shows a pathway for designing new ferroelectric oxides with a low optical band gap and high piezoelectricity for multifunction applications. Intriguingly, oxygen vacancies play a crucial role in the photovoltaic performance as evidenced by the observations in non-ferroelectric oxides with ITO symmetric electrodes. Switchable currents have been observed in both ferroelectric BCTFe-0.1-0.025 and non-ferroelectric BCTFe-0.1-0.1 ceramics.

BCTSn-0.1-0.1 and BCTFe-0.1-x ceramics with x= 0.025, 0.05 and 0.1 have been successfully fabricated by a solid-state reaction method. The pure perovskite structure of the ceramics has been confirmed by the XRD pattern. Together with the results of the dielectric, piezoelectric, and ferroelectric properties, a non-ferroelectric cubic to ferroelectric tetragonal phase transition has been confirmed in the BCTFe-0.1-x ceramics. The phase transition temperature increases with decreasing the doping level of Fe^{3+}. The observed Curie temperature is 53°C for the BCTFe-0.1-0.025 ceramic. Because of the ferroelectric tetragonal structure at room temperature, the BCTFe-0.1-0.025 ceramic exhibits a large d_{33} (190 pC/N) and P_r (4.5 μC/cm^2), which are comparable to those of the BCTSn-0.1-0.1 ceramic (300 pC/N and 6 μC/cm^2). Moreover, the absorption edge of the ceramics shows a redshift from 450 nm to 550 nm after replacing Sn^{4+} with Fe^{3+}. The optical band gap of the BCTFe-0.1-x ceramics decreases with increasing the doping level of Fe^{3+}. The BCTFe-0.1-0.025 ceramic thus exhibits optimized properties for ferroelectric photovoltaic response, i.e., a low optical band gap (2.78 eV) and good piezoelectric properties (190 pC/N).

The ferroelectric photovoltaic response of the BCTSn-0.1-0.1 and BCTFe-0.1-0.025 ceramics has been investigated using IDE pattern and vertical ITO electrode configuration. For the sample with IDE pattern, the photocurrent of BCTFe-0.1-0.025 is slightly larger than that of BCTSn-0.1-0.1(0.22 nA vs 0.07 nA). Based on the bias voltage-dependent photo-responses, the optical band gap of the BCTSn-0.1-0.1 ceramic has been confirmed as 3.26 eV. On the other hand, the steady photocurrent of the BCTFe-0.1-0.025 ceramic with vertical electrode configuration is 5.5 nA or 11 nA/cm^2, which is 3 times larger than that of the BCTSn-0.1-0.1 ceramic (1.5 nA or 3 nA/cm^2).

The photovoltaic properties of the non-ferroelectric BCTFe-0.1-0.1 ceramic have also been investigated using vertical asymmetric ITO-Cr/Au electrodes. The short-circuit current and open-circuit voltage of the ceramic, which has been directly measured using Keithley 2410 under 1 sun illumination, are 10.9 nA/cm^2 and 0.16 V, respectively. The I-V curves have been investigated, based on which the conductivity is found to increase during the illumination. Also, the wavelength-dependent photovoltaic response has confirmed the reduction of the optical band gap to 2.24 eV.

The BCTFe-0.1-0.025 ceramics with both the in-plane and vertical electrode configurations exhibit improved ferroelectric photovoltaic response. The conductivities of the BCTSn-0.1-0.1 and BCTFe-0.1-0.025 ceramics are similar, i.e., 1.15x10^{-12} Ω^{-1}cm^{-1} and 1.5x10^{-12} Ω^{-1}cm^{-1}, respectively. The pyroelectric effect is not the predominant effect for the observed photocurrent. It is then suggested that the enhanced ferroelectric photovoltaic response of the BCTFe-0.1-0.025 ceramic should be attributed to its broaden absorption (or lower optical band gap). It demonstrates that it is possible to improve the ferroelectric photovoltaic response by reducing the optical band gap and retaining the piezoelectricity at the same time.

On the other hand, the photovoltaic response has also been observed in the BCTFe-0.1-0.1 ceramic deposited with symmetric ITO electrode configuration. This should be attributed to the accumulation of oxygen vacancies (mobile ions) in one side of the ceramics. The distribution of oxygen vacancies (mobile ions) can be modulated by an external field and thus the photocurrent is switchable. Our results also show that the switchable photovoltaic response can be obtained in the non-ferroelectric ceramic, which confirms the effects of oxygen vacancies (mobile ions) on the photovoltaic response.

References

[1] Haertling, G. H. (1999). Ferroelectric ceramics: history and technology. Journal of the American Ceramic Society, 82(4), 797-818.

[2] Cohen, R. E. (1992). Origin of ferroelectricity in perovskite oxides. *Nature*, *358*(6382), 136.

[3] Kong, L. B., Huang, H., & Li, S. (2018). Fundamentals of Ferroelectric Materials. *Ferroelectric Materials for Energy Applications*, 1-31.

[4] Glass, A. M., Linde, D. V. D., & Negran, T. J. (1995). High-voltage bulk photovoltaic effect and the photorefractive process in LiNbO3. In *Landmark Papers On Photorefractive Nonlinear Optics* (pp. 371-373).

[5] Ahmed, A., Goldthorpe, I. A., & Khandani, A. K. (2015). Electrically tunable materials for microwave applications. *Applied Physics Reviews*, *2*(1), 011302.

[6] Zheng, T., Wu, J., Xiao, D., & Zhu, J. (2018). Recent development in lead-free perovskite piezoelectric bulk materials. *Progress in Materials Science*, *98*, 552-624.

[7] Safari, A., & Akdogan, E. K. (Eds.). (2008). *Piezoelectric and acoustic materials for transducer applications*. Springer Science & Business Media.

[8] Neurgaonkar, R. R., & Cory, W. K. (1986). Progress in photorefractive tungsten bronze crystals. *JOSA B*, *3*(2), 274-282.

[9] Lang, M., Zhang, F., Zhang, J., Wang, J., Lian, J., Weber, W. J., ... & Ewing, R. C. (2010). Review of A2B2O7 pyrochlore response to irradiation and pressure. *Nuclear Instruments and Methods in Physics Research Section B: Beam Interactions with Materials and Atoms*, *268*(19), 2951-2959.

[10] YAN, H. X., LI, C. E., ZHOU, J. G., & ZHU, W. M. (2000). Structures and Properties of Bismuth Layer-structured Piezoelectric Ceramics with High T_c [J]. *Journal of Inorganic Materials*, *2*.

[11] Damjanovic, D. (1998). Ferroelectric, dielectric and piezoelectric properties of ferroelectric thin films and ceramics. *Reports on Progress in Physics*, *61*(9), 1267.

[12] Miyake, S. (2005). *Novel Materials Processing by Advanced Electromagnetic Energy Sources: Proceedings of the International Symposium on Novel Materials Processing by Advanced Electromagnetic Energy Sources (MAPEES'04)*. Elsevier.

[13] Intravascular Ultrasound Image, (). piezoelectric effect [Drawing], Retrieved July29, 2019from:http://bme240.eng.uci.edu/students/06s/yuhsianh/Piezoelctric%20effect.htm

[14] Whatmore, R. W. (1986). Pyroelectric devices and materials. *Reports on progress in physics*, *49*(12), 1335.

[15] Leontsev, S. O., & Eitel, R. E. (2010). Progress in engineering high strain lead-free piezoelectric ceramics. *Science and Technology of Advanced Materials*, *11*(4), 044302.

[16] Zhang, Y., Sun, H., & Chen, W. (2018). A brief review of Ba (Ti0. 8Zr0. 2) O3-(Ba0. 7Ca0. 3) TiO3 based lead-free piezoelectric ceramics: past, present and future perspectives. *Journal of Physics and Chemistry of Solids*, *114*, 207-219.

[17] Ahn, C. W., Park, C. S., Dittmer, R., Hong, S. H., & Priya, S. (2010). Effect of elemental diffusion on temperature coefficient of piezoelectric properties in KNN-based lead-free composites. *Journal of materials science*, *45*(14), 3961-3965.

[18] Gao, D., Kwok, K. W., Lin, D., & Chan, H. L. W. (2008). Microstructure and electrical properties of La-modified K0. 5Na0. 5NbO3 lead-free piezoelectric ceramics. *Journal of Physics D: Applied Physics*, *42*(3), 035411.

[19] Xu, C., Lin, D., & Kwok, K. W. (2008). Structure, electrical properties and depolarization temperature of (Bi0. 5Na0. 5) TiO3–BaTiO3 lead-free piezoelectric ceramics. *Solid state sciences*, *10*(7), 934-940.

[20] Ge, W., Liu, H., Zhao, X., Li, X., Pan, X., Lin, D., ... & Luo, H. (2009). Orientation dependence of electrical properties of 0.96 Na 0.5 Bi 0.5 TiO 3-0.04 BaTiO 3 lead-free piezoelectric single crystal. *Applied Physics A*, *95*(3), 761-767.

[21] Guillemet-Fritsch, S., Valdez-Nava, Z., Tenailleau, C., Lebey, T., Durand, B., & Chane-Ching, J. Y. (2008). Colossal permittivity in ultrafine grain size BaTiO3–x and Ba0. 95La0. 05TiO3–x materials. *Advanced Materials*, *20*(3), 551-555.

[22] Lin, W., Fan, L., Lin, D., Zheng, Q., Fan, X., & Sun, H. (2013). Phase transition, ferroelectric and piezoelectric properties of Ba1− xCaxTi1− yZryO3 lead-free ceramics. *Current Applied Physics*, *13*(1), 159-164.

[23] López-Juárez, R., González, F., & Villafuerte-Castrejón, M. E. (2011). Lead-free ferroelectric ceramics with perovskite structure. *Ferroelectrics—Materials Aspects; Lallart, M., Ed.; In Tech: Rijeka, Croatia*, 305-330.

[24] Liu, W., & Ren, X. (2009). Large piezoelectric effect in Pb-free ceramics. *Physical review letters*, *103*(25), 257602.

[25] Shrout, T. R., & Zhang, S. J. (2007). Lead-free piezoelectric ceramics: Alternatives for PZT. *Journal of Electroceramics*, *19*(1), 113-126.

[26] Zhu, L. F., Zhang, B. P., Zhao, L., Li, S., Zhou, Y., Shi, X. C., & Wang, N. (2016). Large piezoelectric effect of (Ba, Ca) TiO3–xBa (Sn, Ti) O3 lead-free ceramics. *Journal of the European Ceramic Society*, *36*(4), 1017-1024.

[27] Lin, D., Kwok, K. W., & Chan, H. L. W. (2014). Structure, dielectric and piezoelectric properties of Ba0. 90Ca0. 10Ti1− xSnxO3 lead-free ceramics. *Ceramics International*, *40*(5), 6841-6846.

[28] Hersch, P., & Zweibel, K. (1982). *Basic photovoltaic principles and methods* (No. SERI/SP-290-1448). Solar Energy Research Inst., Golden, CO (USA).

[29] Chapin, D. M., Fuller, C. S., & Pearson, G. L. (1954). A new silicon p-n junction photocell for converting solar radiation into electrical power. *Journal of Applied Physics*, *25*(5), 676-677.

[30] Ginley, D., Green, M. A., & Collins, R. (2008). Solar energy conversion toward 1 terawatt. *Mrs Bulletin*, *33*(4), 355-364.

[31] Chynoweth, A. G. (1956). Surface space-charge layers in barium titanate. *Physical Review*, *102*(3), 705.

[32] Ng, K. K. (2002). *Complete guide to semiconductor devices* (pp. 431-437). IEEE Press.

[33] Sze, S. M., & Ng, K. K. (2006). *Physics of semiconductor devices*. John wiley & sons.

[34] Sproul, A. (2003). Understanding the pn Junction. *Solar Cells: Resource for the Secondary Science Teacher*.

[35] Penn State University, (2019). semiconductor p-n junctions, Retrieved July 22, 2019from:https://chem.libretexts.org/Bookshelves/Inorganic_Chemistry/Book%3A_Inorganic_Chemistry_(Wikibook)/Chapter_10%3A_Electronic_Properties_of_Materials%3A_Superconductors_and_Semiconductors/10.5_Semiconductor_p-n_junctions

[36] Yang, S. Y., Seidel, J., Byrnes, S. J., Shafer, P., Yang, C. H., Rossell, M. D., ... & Martin, L. W. (2010). Above- voltages from ferroelectric photovoltaic devices. *Nature nanotechnology*, *5*(2), 143.

[37] Lee, D., Baek, S. H., Kim, T. H., Yoon, J. G., Folkman, C. M., Eom, C. B., & Noh, T. W. (2011). Polarity control of carrier injection at ferroelectric/metal interfaces for electrically switchable diode and photovoltaic effects. *Physical Review B*, *84*(12), 125305.

[38] Mehta, R. R., Silverman, B. D., & Jacobs, J. T. (1973). Depolarization fields in thin ferroelectric films. *Journal of Applied Physics*, *44*(8), 3379-3385.

[39] Wurfel, P., & Batra, I. P. (1973). Depolarization-field-induced instability in thin ferroelectric films—experiment and theory. *Physical Review B*, *8*(11), 5126.

[40] Matsumura, A., Kamaike, Y., Horiuchi, T., Shimizu, M., Shiosaki, T., & Matsushige, K. (1995). Thermal effects in properties of photovoltaic currents of Pb (Zr, Ti) O3 thin films. *Japanese journal of applied physics*, *34*(9S), 5258.

[41] Brody, P. S., & Rod, B. J. (1993). Decay of remanent polarization in ferroelectric films using polarization-dependent photovoltages. *Integrated Ferroelectrics*, *3*(3), 245-257.

[42] Young, S. M., & Rappe, A. M. (2012). First principles calculation of the shift current photovoltaic effect in ferroelectrics. *Physical review letters*, *109*(11), 116601.

[43] Glass, A. M., Von der Linde, D., Auston, D. H., & Negran, T. J. (1975). Excited state polarization, bulk photovoltaic effect and the photorefractive effect in electrically polarized media. *Journal of Electronic Materials*, *4*(5), 915-943.

[44] Chanussot, G., & Glass, A. M. (1976). A bulk photovoltaic effect due to electron-phonon coupling in polar crystals. *Physics Letters A*, *59*(5), 405-407.

[45] Fradkin, V. M., & Magomadov, R. M. (1979). Anomalous photovoltaic effect in LiNbO 3: Fe in polarized light. *JETP Letters*, *30*, 686-688.

[46] Arizmendi, L. (2004). Photonic applications of lithium niobate crystals. *physica status solidi (a)*, *201*(2), 253-283.

[47] Fridkin, V. M., & Popov, B. (1978). Anomalous photovoltaic effect in ferroelectrics. *Soviet Physics Uspekhi*, *21*(12), 981.

[48] Carnicero, J., Caballero, O., Carrascosa, M., & Cabrera, J. M. (2004). Superlinear photovoltaic currents in LiNbO 3: analyses under the two-center model. *Applied Physics B*, *79*(3), 351-358.

[49] Gunter, P., & Micheron, F. (1978). Photorefractive effects and photocurrents in KNbO3: Fe. *Ferroelectrics*, *18*(1), 27-38.

[50] Brody, P. S., & Crowne, F. (1975). Mechanism for the high voltage photovoltaic effect in ceramic ferroelectrics. *Journal of Electronic Materials*, *4*(5), 955-971.

[51] Ichiki, M., Morikawa, Y., Nonaka, K., Nakada, T., Endo, C., & Maeda, R. (2003, October). Photovoltaic effect of PLZT in a layered film structure and its application to ultraviolet sensing. In *Digest of Papers Microprocesses and Nanotechnology 2003. 2003 International Microprocesses and Nanotechnology Conference* (pp. 184-185). IEEE.

[52] Ichiki, M., Morikawa, Y., & Nakada, T. (2002). Electrical properties of ferroelectric lead lanthanum zirconate titanate as an energy transducer for application to electrostatic-optical motor. *Japanese journal of applied physics*, *41*(11S), 6993.

[53] Chen, F.S. (1969) Optically induced change of refractive indices in LiNbO3 and LiTaO3. *Journal of Applied Physics*, **40** (8), 3389–3396.

[54] Paillard, C., Bai, X., Infante, I. C., Guennou, M., Geneste, G., Alexe, M., ... & Dkhil, B. (2016). Photovoltaics with ferroelectrics: Current status and beyond. *Advanced Materials*, *28*(26), 5153-5168.

[55] Liu, H., Chen, J., Ren, Y., Zhang, L., Pan, Z., Fan, L., & Xing, X. (2015). Large Photovoltage and Controllable Photovoltaic Effect in PbTiO3-Bi (Ni2/3+ xNb1/3–x) O3–δ Ferroelectrics. *Advanced Electronic Materials*, *1*(4), 1400051.

[56] Nechache, R., Harnagea, C., Li, S., Cardenas, L., Huang, W., Chakrabartty, J., & Rosei, F. (2015). Bandgap tuning of multiferroic oxide solar cells. *Nature photonics*, *9*(1), 61.

[57] Yuan, Y., Xiao, Z., Yang, B., & Huang, J. (2014). Arising applications of ferroelectric materials in photovoltaic devices. *Journal of Materials chemistry A*, *2*(17), 6027-6041.

[58] Bhatnagar, A. (2018). Ferroelectric Photovoltaics. *Ferroelectric Materials for Energy Applications*, 61-94.

[59] Cao, D., Wang, C., Zheng, F., Dong, W., Fang, L., & Shen, M. (2012). High-efficiency ferroelectric-film solar cells with an n-type Cu2O cathode buffer layer. *Nano letters*, *12*(6), 2803-2809.

[60] Zhang, J., Su, X., Shen, M., Dai, Z., Zhang, L., He, X., ... & Zou, G. (2013). Enlarging photovoltaic effect: combination of classic photoelectric and ferroelectric photovoltaic effects. *Scientific reports*, *3*, 2109.

[61] Tan, L. Z., Zheng, F., Young, S. M., Wang, F., Liu, S., & Rappe, A. M. (2016). Shift current bulk photovoltaic effect in polar materials—hybrid and oxide perovskites and beyond. *Npj Computational Materials*, *2*, 16026.

[62] You, L., Zheng, F., Fang, L., Zhou, Y., Tan, L. Z., Zhang, Z., ... & Chang, L. (2018). Enhancing ferroelectric photovoltaic effect by polar order engineering. *Science advances*, *4*(7), eaat3438.

[63] Lopez-Varo, P., Bertoluzzi, L., Bisquert, J., Alexe, M., Coll, M., Huang, J., ... & Yuan, Y. (2016). Physical aspects of ferroelectric semiconductors for photovoltaic solar energy conversion. *Physics Reports*, *653*, 1-40.

[64] Wemple, S. H. (1970). Polarization Fluctuations and the Optical-Absorption Edge in BaTi O 3. *Physical Review B*, *2*(7), 2679.

[65] Koch, W. T. H., Munser, R., Ruppel, W., & Würfel, P. (1975). Bulk photovoltaic effect in BaTiO3. *Solid State Communications*, *17*(7), 847-850.

[66] Qin, M., Yao, K., & Liang, Y. C. (2008). High efficient photovoltaics in nanoscaled ferroelectric thin films. *Applied Physics Letters*, *93*(12), 122904.

[67] Alexe, M., & Hesse, D. (2011). Tip-enhanced photovoltaic effects in bismuth ferrite. *Nature communications*, *2*, 256.

[68] Ji, W., Yao, K., & Liang, Y. C. (2010). Bulk photovoltaic effect at visible wavelength in epitaxial ferroelectric BiFeO3 thin films. *Advanced Materials*, *22*(15), 1763-1766.

[69] Dhar, A., & Mansingh, A. (1990). Optical properties of reduced lithium niobate single crystals. *Journal of applied physics*, *68*(11), 5804-5809.

[70] Grinberg, I., West, D. V., Torres, M., Gou, G., Stein, D. M., Wu, L., ... & Spanier, J. E. (2013). Perovskite oxides for visible-light-absorbing ferroelectric and photovoltaic materials. *Nature*, *503*(7477), 509.

[71] Wiesendanger, E. (1973). Dielectric, mechanical and optical properties of orthorhombic KNbO3. *Ferroelectrics*, *6*(1), 263-281.

[72] An, H., Han, J. Y., Kim, B., Song, J., Jeong, S. Y., Franchini, C., ... & Lee, S. (2016). Large enhancement of the photovoltaic effect in ferroelectric complex oxides through bandgap reduction. *Scientific reports*, *6*, 28313.

[73] Das, S., Ghara, S., Mahadevan, P., Sundaresan, A., Gopalakrishnan, J., & Sarma, D. D. (2018). Designing a Lower Band Gap Bulk Ferroelectric Material with a Sizable Polarization at Room Temperature. *ACS Energy Letters*, *3*(5), 1176-1182.

[74] Wu, L., Podpirka, A., Spanier, J. E., & Davies, P. K. (2019). Ferroelectric, Optical and Photovoltaic Properties of Morphotropic Phase Boundary Compositions in the PbTiO3-BiFeO3-Bi (Ni1/2Ti1/2) O3 System. *Chemistry of Materials*.

[75] Bretos, I., Jiménez, R., Ricote, J., & Calzada, M. L. (2018). Synthesis by low temperature solution processing of ferroelectric perovskite oxide thin films as candidate materials for photovoltaic applications. In *The Future of Semiconductor Oxides in Next-Generation Solar Cells* (pp. 45-81). Elsevier.

[76] Wu, L., Akbashev, A. R., Podpirka, A. A., Spanier, J. E., & Davies, P. K. (2019). Infrared-to-ultraviolet light-absorbing BaTiO3-based ferroelectric photovoltaic materials. *Journal of the American Ceramic Society*, *102*(7), 4188-4199.

[77] Di Quarto, F., Sunseri, C., Piazza, S., & Romano, M. C. (1997). Semiempirical correlation between optical band gap values of oxides and the difference of electronegativity of the elements. Its importance for a quantitative use of photocurrent spectroscopy in corrosion studies. *The Journal of Physical Chemistry B*, *101*(14), 2519-2525.

[78] Shannon, R. D. (1976). Revised effective ionic radii and systematic studies of interatomic distances in halides and chalcogenides. *Acta crystallographica section A: crystal physics, diffraction, theoretical and general crystallography*, *32*(5), 751-767.

[79] Goudochnikov, P., & Bell, A. J. (2007). Correlations between transition temperature, tolerance factor and cohesive energy in 2+: 4+ perovskites. *Journal of Physics: Condensed Matter*, *19*(17), 176201.

[80] Moulson, A. J., & Herbert, J. M. (2003). *Electroceramics: materials, properties, applications*. John Wiley & Sons.

[81] Gao, R. L., Yang, H. W., Chen, Y. S., Sun, J. R., Zhao, Y. G., & Shen, B. G. (2014). Oxygen vacancies induced switchable and nonswitchable photovoltaic effects in Ag/Bi0. 9La0. 1FeO3/La0. 7Sr0. 3MnO3 sandwiched capacitors. *Applied Physics Letters*, *104*(3), 031906.

[82] Ge, C., Jin, K. J., Zhang, Q. H., Du, J. Y., Gu, L., Guo, H. Z., ... & Wang, C. (2016). Toward switchable photovoltaic effect via tailoring mobile oxygen vacancies in perovskite oxide films. *ACS applied materials & interfaces*, *8*(50), 34590-34597.

[83] Gao, R. L., Yang, H. W., Fu, C. L., Cai, W., Chen, G., Deng, X. L., ... & Shen, B. G. (2015). Tunable photovoltaic effects induced by different cooling oxygen pressure in Bi0. 9La0. 1FeO3 thin films. *Journal of Alloys and Compounds*, *624*, 1-8.

[84] Moubah, R., Rousseau, O., Colson, D., Artemenko, A., Maglione, M., & Viret, M. (2012). Photoelectric effects in single domain BiFeO3 crystals. *Advanced Functional Materials*, *22*(22), 4814-4818.

[85] López, R., & Gómez, R. (2012). Band-gap energy estimation from diffuse reflectance measurements on sol–gel and commercial TiO2: a comparative study. *Journal of sol-gel science and technology*, *61*(1), 1-7.

[86] Torrent, J. O. S. É., & Barron, V. (2008). Diffuse reflectance spectroscopy. *Methods of soil analysis. Part*, *5*, 367-387.

[87] Xiao, H., Dong, W., Guo, Y., Wang, Y., Zhong, H., Li, Q., & Yang, M. M. (2019). Design for Highly Piezoelectric and Visible/Near-Infrared Photoresponsive Perovskite Oxides. *Advanced Materials*, *31*(4), 1805802.

[88] Rani, A., Kolte, J., Vadla, S. S., & Gopalan, P. (2016). Structural, electrical, magnetic and magnetoelectric properties of Fe doped BaTiO3 ceramics. *Ceramics International*, *42*(7), 8010-8016.

[89] Guo, Z., Pan, L., Bi, C., Qiu, H., Zhao, X., Yang, L., & Rafique, M. Y. (2013). Structural and multiferroic properties of Fe-doped Ba0. 5Sr0. 5TiO3 solids. *Journal of Magnetism and Magnetic Materials*, *325*, 24-28.

[90] Keswani, B. C., Devan, R. S., Kambale, R. C., James, A. R., Manandhar, S., Kolekar, Y. D., & Ramana, C. V. (2017). Correlation between structural, magnetic and ferroelectric properties of Fe-doped (Ba-Ca) TiO3 lead-free piezoelectric. Journal of Alloys and Compounds, 712, 320-333.

[91] Sharma, P., Kumar, P., Kundu, R. S., Juneja, J. K., Ahlawat, N., & Punia, R. (2015). Structural and dielectric properties of substituted barium titanate ceramics for capacitor applications. *Ceramics International*, *41*(10), 13425-13432.

[92] Ray, J., & Hing, P. (2000). Sol-gel derived Ba (Fe, Ti) O 3 ferroelectric materials for infrared sensors. *Journal of Applied Physics*, *88*(2), 1008-1014.

[93] Merz, W. J. (1949). The Electric and Optical Behavior of BaTi O 3 Single-Domain Crystals. *Physical Review*, *76*(8), 1221.

[94] Kola, L., Murali, D., Pal, S., Nanda, B. R. K., & Murugavel, P. (2019). Enhanced bulk photovoltaic response in Sn doped BaTiO3 through composition dependent structural transformation. *Applied Physics Letters*, *114*(18), 183901.

[95] Zhao, X., Fang, B., Cao, H., Guo, Y., & Luo, H. (2002). Dielectric and piezoelectric performance of PMN–PT single crystals with compositions around the MPB: influence of composition, poling field and crystal orientation. *Materials Science and Engineering: B*, *96*(3), 254-262.

[96] Xue, D., Zhou, Y., Bao, H., Gao, J., Zhou, C., & Ren, X. (2011). Large piezoelectric effect in Pb-free Ba (Ti, Sn) O3-x (Ba, Ca) TiO3 ceramics. *Applied Physics Letters*, *99*(12), 122901.

[97] Chen, X., Liu, L., Peter, Y. Y., & Mao, S. S. (2011). Increasing solar absorption for photocatalysis with black hydrogenated titanium dioxide nanocrystals. *Science*, *331*(6018), 746-750.

[98] Naldoni, A., Allieta, M., Santangelo, S., Marelli, M., Fabbri, F., Cappelli, S., ... & Dal Santo, V. (2012). Effect of nature and location of defects on bandgap narrowing in black TiO2 nanoparticles. *Journal of the American Chemical Society*, *134*(18), 7600-7603.

[99] Srikanth, K. S., Hooda, M. K., Singh, H., Singh, V. P., & Vaish, R. (2018). Structural and photocatalytic performance of (Ba, Ca) TiO3–Ba (Sn, Ti) O3 ferroelectric ceramics. *Materials Science in Semiconductor Processing*, *79*, 153-160.

[100] Upadhyay, S., Shrivastava, J., Solanki, A., Choudhary, S., Sharma, V., Kumar, P., ... & Dass, S. (2011). Enhanced photoelectrochemical response of BaTiO3 with Fe doping: experiments and first-principles analysis. *The Journal of Physical Chemistry C*, *115*(49), 24373-24380.

[101] Yang, F., Lin, S., Yang, L., Liao, J., Chen, Y., & Wang, C. Z. (2017). First-principles investigation of metal-doped cubic BaTiO3. *Materials Research Bulletin*, *96*, 372-378.

[102] Maldonado, F., Jácome, S., & Stashans, A. (2017). Codoping of Ni and Fe in tetragonal BaTiO3. *Computational Condensed Matter*, *13*, 49-54.

[103] Scafetta, M. D., Cordi, A. M., Rondinelli, J. M., & May, S. J. (2014). Band structure and optical transitions in LaFeO3: theory and experiment. *Journal of Physics: Condensed Matter*, *26*(50), 505502.

[104] Swain, A. B., Rath, M., Biswas, P. P., Rao, M. R., & Murugavel, P. (2019). Polarization controlled photovoltaic and self-powered photodetector characteristics in Pb-free ferroelectric thin film. *APL Materials*, *7*(1), 011106.

[105] Ma, N., Zhang, K., & Yang, Y. (2017). Photovoltaic–pyroelectric coupled effect induced electricity for self-powered photodetector system. *Advanced Materials*, *29*(46), 1703694.

[106] Spanier, J. E., Fridkin, V. M., Rappe, A. M., Akbashev, A. R., Polemi, A., Qi, Y., ... & Xiao, G. (2016). Power conversion efficiency exceeding the Shockley–Queisser limit in a ferroelectric insulator. *Nature Photonics*, *10*(9), 611.

[107] Ma, N., & Yang, Y. (2018). Boosted photocurrent in ferroelectric BaTiO3 materials via two dimensional planar-structured contact configurations. *Nano energy*, *50*, 417-424.

[108] Yang, M., Bhatnagar, A., & Alexe, M. (2015). Electronic origin and tailoring of photovoltaic effect in BiFeO3 single crystals. *Advanced Electronic Materials*, *1*(11), 1500139.

[109] Ma, N., & Yang, Y. (2019). Boosted photocurrent via cooling ferroelectric BaTiO3 materials for self-powered 405 nm light detection. *Nano Energy*, *60*, 95-102.

[110] Hamza, A., Benabdallah, F., Kallel, I., Seveyrat, L., Lebrun, L., & Khemakhem, H. (2018). Effect of rare-earth substitution on the electrical properties and Raman spectroscopy of BCTZ ceramics. *Journal of Alloys and Compounds*, *735*, 2523-2531.

[111] Anton, E. M., Jo, W., Damjanovic, D., & Rödel, J. (2011). Determination of depolarization temperature of (Bi1/2Na1/2) TiO3-based lead-free piezoceramics. *Journal of Applied Physics*, *110*(9), 094108.

[112] Akbashev, A. R., Fridkin, V. M., & Spanier, J. E. (2016). Semiconducting and Photovoltaic Ferroelectrics. *Nanoscale Ferroelectrics and Multiferroics: Key Processing and Characterization Issues, and Nanoscale Effects*, 830-850.

[113] Hu, Y., Dong, W., Zheng, F., Fang, L., & Shen, M. (2014). Fe (III) doped and grafted PbTiO3 film photocathode with enhanced photoactivity for hydrogen production. *Applied Physics Letters*, *105*(8), 082903.

[114] Yi, H. T., Choi, T., Choi, S. G., Oh, Y. S., & Cheong, S. W. (2011). Mechanism of the switchable photovoltaic effect in ferroelectric BiFeO3. *Advanced Materials*, *23*(30), 3403-3407.

[115] Xing, J., Guo, E. J., Dong, J., Hao, H., Zheng, Z., & Zhao, C. (2015). High-sensitive switchable photodetector based on BiFeO3 film with in-plane polarization. *Applied Physics Letters*, *106*(3), 033504.

[116] Park, J., Won, S. S., Ahn, C. W., & Kim, I. W. (2013). Ferroelectric Photocurrent Effect in Polycrystalline Lead-Free (K 0.5 Na 0.5)(Mn 0.005 Nb 0.995) O 3 Thin Film. *Journal of the American Ceramic Society*, *96*(1), 146-150.

[117] Wang, C., Cao, D., Zheng, F., Dong, W., Fang, L., Su, X., & Shen, M. (2013). Photocathodic behavior of ferroelectric Pb (Zr, Ti) O 3 films decorated with silver nanoparticles. *Chemical Communications*, *49*(36), 3769-3771.

[118] Alexe, M. (2012). Local mapping of generation and recombination lifetime in BiFeO3 single crystals by scanning probe photoinduced transient spectroscopy. *Nano letters*, *12*(5), 2193-2198.

[119] Patel, S., Srikanth, K. S., Steiner, S., Vaish, R., & Frömling, T. (2018). Pyroelectric and impedance studies of the 0.5 Ba (Zr0. 2Ti0. 8) O3-0.5 (Ba0. 7Sr0. 3) TiO3 ceramics. *Ceramics International*, *44*(17), 21976-21981.

[120] Srikanth, K. S., Patel, S., Steiner, S., & Vaish, R. (2018). Pyroelectric signals in (Ba, Ca) TiO3-xBa (Sn, Ti) O3 ceramics: a viable alternative for lead-based ceramics. *Scripta Materialia*, *146*, 146-149.

[121] Qiao, P., Zhang, Y., Chen, X., Zhou, M., Wang, G., & Dong, X. (2019). Enhancing pyroelectric properties in (Pb1−1.5 xLax)(Zr0. 86Ti0. 14) O3 ceramics through composition modulated phase transition. *Ceramics International*, *45*(6), 7114-7119.

[122] Peter, L. M. (2013). Energetics and kinetics of light-driven oxygen evolution at semiconductor electrodes: the example of hematite. *Journal of Solid State Electrochemistry*, *17*(2), 315-326.

[123] Zhang, P., Cao, D., Wang, C., Shen, M., Su, X., Fang, L., ... & Zheng, F. (2012). Enhanced photocurrent in Pb (Zr0. 2Ti0. 8) O3 ferroelectric film by artificially introducing asymmetrical interface Schottky barriers. *Materials Chemistry and Physics*, *135*(2-3), 304-308.

[124] Thomas, R. E., & Haas, G. A. (1972). Diffusion measurements in thin films utilizing work function changes: Cr into Au. *Journal of Applied Physics*, *43*(12), 4900-4907.

[125] Guo, Y., Guo, B., Dong, W., Li, H., & Liu, H. (2013). Evidence for oxygen vacancy or ferroelectric polarization induced switchable diode and photovoltaic effects in BiFeO3 based thin films. *Nanotechnology*, *24*(27), 275201.

[126] Hu, L., Sheng, Z. G., Huang, Y. N., Song, W. H., & Sun, Y. P. (2012). Remarkable current-enhanced photoconductivity in oxygen-deficient La7/8Sr1/8MnO3− δ thin film. *Applied Physics Letters*, *101*(4), 042413.

[127] Yao, K., Gan, B. K., Chen, M., & Shannigrahi, S. (2005). Large photo-induced voltage in a ferroelectric thin film with in-plane polarization. *Applied Physics Letters*, *87*(21), 212906.

[128] Yang, C. H., Seidel, J., Kim, S. Y., Rossen, P. B., Yu, P., Gajek, M., ... & Maksymovych, P. (2009). Electric modulation of conduction in multiferroic Ca-doped BiFeO 3 films. *Nature materials*, *8*(6), 485-493.

[129] Zhao, Y., Liang, C., Zhang, H., Li, D., Tian, D., Li, G., ... & Zhang, F. (2015). Anomalously large interface charge in polarity-switchable photovoltaic devices: an indication of mobile ions in organic–inorganic halide perovskites. *Energy & Environmental Science*, *8*(4), 1256-1260.